DETERMINATION OF ATMOSPHERIC WATER VAPOUR ISOTOPIC COMPOSITION USING MULTI-PLATFORM INSTRUMENTS AND MODELS OVER ETHIOPIA: IMPLICATIONS FOR WATER CYCLE.

A thesis submitted to the School of Graduate Studies

Addis Ababa University

In partial fulfilment of the requirements for the degree of

Doctor of Philosophy in Atmospheric Physics

By

Samuel Takele Kenea

Addis Ababa, Ethiopia

November, 2014

The undersigned hereby certify that they have read and recommended to the Faculty of Science School of Graduate Studies acceptance of a thesis entitled "**Determination of atmospheric water vapour isotopic composition using multi-platform instruments and models over Ethiopia: Implications for water cycle.**" by **Samuel Takele Kenea** in partial fulfillment of the requirements for the degree of **Doctor of Philosophy**.

Dated: November 2014

Dr. Gizaw Mengistu, Research Supervisor _____

Associate Professor, Department of Physics

Addis Ababa University, Ethiopia

Prof. Ding Yi Wang, External Examiner _____

Professor, School of Sciences

Xian Jiao Tong University, China

Prof. Ashok V. Gholap, Internal Examiner _____

Professor, Department of Physics

Addis Ababa University, Ethiopia

Dr. Teshome Senbeta, Examining Chair _____

Assistant Professor, Department of Physics

Addis Ababa University, Ethiopia

Dedicated to my family.

Table of Contents

List of Figures

Abstract

Coupled stable isotopes of hydrogen and oxygen (δD and δ^{18}O) in water vapour, as well as in precipitation, represent valuable tools for quantifying the atmospheric processes in water cycle. Various physical processes associated with the state of phase changes of water potentially impart unique signal on the integrated isotopic fractionation of water vapour in the atmosphere. For instance, atmospheric processes such as condensation, evapo-transpiration and transport can be characterized quantitatively and qualitatively using Rayleigh distillation curves of δD versus humidity. In this study, abundances of H_2O and δD determined from various satellites, models, and Fourier transform infrared spectrometer (FTIR) at Addis Ababa, Ethiopia are used to evaluate isotopic fractionation over Ethiopia and assess water vapour budget and cycle in the region. Volume mixing ratio (VMR) profiles of H_2O and δD are simultaneously retrieved from FTIR solar absorption spectra during June, 2009 to March, 2013. Fifteen spectral microwindows in the region between 2600 to 3200 cm^{-1} are used to determine their profiles. For the peculiar features of the remote sensing product of water vapour isotopologues, it is essential applying aposteriori corrections to ensure that both H_2O and δD products are representative of the same air mass and also minimize the cross-dependence between them. Detailed error analysis of the retrieved species are also performed.

H_2O VMR profiles and integrated column amounts from FTIR are compared with the coincident satellite observations of Tropospheric Emission Spectrometer (TES),

Atmospheric Infrared Sounding (AIRS) instruments, and Modular Earth Submodel System (MESSy) model. The mean relative differences in H_2O profiles of FTIR with TES and MESSy are generally lower than 27% within the altitude range of 3.6 and 8.9 km, whereas difference from AIRS is lower than 45%. The mean relative differences of integrated column amounts are within +3.5 to +15.4% for FTIR versus TES, whereas -9.4 to -28.6% for FTIR versus MESSy and AIRS. The corresponding standard deviations are within 21.7 to 33.6% among them. Thus, the retrieved H_2O VMR and column amounts from a tropical site, Addis Ababa, is found to exhibit a general agreement with these instruments and model.

Spatio-temporal variability of isotopic composition of water vapour using TES observations are examined over Ethiopia. The seasonal variation of δD in vapour composition of the region is mainly controlled by differences in sources of moisture owing to the seasonal movement of the ITCZ and local factors such as amount and temperature effects. The role of atmospheric processes that contribute to the seasonal variability of isotope composition of water vapour at 682 and 510 hPa pressure levels over our site are characterized by fitting the Rayleigh distillation curves of δD versus H_2O. Enrichment characteristics are identified at 682 hPa level in all seasons, which is likely caused by surface influence. In addition, δD vapour that falls below the Rayleigh curve is generally associated with moisture recycling in convective clouds, and this could partly describe some observations in summer season. On the other hand, δD vapour that falls above the Rayleigh curve is typically associated with advective mixing which explains a large number of observations during Spring and Autumn seasons. However, winter observations are strongly influenced by moisture mixing process. Further analysis of isotopic composition of water vapour from IsoGSM model follows the known seasonal cycles observed in precipitation from earlier studies suggesting that the dominant mode of water vapour variability is governed mainly by large scale climate system.

Acknowledgements

First of all, I would like to express my deep gratitude to my research supervisor Dr. Gizaw Mengistu for his strong encouragement and consistent support, and numerous helpful discussions during the development of this thesis work. I would also like to greatly acknowledge Samara university for the sponsorship during my stay at Addis Ababa University. I am also thankful to Dr. Thomas Blumenstock and Dr. Frank Hase, from institute of Karlshruh, Germany, for their fruitful suggestion and comments during the manuscript preparation as well as making support in operating the ground-based FTIR instrument established at Addis Ababa site. Many thanks goes to Dr. Kei Yoshimura from Atmosphere and Ocean Research Institute, University of Tokyo, Japan, who provided me the IsoGSM model data which are helpful for enhancing the scientific aspect of the result presented in the thesis. Great thanks to Dr. Lemi Demeyu (former chairman of physics Department) and Dr. Belayneh Mesfin, current chairman of physics Department, who have supported me to access the necessary research facilities. Special thanks to W/r Tsilat Adnew the secretary of physics department for kind cooperation. I also acknowledge to all IGSSA staff for kind response and support for the research facility.

I am grateful to my best friends Dr. Alemnew Geto and Derbe Teshome, with whom I have shared a great experience in all aspects that significantly helped me for the achievement. Many thanks extends to Gemechu Fanta, Titike Kassa, and others, from atmospheric science group, and all my friends who inspired me to be successful. Also thanks to Gezahegn Sufa and Milkessa Gebeyehu, who were the former FTIR group, for having fruitful discussions during the measurement period. Finally, I would like to thank my family for their continuous support to accomplish my work successfully.

Addis Ababa, Ethiopia Samuel Takele

October, 2014

Chapter 1

Introduction

Water is the principal molecule that governs the climate on Earth. This is because, through the hydrological cycle, it is involved in all phenomena from energy transport to radiative effects governing the climate system [1]. Atmospheric water, in the form of both vapour and clouds, is the most prominent greenhouse component that traps the outgoing longwave radiation (OLR) [2]. Understanding the atmospheric water vapour sources (evaporation from ocean or land), sinks (precipitation), and transport (advection, turbulence, diffusion, inner-cloud processes, etc.) is indispensable for gaining better insight on the weather and climate change. However, its concentration, evolution, and transport processes are still acquired further attention [3, and references therein]. The water cycle strongly controls various feedback mechanisms of the Earth system in response to perturbations of the energy balance of the troposphere such as cloud and ice/snow-albedo feedbacks. The water cycle is also coupled to the surface energy budget by latent heat fluxes associated with evaporation and condensation. Large fluxes of moisture into and out of the atmosphere by evapotranspiration and precipitation replace atmospheric water vapour, on average, every ten days according to global model estimates [4]. As global temperatures increase, it is

expected that evapotranspiration will also increase, leading to more water vapour in the atmosphere and a positive feedback on climate forcing. Indeed, there is some evidence that the specific humidity of the atmosphere is already increasing due to anthropogenic influences [5]. However, many aspects of the water cycle are still uncertain such as rainfall evaporation [6] or radiative impacts depending on the present water phase [7].

In the upper troposphere and lower stratosphere ($\geq$ 56 hPa pressure $\leq$ 146 hPa) the radiative and chemical effects of water vapour are large and the concentration of H_2O varies considerably with the temperature and relative humidity. From the perspective of global climate models, almost half of the projected increase in temperature due to a doubling of carbon dioxide in the atmosphere results from the effects of increased water vapour. Tropical Tropopause Layer (TTL) (121 to 68 hPa) is a transition layer sharing Upper Tropospheric (UT) and Lower Stratospheric (LS) characteristics, is an important gateway for Troposphere to Stratosphere Transport (TST), and plays a pivotal role in the global composition and circulation of the stratosphere [8, 9]. Troposphere to Stratosphere Transport (TST) processes responsible for the upward motion of air masses are: (i) the slow ascent (300 m month^{-1}) due to radiative heating associated with horizontal advection and known as 'Cold Trap' [8, 10, 11], (ii) fast overshooting updrafts followed by detrainment referred as 'Freeze and Dry' process [12-15], and (iii) the fast and direct injection by 'geyser-like' overshoots [16-18] that can penetrate into the LS. However, the detailed physical mechanisms of TST processes that are responsible for the water vapour budget in the TTL and LS layers are not still fully addressed at global scale [19]. As a matter of fact, several research activities in this regard have been intensively conducted and still continued

rigorously. Water vapour in the TTL primarily comes from convective processes. The interplay between transport and freeze-drying controls the amount of H_2O lifted into the stratosphere [20]. The role of overshooting deep convection is quite significant on the water content of the TTL and lower stratosphere [21]. H_2O from overshooting convection can be radiatively lifted up to the stratosphere [22]. Thus stratospheric H_2O is closely linked to convection and vertical ascent in the TTL [23].

Therefore, additional knowledge about the water cycle would allow improved weather forecasts as well as more precise climate predictions. Improving the climate models treatment of the complex water cycle is one of the key goals set by the Intergovernmental Panel on Climate Change (IPCC). In this context atmospheric water isotopologues ratios are of great interest. Water vapour isotopologues ratios are the powerful tools for investigating different atmospheric processes since the partitioning of the different isotopologues depends on the underlying process (equilibrium condensation or Rayleigh process, ice lofting, mixing of dry and humid air masses, rain evaporation, plant transpiration, etc.). In the fact that, measurements of stable isotopologues of water can provide key constraints on the processes controlling clouds and humidity, because of the following reasons: the isotopic composition of water will change as the water changes its state of phase; water sources such as the ocean and plants have different isotopic signatures (or compositions); and mixing processes will affect the isotopic composition of water differently than phase changes. In the lower troposphere, the water vapour isotopic composition is sensitive to the origin of water vapour and precipitation, such as continental recycling or convection in the budget [24, 25, 26] or air mass origin [27]. In the mid-troposphere, the water vapour isotopic composition provides information about water cycle processes such as mixing

of air masses [28] and rain re-evaporation, on average, about 20% to 50% of tropical precipitation over the ocean re-evaporated before reaching the surface [6]. In the upper troposphere, this isotope signal can reflect the role of convection in the transport of water in the upper troposphere and through the tropopause [29] and the processes that control upper tropospheric humidity [26].

For large potential applications of the isotope signals, there are a number of measurement techniques have been developed considerably. As reported in [6], the isotopic composition of tropospheric water vapour may differ significantly from that of precipitation due to separate sources. Therefore, remote sensing provides new information about the hydrologic cycle unattainable from water measurements at the surface. The remote sensing of ground-based high resolution Fourier Transform Infrared (FTIR) instrument and space based sensors such as, Tropospheric Emission Spectrometer (TES), Scanning Imaging Absorption Spectrometer for Atmospheric Chartography (SCIAMACHY), Michelson Interferometer for Passive Atmospheric Sounding (MIPAS), Sub-Millimeter Radiometer (SMR), and Atmospheric Chemistry Experiment (ACE), Infrared Atmospheric Sounding Interferometer (IASI), and Japanese Greenhouse Gases Observing SATellite (GOSAT) have been engaged in providing water vapour isotope compositions data depending on different temporal and spatial resolutions, for detailed description about these different sensors can be obtained in [30-38]. In particular, the FTIR spectrometer has a great potential for making continuous observations with high temporal resolution (in the order of minutes), which offers a good opportunity for investigation of the variability of the species with different temporal scales in connection with physical phenomena, although it is limited to small area. The extensive analysis of the FTIR measurements of δD profiles between

the surface and the middle/upper troposphere have been reported at the region of subtropical and midlatitudes (e.g. [3, 35, 39]). However, this is the first ground-based FTIR observation of tropospheric stable water vapour isotopologues at equatorial station. Therefore, the main objective of this research is focused on quantifying the abundance of atmospheric water vapour distribution and its isotope composition at tropical sites to investigate the role of tropospheric processes that are responsible for the movement of water cycle. The specific objectives are stated as follows.

1. Intercomparison of water vapour isotopologues measurements from ground-based FTIR Spectrometer at Equatorial Station: Addis Ababa, Ethiopia with those of satellite observations and model simulations

2. Application of FTIR, TES, and IsoGSM results of water vapour isotopologues ratio to estimate the role of tropospheric processes on water vapour budget.

3. Assessment of spatial and temporal variability of δD and H_2O amounts over Ethiopia.

4. Quantification of the role of local convection and temperature on the vertical distribution of water vapour in the layer between upper troposphere and lower stratosphere over Addis Ababa.

The structure of the thesis is organized as follows. Chapter 2 gives a description about the isotopic composition of atmospheric water. Chapter 3 presents an overview of the instrumentations, models and measurement site, Chapter 4 deals with retrieval procedure for water vapour isotopologues from the FTIR spectra, Chapter 5 is focused on the intercomparison of δD and H_2O amounts from various instruments, Chapter 6 provides discussion on the results for tropospheric H_2O, δD, and $\delta^{18}O$ budget in cycle, and followed by upper troposphere and lower stratosphere water vapour budget

in Chapter 7. Finally, conclusions are given in Chapter 8.

Chapter 2

Isotopic composition of water in the atmosphere

A wide spectrum of empirical and theoretical studies has laid the foundations for the application of stable water isotope ratios in investigating the hydrologic cycle. Early empirical studies investigated the main physical processes governing isotopic fractionation of water molecules under laboratory conditions. Simple models based on these empirical studies are applied to the interpretation of observational records ranging from local to regional scales. Recently, the development of numerical models incorporating water isotope tracers has played an important role for understanding of the isotopic response with respect to various atmospheric processes over a wide range of temporal and spatial scales.

2.1 Equilibrium fractionation

Hydrogen exists naturally in two stable isotopic forms (^{1}H, protium and ^{2}H or D, deuterium) while oxygen has three stable isotopic forms (^{16}O, ^{17}O, and ^{18}O). Water molecules can therefore occur with any combination of these isotopes, although the only three forms existing in readily measurable quantities are $H_2^{18}O$, HDO, and the

Table 2.1. Typical natural isotopic ratios of water in the hydrological cycle taken from [42].

Natural reservoir	δ^{18}O	δD
Ocean water	-6 ... +3	-28 ... +10
Arctic sea ice	-3 ... +3	0 ... +25
Marine moisture	-15 ... -11	-100 ... -75
Lake Chad	+8 ... +16	+15 ... +50
Alpine glaciers	-19 ... -3	-130 ... -90
Greenland	-39 ... -25	<-150 ... -100
Antarctica	-39 ... -25	<-150 ... -100
(Sub)Tropical precipitation	-8 ... -2	-50 ... -20
Mid-latitude rain	-10 ... -3	-80 ... -20
Mid-latitude snow	-20 ... -10	-160 ... -80

normal water molecule $H_2^{16}O$. The ratio of isotopically heavy to normal water is commonly expressed in parts per thousand (‰) relative to the ratio in Standard Mean Ocean Water (SMOW):

$$\delta = (\frac{R_{sample}}{R_{SMOW}} - 1) \times 1000 \tag{2.1.1}$$

where the standard ratios are given by R = 0.15595 x 10^{-3} for HDO [40] and R = 2.00520 x 10^{-3} for $H_2^{18}O$ [41]. For instance, δD represents the abundance of HDO relative to that of H_2O. A δD of 0‰ indicates that the ratio is equal to that of sea water. A value of -500‰ means that the ratio in the sample is only half that of the ratio in sea water, and a value of -1000‰ means that the sample contains no HDO.

The ratio of isotopically heavy water to normal water is altered at phase transitions due to the different saturation vapour pressures of the isotopic species. Thus the ratio of the saturation vapour pressures of the normal and isotopically heavy water (e and e_i respectively) gives the (equilibrium) fractionation factor $\alpha = e/e_i$ [43, 44]. The fractionation factor is greater than unity as the condensate is isotopically enriched

relative to the vapour. The reverse relationship holds for evaporation, with the fractionation factor inverted. The temperature dependence of vapour pressure implies that the fractionation factor is also dependent on temperature:

$$\alpha \propto exp(\frac{L_i m_i - Lm}{RT}) \tag{2.1.2}$$

where L and L_i are the latent heats of fusion, m and m_i are the molecular weights for normal and isotopically heavy water respectively, R is the ideal gas constant and T is the temperature. The fractionation factors are found empirically as a function of temperature, $T(K)$, expressed as series expansions, for the liquid to vapour change [45]:

$$\alpha_{HDO} = exp[\frac{24.844}{T^2} \times 10^3 - \frac{76.248}{T} + 52.612 \times 10^{-3}] \tag{2.1.3}$$

$$\alpha_{H_2^{18}O} = exp[\frac{1.137}{T^2} \times 10^3 - \frac{0.4156}{T} - 2.0667 \times 10^{-3}] \tag{2.1.4}$$

In the case of solid to vapour fractionation, the formulations for HDO [46] and for $H_2^{18}O$ [47] are expressed:

$$\alpha_{HDO} = exp[\frac{16.288}{T^2} \times 10^3 - 9.34 \times 10^{-2}] \tag{2.1.5}$$

$$\alpha_{H_2^{18}O} = exp[\frac{11.839}{T^2} \times 10^3 - 28.224 \times 10^{-3}] \tag{2.1.6}$$

The model of equilibrium fractionation assumes that the two phases are in contact in a closed system and reach total equilibrium, as may occur within a well-mixed cloud during stratiform or convective precipitation formation. The fractionation due to condensation assuming total equilibrium is:

$$\frac{q_{ic}}{q_c} = \alpha(T)(\frac{q_{iv}}{q_v}) \tag{2.1.7}$$

where q_c and q_{ic} are the normal water mixing ratio and the isotopic water mixing ratio for the condensate, q_v and q_{iv} are the same for the vapour and $\alpha(T)$ is the fractionation factor at temperature T. For the open system, the Rayleigh distillation model for fractionation assumes that the condensate is instantly removed after formation, as may occur when solid condensate is formed during convection. The Rayleigh model also assumes that a constant fractionation factor may be used to describe the process. In this case, isotopic equilibrium exists only between the vapour and the newly formed condensate:

$$\frac{dq_{iv}}{dq_v} = \alpha(T)(\frac{q_{iv}}{q_v}) \tag{2.1.8}$$

Integrating from the initial mixing ratio (q_i, q) to the final state ($q_i^{'}$, $q^{'}$) and assuming that the fractionation coefficient is constant for the process, the following relation is obtained:

$$q_{ic}^{'} = q_{ic}^{'}(\frac{q_v^{'}}{q_v})^{\alpha} \tag{2.1.9}$$

The ratio of final to initial water mixing ratios $\frac{q_v^{'}}{q_v}$ is described as the rainout from the initial moisture, and according to the Rayleigh model, for a given initial isotopic ratio the resulting isotopic depletion depends only on the rainout. As condensation proceeds, the depletion of the vapour increases, producing greater instantaneous and total isotopic depletion of the precipitation compared with the total equilibrium case. Real physical processes will therefore lie between the two extreme cases of total equilibrium and Rayleigh distillation. The large variations in atmospheric water vapour and precipitation result from isotopic fractionation that occurs during evaporation and condensation. The fractionation factors, α = R_{liquid}:R_{vapour} under equilibrium conditions (relative humidity, RH = 100%) increase from 1.00937 to 1.0117 and from

1.0793 to 1.111 as temperature decreases from 25°C to 0°C for ^{18}O and ^{2}H respectively [45]. Thus water vapour in isotopic equilibrium with SMOW at 25^{o}C and RH = 100% has a δ^{18}O = -9.4‰ and δD = -79‰. Fractionation factors are larger for vapour-ice transitions (1.0152 and 1.1341 for ^{18}O and ^{2}H respectively at 0°C) [48, 49].

2.2 Non-equilibrium processes

When phase changes occur too rapidly for isotopic equilibrium to be established, fractionation must be described in terms of non-equilibrium effects. Under non-equilibrium conditions the extent of fractionation depends on the different rate of molecular diffusivity of the isotopic species compared with the normal water molecule, hence termed as kinetic fractionation or kinetic effects. Kinetic fractionation therefore differs from equilibrium fractionation which depends on the molecular weights of the different isotopic species and their resulting saturation vapour pressures. Kinetic effects occur during evaporation into an atmosphere with relative humidity of less than 100%, or where there are strong surface winds removing the vapour as it forms [50]. Kinetic fractionation is an important process in the micro-boundary layer above the ocean surface (influencing the initial isotope vapour values) and in clouds when forming snow and ice crystals at very low temperatures (below -20°C) where the atmosphere around the condensate will become super-saturated [51]. During the re-evaporation of falling rain drops below the condensation level, kinetic fractionation occurs in the atmosphere at the boundary layer between the liquid surface and the free atmosphere [52]. The evaporation flux E can be expressed:

$$E = \gamma\rho(q_s - q) \tag{2.2.1}$$

where ρ air density, specific air humidity in the atmosphere boundary layer q, and saturated specific air humidity air-water interface q_s. γ is the profile coefficient with $\gamma \propto$ to u (wind speed). The isotopic evaporation flux E_i can be expressed:

$$E_i = \gamma_i \rho (q_{si} - q_i) \tag{2.2.2}$$

with q_{si}=$R_s q_s$ and q_i=$R_v q$, R_s is the equilibrium vapour isotopic concentration (R_L=$\alpha_{L-V} R_s$), R_v is the resulting isotopic concentration in the atmospheric vapour. Combining equation (2.2.1) and equation (2.2.2) gives:

$$R_E = \frac{E_i}{E} \tag{2.2.3}$$

R_E is isotopic concentration in the evaporation moisture. Changing from absolute isotopic concentration to δ notation (relative deviation into ocean standard). The quantitative description of kinetic fractionation of δ in vapour (δ is either δ^{18}O or δD):

$$\delta = (1-k)[\frac{\frac{1}{\alpha} - h(1-\delta_\circ)}{1+h}] - 1 \tag{2.2.4}$$

where h=$\frac{q}{q_s}$ is (h relative air humidity), and $\delta_\circ$ vapour over the ocean surface. α is the equilibrium fractionation factor, and k the kinetic fractionation factor:

$$k = \begin{cases} 0.006 : \delta^{18}\text{O} \\ 0.00528 : \delta\text{D}, \ \|\upsilon_h\| < 7 \text{ m/s} \end{cases} \tag{2.2.5}$$

$$k = \begin{cases} 2.85\text{x}10^{-5} + 8.2\text{x}10^{-5} \text{ x } \|\upsilon_h\| : \delta^{18}\text{O} \\ 2.508\text{x}10^{-5} + 7.216\text{x}10^{-5} \text{ x } \|\upsilon_h\| : \delta\text{D}, \ \|\upsilon_h\| > 7 \text{ m/s} \end{cases} \tag{2.2.6}$$

where υ_h is horizontal wind speed.

The relationship between δ^{18}O and δD reflects the imprint of kinetic and equilibrium fractionation processes as noted by [43]. A linear relationship between the isotope

forms δ^{18}O and δD compositions in natural water derived from precipitation was identified and is known as the Global Meteoric Water Line (GMWL); δD = 8 $\times\delta^{18}$O + 10. From the δD-δ^{18}O relationship described by the GMWL, the second order parameter deuterium-excess (d) is defined as $d = \delta$D - 8 $\times$ δ^{18}O [44] in order to highlight potentially the variability of isotopic signal, which is not driven by equilibrium fractionation. Since equilibrium fractionation is temperature-dependent, the ratio of the two equilibrium fractionation factors $S(T) = \frac{\alpha_{2_H}-1}{\alpha_{18_O}-1}$ varies between 8.6 at 0°C and 7.7 at 30°C [45]. d can thus slightly change even under thermodynamic equilibrium conditions. Since non-equilibrium fractionation is intrinsically dominant during evaporation, d is an interesting variable for the study of surface evaporation and the associated meteorological conditions. In [43] reported that the global mean meteoric water has a d of 10‰, reflecting the fact that the ocean is generally out of equilibrium with the atmosphere. Equilibrium Rayleigh condensation processes roughly follow the GMWL slope of 8. In fact, those processes are responsible for the observed GMWL, and since d is defined as the offset from the GMWL, Rayleigh signals are greatly suppressed in d values. Diffusive transport contributes a significant role for greater fractionation in the light isotopes during non-equilibrium processes. Thus the deuterium excess in precipitation and atmospheric water vapour provides information about the role of diffusive transport in the boundary layer at the evaporative source and about source temperatures that cannot be obtained from δD or δ^{18}O individually.

The role of humidity

The evaporation process is driven by isotopic fractionation. The role of humidity on isotopic enrichment in evaporating water could be expressed as follows [53]:

$$\varepsilon^{18}O_{l-v} = 14.2(1-h) \tag{2.2.7}$$

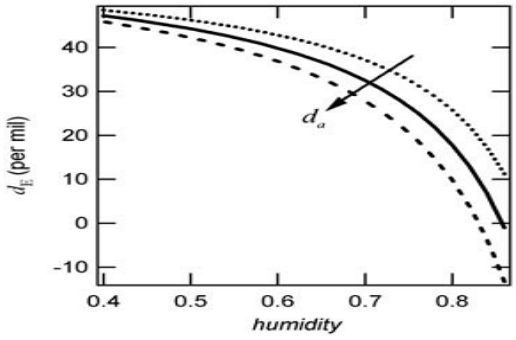

Figure 2.1: Deuterium excess (d) values calculated for the net evaporate as a function of humidity with $T_{surface} = 25^oC$. The solid line corresponds to δD_a = -86 ‰, $\delta^{18}O_a$ = -12 ‰, and d_a = +10 ‰. For the dashed line δD_a = -84 ‰ such that d_a = +12 ‰ and for the dotted line δD_a = -88 ‰ such that d_a = + 8 ‰, taken from [55].

$$\varepsilon^2 H_{l-v} = 12.5(1-h) \tag{2.2.8}$$

where $\varepsilon^{18}O_{l-v}$ and $\varepsilon^2 H_{l-v}$ are the fractionation factors of ^{18}O and ^{2}H, respectively, and h is relative humidity, the lower it is the faster the evaporation rate and the greater the kinetic fractionation. Humidity influences the isotopic composition of precipitation at every part of the hydrologic cycle; during air mass formation and their recharge along trajectories, in exchange with environmental humidity and evaporation below the clouds base [54]. For further elaboration see Fig 2.1 taken from [55].

Re-evaporation and exchange

As the condensate falls through vapour below the condensation level, it undergoes both molecular exchange with the surrounding vapour and evaporation of some of the condensate [52, 56]. Diffusive molecular exchange occurs with isotopically heavier

vapour near the ground, leading to an enrichment relative to the initial precipitation. The extent of exchange will be diminished as the isotopic ratio of the lower level vapour decreases and approaches that of the condensate. Thus during more extensive precipitation events the enrichment due to exchange is reduced. Additional isotopic fractionation occurs as some of the condensate evaporates while passing through non-saturated layers below the formation level, leading to an isotopic enrichment of the condensate. Re-evaporation is believed to occur with non-equilibrium kinetic effects when the surrounding atmosphere has a very low relative humidity and hence the re-evaporation is too rapid to be able to reach the equilibrium [52]. No fractionation will occur for re-evaporation of solid condensate due to the extremely slow rate of molecular diffusion in the solid phase (10 - 14 m^2s^{-1} at 0°C) [51].

2.3 Precipitation behavior and correlated effects

Obviously phase changes in the hydrologic cycle drive the isotopic characterization of its different compartments. Water vapour forming precipitation will be depleted in heavy molecules ($H_2^{18}O$ and HDO) with respect to the ocean water. The inverse process happens during condensation forming rain drops. Water molecules depend on the different environmental conditions occurring during their history. In 1961, the International Atomic Energy Agency (IAEA) and the World Meteorological Organization (WMO) started a world-wide survey on the isotopic composition of global precipitation. Using the first data of the IAEA/WMO network, the degree of depletion of heavy isotopes is connected to geographical parameters, such as latitude, altitude, distance from the coast, surface air temperature and amount of precipitation are determined [44]. All of these effects are bound to the degree of rain-out of

moisture from any air mass.

Latitude effect

Based on the IAEA/WMO database, the influence of latitude on the stable isotopic composition of precipitation is evident by more depleted values in stations at higher latitudes. This is because the tropical ocean is the most important reservoir of water vapour which, under the guide of poleward transport, undergoes subsequent condensation along the latitudinal gradient of air temperature [57].

Continental effect

A depletion in stable isotopes is observed at continental stations compared to coastal stations at a similar latitude. This is particulary true at mid and low latitudes [57]. In some cases this continental gradient differs from place to place and, in the same place, during different periods of the year. The latter is principally due to the re-evaporation of precipitation in summer.

Altitudinal effect

The altitudinal effect is particularly important for hydrological and hydrogeological applications. It consists of a gradual depletion in heavy isotopes with increasing altitude. The isotopic data generally show a linear correlation with altitude; the magnitude of the effect and the relative gradients depend on local parameters such as topography and climate (i.e. temperature).

Amount effect

The relationship between the amount of precipitation and stable isotope data ($H_2^{18}O$ and HDO) is first highlighted [44] report, noting a depletion in isotopes with increased precipitation. This is well rendered in the tropics, where precipitation is very abundant, the correlation will be different at different altitudes evidently because the amount effect is a direct result of the adiabatic condensation process. It was obtained a gentle slope at low altitude, where precipitation derives from the first stages of condensation and is also affected by the recycled vapour of evapotranspiration [58, 59]. In other instances the amount effect is not too consistent and other factors seem to influence the isotopic composition of precipitation, such as meteorological conditions at the time of precipitation and the origin of air masses. Small amounts of rain are, as a rule, enriched in the heavy isotopes along typical evaporation lines, especially in the more arid regions [60].

Chapter 3

Instrumentations, models, and site descriptions

For this study, we have used several datasets that have been derived from various instruments on different platforms and model simulations. Thus, the data are having varying degrees of spatial coverage, horizontal and vertical resolutions, temporal resolution, and time continuity. Obviously, to some extent, these differences have caused an influence on the interpretation of water vapour variability at various atmospheric layers. The analysis provided in this thesis is accounted the discrepancies among instruments. Descriptions about the instruments and the model techniques, as well as site descriptions are provided in the following sections.

3.1 Instrumentations

3.1.1 FTIR spectrometer

The BRUKER interferomenter is based on the IFS-120M model but upgraded with the new electronics of the model IFS-125M. The FTIR spectrometer has two detectors: mercury-cadmium-telluride (Hg−Cd−Te) and indium antimonide (InSb), which allow coverage of the 600−1500 and 1500−4400 cm^{-1} spectral intervals, respectively. Recently, a new laser source with power supply has been mounted on this interferometer in order to improve the laser signal that reaches the detector to attain stable movement of the optics. The applied spectral resolution is in the order of 0.009 to 0.0085 cm^{-1}. FTIR spectrometer makes direct solar absorption measurements throughout the day, under clear sky conditions. The spectra are constructed by coadding 10 scans recorded in about 8 minutes. FTIR at Addis Ababa is planned to be part of NDACC (Network for Detection of Atmospheric Composition Change) network that has been monitoring long term atmospheric composition changes. The FTIR data set used for this study covers the time period from 01 June, 2009 to 11 March, 2013, which contains about 186 days of measurements. To minimize the effect of instrumental artifacts on the retrieved profiles cell measurements are made and analyzed with LINEFIT software [61]. More details about these measurements are reported in [62]. This FTIR spectrometer is installed in college of science, Addis Ababa University. Currently, FTIR is being operated by the Department of Physics, Addis Ababa University in collaboration with Karlsruhe Institute of Technology (KIT), Germany.

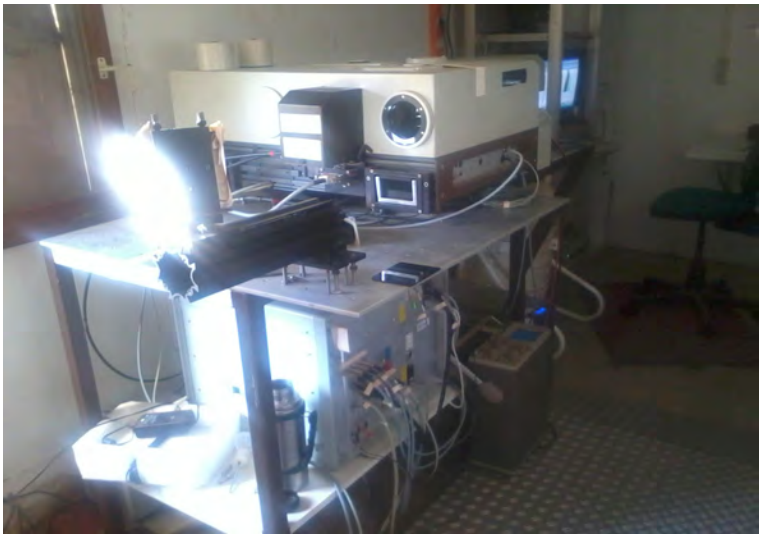

Figure 3.1: The FTIR spectrometer at measurement site in Addis Ababa.

3.1.2 Atmospheric Infrared Sounding (AIRS)

The Atmospheric Infrared Sounder (AIRS) was launched into Earth orbit on 4 May 2002 on board the Aqua satellite, part of the NASA Earth Observing System [63]. Owing to demand on high spatial resolution humidity observations, AIRS provides twice daily atmospheric profiles over the most parts of the globe. It is a high-spectral resolution infrared sounder instruments for measuring the atmospheric water vapour. The IR spectral channels used in AIRS are in the range of 3.74 to 15.4 μm with an accuracy of 3%. At nadir, the spatial resolution of the IR channels is 13.5 km from the orbital altitude of 705 km. Water vapour amount is retrieved at twelve standard pressure levels between the surface and 100 hPa, though sensitivity is low for mixing ratios of about 10 ppmv or less [64, 65]. AIRS water vapour retrievals have been validated with aircraft and balloon in situ measurements [64, 66, 67] and MLS [65]. AIRS

level 3 version 5 H_2O product has been used in the analysis. Further details about the overview of AIRS instruments can be found in [68] and at http://disc.gsfc.nasa.gov.

3.1.3 Tropospheric Emission Spectrometer (TES)

The Tropospheric Emission Spectrometer (TES) launched into sun-synchronous orbit on aboard Aura, the third of NASA's Earth Observing System (EOS) spacecraft, on 15 July 2004. TES is an infrared Fourier transform spectrometer (FTS) that measures the spectral infrared (IR) radiances between 650 cm^{-1} and 3050 cm^{-1} in a limb-viewing and a nadir (downward looking) mode. The observed IR radiance is imaged onto an array of sixteen detectors that have a combined horizontal footprint of 5.3 km by 8.4 km in the nadir viewing mode. In the nadir view, TES estimates of atmospheric distributions provide vertical information of the more abundant tropospheric species such as H_2O, HDO, O_3, CO, and CH_4 [38, 69]. However, sufficient spectral resolution and signal-to-noise ratio are required to distinguish between trace-gas amounts at different altitudes because vertical information about trace gas concentrations is obtained only from spectral variations along the line-of-sight. Therefore, the TES spectral resolution was chosen to match the average pressure-broadened widths of weak infrared molecular transitions in the lower troposphere for nadir measurements (0.06 cm^{-1} apodized) [70]. The vertical resolution and error characteristics for the HDO/H_2O estimates from TES are discussed in detail in [38]. Under clear-sky conditions in the tropics, TES estimates of the HDO/H_2O ratio are sensitive to the distribution of the actual ratio from the surface ($\sim$1000 hPa) to about 300 hPa with peak sensitivity at 700 hPa [71] and references therein. Standard products are provided in Level 2 and Level 3. Level 2 data are the retrieved atmospheric species

profiles at the nadir footprint or the limb tangent. The Level 2 processing is to retrieve atmospheric temperature and species profiles via iteratively fitting an atmospheric radiative transfer model results with the observed spectral radiances (Level 1B data) considering the measurement noise and some known characteristics of the atmospheric parameters. The Level 2 data are the inputs to Level 3 processing. The Volume Mixing Ratio (VMR) for chemical species is reported with respect to dry air. The vertical pressure levels of Level 2 data are UARS standard levels, defined as $P = 1000.0x10^{\frac{-k}{6.0}}$, (hPa), where constant $k = 0, 1, 2,..$ The data granule for Level 2 data is a "daily" (actually 16 orbits) file per species. It includes time dependent data, such as the geolocations, solar zenith angles, and total column data etc., and the time-pressure dependent profile data. The retrieval errors are also provided for the profiles. Level 3 data are the "daily", "8-day", and "monthly" species profile (or the surface parameter and total column etc.) data interpolated into uniform longitude-latitude grid. A common grid of 4^o longitude by 2^o latitude for Level 3 data is applied for all four instruments on the Aura spacecraft. In this study, both TES Level 2 and Level 3 products are used when the degree of freedom for signal (DOFS) is higher than 0.5, to ensure a significant sensitivity to the true state [38]. Further information about the products can be in the document (http://tes.jpl.nasa.gov).

3.1.4 Microwave Limb Sounder (MLS)

The Earth Observing System (EOS) Microwave Limb Sounder (MLS) is one of four instruments on the NASA's EOS Aura satellite, launched on July 15, 2004 into a near polar sun-synchronous orbit at 705 km altitude, allowing samplings at nighttime at 01:30 local time (LT) and at daytime at 13:30 LT at the equator [72]. The

Aura-MLS instrument, calibration and performance for the different channels are described [73, 74, 75]. It scans the Earths limb providing 240 scans per orbit, spaced ∼165 km along the orbit track, and ∼3500 vertical profiles per day for 17 primary atmospheric parameters: pressure, temperature and cloud ice water content, as well as 14 trace constituents such as O_3, H_2O and CO, with near pole-to-pole daily global latitudinal coverage from 82^{o}S to 82^{o}N. MLS measures thermal emission lines from limb, using seven radiometers to provide coverage of five spectral regions between 118 GHz and 2.5 THz, during both day and night. The retrieval scheme is based on the Optimal Estimation Method [76]. In this study, the Level 2 (L2) version 3.3 (v3.3) water vapour (H_2O), temperature (T) and ice water content (IWC) profiles from MLS are used.

The MLS H_2O version 2.2 (v2.2) products have been validated [77, 78], but the differences between v2.2 and v3.3 used here are minor in the tropics at the TTL pressure levels (< 10 %). From the UT (220 hPa) to the LS (31 hPa), the precision and accuracy range from 40 to 6 % and from 25 to 4 %, respectively, for a vertical resolution from 2.5 to 3.2 km, although the entire useful pressure range spans from 316 to 0.002 hPa [79]. Note that a data screening as suggested in [79] has been applied.

The v3.3 IWC product used here is derived from MLS cloud-induced radiances as detailed in [80]. It has a 3 km vertical resolution, a 1.2 to 0.07 m gm^{-3} precision and a 100-150 % accuracy in the pressure range 215-83 hPa where they are reliable. As suggested in [79], the screenings consisting in a temperature profile filter [81] and a screening method described in [82] have been also applied.

The v3.3 temperature, very similar to the v2.2 described in [81], has a useful domain

ranging from 261 to 0.001 hPa. In the layer of interest for our study, from 220 to 31 hPa, the vertical resolution ranges from 5 to 3.6 km, the precision from ± 1 to ± 0.6 K and the accuracy is about ± 2 K [79]. An adequate screening has been also applied following [79].

3.1.5 Moderate Resolution Imaging Spectro-radiometer (MODIS)

The MODIS is a key scientific instrument aboard the Terra (EOS AM) and Aqua (EOS PM) satellites. MODIS Terra covers the globe every 1-2 days, provides data in moderate spatial resolution (250 m at nadir) with swath width (2330 km), and large spectral range (36 channels between 0.412 to 14.2 μm. Here cloud fraction data [83] from Level-3 MODIS terra (MOD08_M3 http://modisatmos.gsfc.nasa.gov) monthly basis of gridded product available at spatial resolution of 1 degree are used.

3.1.6 Advanced Very High Resolution Radiometer (AVHRR)

Outgoing Longwave Radiation (OLR) is measured by the National Oceanic and Atmospheric Administration (NOAA) Advanced Very High Resolution Radiometer (AVHRR) sensors. Interpolated data [84] are taken from the NOAA-CIRES Climate Diagnostics Centre web site http://www.cdc.noaa.gov, from the NOAA 16 series of satellites. Data are binned within boxes of 2.5^o latitude x 2.5^o longitude. The OLR is a measure of the thermal infrared radiation that escapes from the top of the Earths atmosphere back into space. Cold, high clouds radiate low values of OLR while warm, low clouds, ocean and land surfaces in the tropics radiate high values of OLR. Cumulonimbus clouds, representative of deep convection, have high cold tops and they radiate little longwave radiation to outer space. Regions with low OLR are therefore

associated with deep convection. Areas of OLR with values less than 236 and 220 W m^{-2} can be considered as an estimation of the convective outflow location in the middle (∼400 hPa) and in the upper (∼100 hPa) tropical troposphere, respectively.

3.2 Models and data

3.2.1 IsoGSM

The simulated a multi-decadal and globally three-dimensional stable water isotope data (IsoGSM, Isotopic Global Spectral Model, http://www.ccsr.u-tokyo.ac.jp/∼kei) set by introducing isotopic fractionation process into up-to-date version of the Scripps Experimental Climate Prediction Center's Global Spectral Model (ECPC's GSM [85]) and applying spectral nudging toward the meteorology captured by the National Centers for Environmental Prediction (NCEP) Reanalysis. The model's physics packages include longwave and shortwave radiation [86], relaxed Arakawa-Schubert convective parameterization [87], non-local vertical diffusion [88], mountain drag [89], shallow convection [90], and the Noah land surface scheme [91]. Unlike the global model calculations forced only by sea surface temperature, this model is driven by observed atmospheric circulation, thereby improving the agreement between observed and modeled isotope variations. Therefore, the simulated isotopic fields are reasonably accurate over the entire globe ranging from daily to inter-annual time scale. This model is useful in providing information in regions where in-situ isotope observations are not available, which is required for a variety of biogeochemical, hydrological and paleoclimate studies [92]. It can provide the simulated water vapour with nudged or not nudged (free run) options. The free run model output remains its own hydrological

cycle. The nudging technique adjusts the model dynamics to the actual short-term synoptic scale situation and allows an adequate simulation of day-to-day as well as inter-annual variability. IsoGSM has been used with TES data [6] to understand below cloud effects on the isotopic composition of precipitation and water vapour [93].

In addition, the comparisons of the water vapour isotopologues from IsoGSM have been extensively evaluated against other isotopic atmospheric general circulation models (AGCMs), as well as instruments from different platforms, such as space-based and ground-based. For instances, it has been reported that the IsoGSM isotope simulations are evaluated against TES [94] and SCHIAMACHY [31, 94] spectroscopic satellite isotope data. As reported in [94], an overall consistency was found between the model and the satellite observations, but there were some discrepancies. However, the uncertainty in the satellite δD measurements remains large enough that they cannot be used to diagnose the potential shortcomings in the model. IsoGSM simulations have also been compared to ground-based isotope observations. For example, investigation of the IsoGSM's performance using isotope data acquired by a fourier transform infrared spectroscopy (FTIR) network are reported in [**?**]. These authors reported that a systematic discrepancy exists between observed and modeled amplitude in seasonal cycles of δD values. Therefore, these facts are sufficient to build a confidence to utilize the IsoGSM model simulations for scientific applications in this study.

3.2.2 Modular Earth Submodel System (MESSy)

Recent approaches towards Earth System Modeling follow a top-down approach, coupling existing models of different domains (land, ocean, atmosphere, etc) by means

of a universal coupler. Yet, to study the interactions between bio-physico-chemical processes, the internal complexity of every domain specific model itself must be controllable in a transparent and user friendly way. The Modular Earth Submodel System provides as complementary to the domain couplers a bottom-up approach, including a generalized interface structure for the standardized control of submodels and their interconnections. This gives remarkable new possibilities to study feedback mechanisms. MESSy is an interface with infrastructure to couple 'processes' (as submodels) to a GCM (as base model) a set of processes coded as switchable submodels a coding standard. In this study, we have used MESSy simulated water vapour that has been derived by nudging with ECMWF ERA-interim reanalysis wind fields data for meteorological fields. Further details about MESSy can be found in [95, 96, 97].

3.2.3 ERA-Interim reanalysis data

Specific humidity, relative humidity (RH), moisture flux fields derived from primary parameters of specific humidity and wind components obtained with the European Center for Medium range Weather Forecasting (ECMWF) ERA-Interim reanalysis dataset have been used in this thesis. These parameters derived from ECMWF are used for making the cross-comparison to the co-located observations and diagnose the variability of moisture at seasonal time scale over the domain of interest. The data are available on a 1.5° latitude by 1.5° longitude and variable vertical resolution in pressure level with a temporal resolution of six hours. Other features of the data can be obtained in [98].

Table 3.1 Summary of the characteristics of the instruments of H_2O addressed in this study.

	Instruments			
	FTIR	TES	AIRS	MLS
Platform	Ground-based	Satellite	Satellite	Satellite
Observation geometry	upward	nadir	nadir	limb
Observation mode	absorption	emission	emission	emission
Vertical resolution (km)	∼9-15	∼2-6	2-7	2.5-3.2
Spectral resolution	0.009 cm^{-1}	0.06 cm^{-1}	0.5-2cm^{-1}	696 MHz
Spectral domain	600-4400 cm^{-1}	650-3050 cm^{-1}	650-2700 cm^{-1}	∼80,000 cm^{-1} (∼240 GHz)
Standard data versions	H_2O	H_2O (level 2 ver05 and level 3 ver02)	H_2O level 3 ver05	H_2O level 2 ver3.3

Table 3.2 Models used in this study and their respective simulations.

Models	studied for type of species	Simulations	Reference
MESSy	for H_2O species only	nudged by ECMWF era-interim	
IsoGSM	both for H_2O and HDO species	free-running	Yoshimura et al. [2008]

"Free-running" refers to simulation that has been forced by observed sea surface temperatures, and whose winds are not nudged.

3.3 Measurement site description

Addis Ababa is located at 9.01^{o}N latitude, 38.76^{o}E longitude, 2443 m altitude above sea level, which is in the equatorial region. It is relatively dry due to its topography, making it robust for monitoring trace gas species in the tropics. Indeed, high altitude mountain sites have long been recognized as good places for atmospheric composition measurements. Primarily influenced by distant sources, such sites can be used to make measurements which are representative of the global average concentration [99], also known as the baseline [100]. But local sources can also be important, depending largely on the recent history of vertical transport and associated mixing. The typical tropopause height for tropical regions is ranging between 16 to 18 km, and the corresponding temperature is about 200 K. The tropical tropopause region is the transition layer between the dynamical control of the vertical mass flux by tropospheric convection, and by the stratospheric Brewer-Dobson circulation [101, 102]. Thus, the site is highly affected by tropical dynamics allowing us to understand processes that modulate tropical dynamics from the observed variation in the measurement of atmospheric trace gases. The modern climate of Ethiopia region is mainly characterized by alternating wet and dry seasons following the annual movements of the Intertropical Convergence Zone (ITCZ). Thus, Ethiopia experiences generally southwesterly moisture laden air from South Atlantic and Indian Ocean during northern summer whereas it is under the influence of dry continental northeasterly winds during northern winter. The detailed climatology of the region is described by [103] and references therein. Therefore, this FTIR site is also ideal to observe seasonal variation as ITCZ migrates north-south with season across the site.

Chapter 4

Retrieval procedure for water vapour isotopologues

Remote sensing techniques are an indirect method, which are currently widely used for deriving atmospheric parameters, such as temperature, pressure, and concentration of trace gases based on direct measurement of radiation emitted, absorbed and scattered by the atmosphere. Our ground-based high-resolution Fourier transform infrared (FTIR) spectrometer is employed the remote sensing techniques to obtain the abundance of atmospheric trace gases. Therefore, the measurement principle of the solar spectra and the retrieval techniques, particularly, for water vapour isotopologues (H_2O, HDO) which are the important species in this study, are discussed as follows.

4.1 Forward radiative transfer model

Remote sensing observations are only possible due to the transfer of radiation through the atmosphere to the instrument. The radiation arriving at an observing instrument is the sum of radiation entering the atmosphere in the field of view of the instrument and that emitted or scattered by trace gases, aerosol or by cloud into the beam of radiation. The intensity, or radiance, of the beam of energy originating from the point can be attenuated within a differential thickness ds by:

$$dI_\nu = -e_\nu n_a I_\nu ds \tag{4.1.1}$$

where e_ν is the molecular extinction coefficient that characterizes the radiation matter interaction (including both absorption and scattering), and n_a is the number density of absorbing molecules. In a path ds, the absorbing or scattering molecules may also contribute to the incident radiation through emission. The increase in radiance traveling through the path ds is then given by:

$$dI_\nu = j_\nu n_a ds \tag{4.1.2}$$

where j_ν is the emission coefficient, which characterizes the emission properties of the molecules in the path. Assuming that the atmospheric layer is in local thermodynamic equilibrium (LTE) at a given temperature T, Kirchhoff's law can be used to relate states that the emission and absorption coefficients, j_ν and e_ν:

$$\frac{j_\nu}{e_\nu} = f_\nu(T) \tag{4.1.3}$$

where J_ν source function. Therefore, equation 4.1.2 can be rewritten:

$$dI_\nu = e_\nu n_a J_\nu ds \tag{4.1.4}$$

Combining extinction and emission gives net change in radiance which is expressed as:

$$\frac{dI(P,s)}{ds} = -e_\nu n_a[I_\nu(P,s) - J_\nu(P,s)] \tag{4.1.5}$$

where $I_\nu(P,s)$ defines the radiance at a point P in an arbitrary direction s. This is Schwarzchild's radiative transfer equation. This radiative transfer equation at the point P' at a distance s can now be written as:

$$\frac{dI_\nu(s',s)}{d\tau_\nu} = [I_\nu(s',s) - J_\nu(s',s)] \tag{4.1.6}$$

where τ_ν is defined as a positive quantity as $s > s'$. As a linear first-order differential equation with constant coefficient, the necessary integrating factor is $exp(-\tau_\nu)$. After integration using $\tau_\nu = 0$, at the origin s_o:

$$I_\nu(s',s) = I_\nu(s_o,s)exp[-\tau(s_o,s)] + \int_o^{\tau(s_o,s)} J_\nu(s',s)exp[-\tau(s',s)]d\tau_\nu \tag{4.1.7}$$

Equation 4.1.7 solves the radiative transfer problem if the source function $J_\nu(P',s)$ at a point P' and direction s is known. Under local thermodynamic conditions the source function is given by the Planck function, $B_\nu(T)$. The Planck function is given by:

$$B_\nu(T) = \frac{2h\nu^3}{c^2}\frac{1}{[exp(\frac{h\nu}{k_BT}) - 1]} \tag{4.1.8}$$

where h is Planck's constant, and k_B is the Boltzmann constant. At a given frequency, the source function depends only on temperature T, if the gas is in thermodynamic equilibrium. Different gas properties emitting and absorbing radiation at frequency ν are contained in their absorption or emission coefficient. One can also use transmission model equally well to describe the measurement $e^{-\tau}$ is the total transmission between

the points corresponding to optical path $\tau = 0$, the top of atmosphere, and $\tau = \tau$, at the site of the instrument. The radiative transfer model in terms of total transmission has the form:

$$I_\nu(t) = B_\nu(T_s)t \tag{4.1.9}$$

It is then noted that attenuation of radiation between arbitrary atmospheric layers bounded by s' and s is described as:

$$I_\nu(t) = B_\nu(T_s)\int_{s'}^{s} \frac{\partial t}{\partial s"} ds" \tag{4.1.10}$$

where now t is the total transmission after being attenuated by gases within layers bounded by $s"$ and $s" + ds"$. This is the general model for which explicit functional form of τ is not given, however, recalling the definition of optical thickness, the transmission can expressed as a function of s':

$$t_\nu(s', s) = exp(-\int_{s'}^{s} k_\nu(s")n_a(s")ds") \tag{4.1.11}$$

As there are many absorber along the optical path, the absorption cross-section is weighted and given as:

$$k_\nu(s') = \sum_{m=1}^{M} k_{\nu(m)}(s')y_m(s') \tag{4.1.12}$$

where $y_m(s')$ and $k_{\nu(m)}(s')$ denote volume mixing ratio (VMR) and absorption cross section, respectively, of the species m of the total number M of different molecular species that absorb in the spectral region under consideration. Then, by substituting equation(4.1.12) into equation(4.1.7), the equation expressed as follows:

$$I_\nu(s', s) = I_\nu(s_o, s)exp[-\int_{s_o}^{s} \sum_{m=1}^{M} k_{\nu(m)}(s')y_m(s')\rho(s')ds'] \tag{4.1.13}$$

Dividing the above equation by $I_\nu(s_o, s)$, gives:

$$\frac{I_\nu(s', s)}{I_\nu(s_o, s)} = exp[-\int_{s_o}^{s} \sum_{m=1}^{M} k_{\nu(m)}(s')y_m(s')\rho(s')ds'] \tag{4.1.14}$$

Furthermore, as the molecular species m may have several transitions which have different temperature and pressure dependence, the absorption cross-section of one molecular species m as a function of temperature and pressure is given by the following sum over all lines of the species (more details on the above discussion can be found in [104, 105, 106].

$$k_{\nu(m)}(T,P) = \sum_{l=1}^{lines} S_{m,l}(T) g_{m,l}(\nu - \nu_{m,l}, T, P) \tag{4.1.15}$$

where $g_{m,l}(\nu - \nu_{m,l}, T, P)$ is line shape function and $S_{m,l}(T)$ is spectral line strength.

4.2 Retrieval technique

The retrieval of atmospheric parameters from remote sensing data requires accurate calculations that determine the received radiation for specific atmospheric conditions, since the sensor measures the radiation which is the complicated functions of the quantities of interest. Spectrally resolved or integrated radiance signal recorded by the instrument is described as:

$$\mathbf{y} = \mathbf{F}(\mathbf{x}, \mathbf{p}) + \epsilon_y \tag{4.2.1}$$

where $\mathbf{y}$ is the vector of the measured intensities for certain frequencies, $\mathbf{x}$ is the vector of the intended constituent profiles, $\mathbf{p}$ a set of model parameters comprising quantities that influence the measurements and are known to some accuracy, e.g. the relationship between altitude, pressure and temperature, ϵ_y the measurement error and $\mathbf{F}$ is the forward model which provides a physical description of the measurement process and a numerical process that provides a simulation of the radiative transfer in the experiment. Thus, the inversion of the radiative transfer equation is required to

implement it for remote sensing applications. This requires a numerical approach, as there is no analytical solution. In general, retrieval of atmospheric parameters from measured spectra is an ill-posed inverse problem with non-uniqueness and unstable solution [107, 76, 108]. An inverse (or retrieval) method $\mathbf{R}$ has to be applied to the measurement vector in order to retrieve an optimal estimate $\hat{\mathbf{x}}$ of the state vector $\mathbf{x}$, i.e.,

$$\hat{\mathbf{x}} = \mathbf{R}(\mathbf{y}) \tag{4.2.2}$$

The retrieval algorithm selects values for state vector $\mathbf{x}$ at the i^{th} which minimizes the quantity χ^2, defined as:

$$\chi^2 = [\mathbf{y} - \mathbf{F}(\mathbf{x}, \mathbf{p})]^T \mathbf{S}_y^{-1} [\mathbf{y} - \mathbf{F}(\mathbf{x}, \mathbf{p})] \tag{4.2.3}$$

where $\mathbf{S}_y$ is the error covariance matrix of the spectral radiance measurement vector $\mathbf{y}$ and $\mathbf{F}$ is the forward model. This cost function is minimized iteratively by a Gauss-Newton method, and the state vector $\mathbf{x}$ at the $(i+1)^{th}$ iteration is:

$$\mathbf{x}_{i+1} = \mathbf{x}_i + (\mathbf{K}_i^T \mathbf{S}_y^{-1} \mathbf{K}_i)^{-1} \mathbf{K}_i^T \mathbf{S}_y^{-1} (\mathbf{y} - \mathbf{F}(\mathbf{x}_i)) \tag{4.2.4}$$

where $\mathbf{K}$ is the matrix of weighting function or Jacobians. There are aspects of the state vector about which the measurement has been unable to provide any information because of the occurrence of singularity during inverting the matrix. This singularity can be avoided by including a constraining second term in 4.2.3:

$$\chi^2 = [\mathbf{y} - \mathbf{F}(\mathbf{x}, \mathbf{p})]^T \mathbf{S}_y^{-1} [\mathbf{y} - \mathbf{F}(\mathbf{x}, \mathbf{p})] + (\mathbf{x} - \mathbf{x}_a)^T \mathbf{S}_a (\mathbf{x} - \mathbf{x}_a) \tag{4.2.5}$$

where $\mathbf{S}_a$ is apriori covariance matrix which is used as regularization matrix and $\mathbf{x}_a$ is the a priori profile. Now the iterative solution is:

$$\hat{\mathbf{x}}_{i+1} = \hat{\mathbf{x}}_i + (\mathbf{K}_i^T \mathbf{S}_y^{-1} \mathbf{K}_i + \mathbf{S}_a + \lambda \mathbf{I})^{-1} (\mathbf{K}_i^T \mathbf{S}_y^{-1} [\mathbf{y} - \mathbf{F}(\hat{\mathbf{x}}_i)] - \mathbf{S}_a (\hat{\mathbf{x}}_i - \mathbf{x}_a)) \tag{4.2.6}$$

where $\lambda\mathbf{I})^{-1}$ is the damping term for attaining the convergence [109, 110].

The analysis of solar absorption spectra derived from ground-based FTIR spectrometer has been done by the retrieval algorithm of PROFFIT (PROfile FITing) [111], which has been used by the ground-based FTIR scientific community. The code simulates the spectra and the Jacobians by the line-by-line radiative transfer model PRFFWD (PRoFit ForWarD model) [111, 112]. It includes a ray tracing module [113] in order to precisely simulate how the radiation passes through the atmosphere. The vertical structure of the atmosphere is discretised and the amount of the absorber $\mathbf{x}$ at altitude level z can be described in form of a vector $\mathbf{x}$(z). Similarly the radiation spectrum is discretised and described by a vector $\mathbf{y}$ containing the radiances at the different spectral bins. PRFFWD accounts for the forward radiative transfer model ($\mathbf{F}$), which connects the spectrum ($\mathbf{y}$) to the vertical distribution of the absorbers ($\mathbf{x}$) and to parameters ($\mathbf{p}$) describing the state of the atmosphere and instrumental characteristics.

PROFFIT provides options to perform retrieval either on the basis of linear or logarithmic scale. This option has proven to be very beneficial for tropospheric water vapour retrievals. The reason is that tropospheric water vapour concentrations are log-normally, rather than normally, distributed [114]. The inversion algorithm is able to fix apriori value for the measurement noise by taking the residuals of the spectral fit itself. Tikhonov-Phillips regularization method [115, 116] is applied during the inversion of the FTIR spectra. Moreover, PROFFIT supports retrieval options that are essential for the remote sensing of isotopologue ratios. The HDO/H_2O ratio constraint is essential for obtaining an appropriate tropospheric HDO/H_2O estimate. The reason is that the H_2O and HDO kernels are rather different and tropospheric H_2O and

HDO distributions are very inhomogeneous [3, and references therein]. Daily pressure and temperature profiles used in the retrievals are taken from the automailer system of Goddard Space Flight Center. Our apriori VMR profiles are from the Whole Atmosphere Community Climate Model (WACCM, http://www2.cesm.ucar.edu/working-groups) as recommended by the NDACC/IRWG (Infrared Working Group). WACCM is a numerical model developed at the National Center for Atmospheric Research (NCAR). The HDO apriori profile is generated from the WACCM H_2O apriori profile using an empirically derived isotopic fractionation equation as given below:

$$HDO = 0.16 H_2O\ (VMR)\ (8.0 + \log(H_2O\ (VMR))) \tag{4.2.7}$$

At the tropopause (H_2O (VMR) = 3x10^{-6}) this equation gives $\frac{HDO}{H_2O} = 0.4$, whereas in the humid lower troposphere (H_2O (VMR) = 1x10^{-2}) the equation gives $\frac{HDO}{H_2O}$ =0.96. The retrieval of H_2O and HDO profiles are performed on a logarithmic scale and also employed inter-species constraints in order to obtain optimal estimation of δD profiles, details are provided in [3, 117].

As discussed in [76], the Optimal Estimation Method allows the characterization of the retrievals, i.e., the vertical resolution of the retrieval, its sensitivity to the apriori information and degree of freedoms for signal (DOFs) are quantitatively described. The retrieved state vector $\hat{\boldsymbol{x}}$ related to the apriori and the true state vectors $\boldsymbol{x}_a$ and $\boldsymbol{x}$, are given as:

$$\hat{\boldsymbol{x}} = \boldsymbol{x}_a + \hat{\mathbf{A}}(\boldsymbol{x} - \boldsymbol{x}_a) + error\ terms \tag{4.2.8}$$

respectively, where $\hat{\mathbf{A}}$ is averaging kernel matrix. The actual averaging kernels matrix depends on several parameters including the solar zenith angle, the spectral resolution and signal to noise ratio, the choice of retrieval spectral microwindows, and the apriori

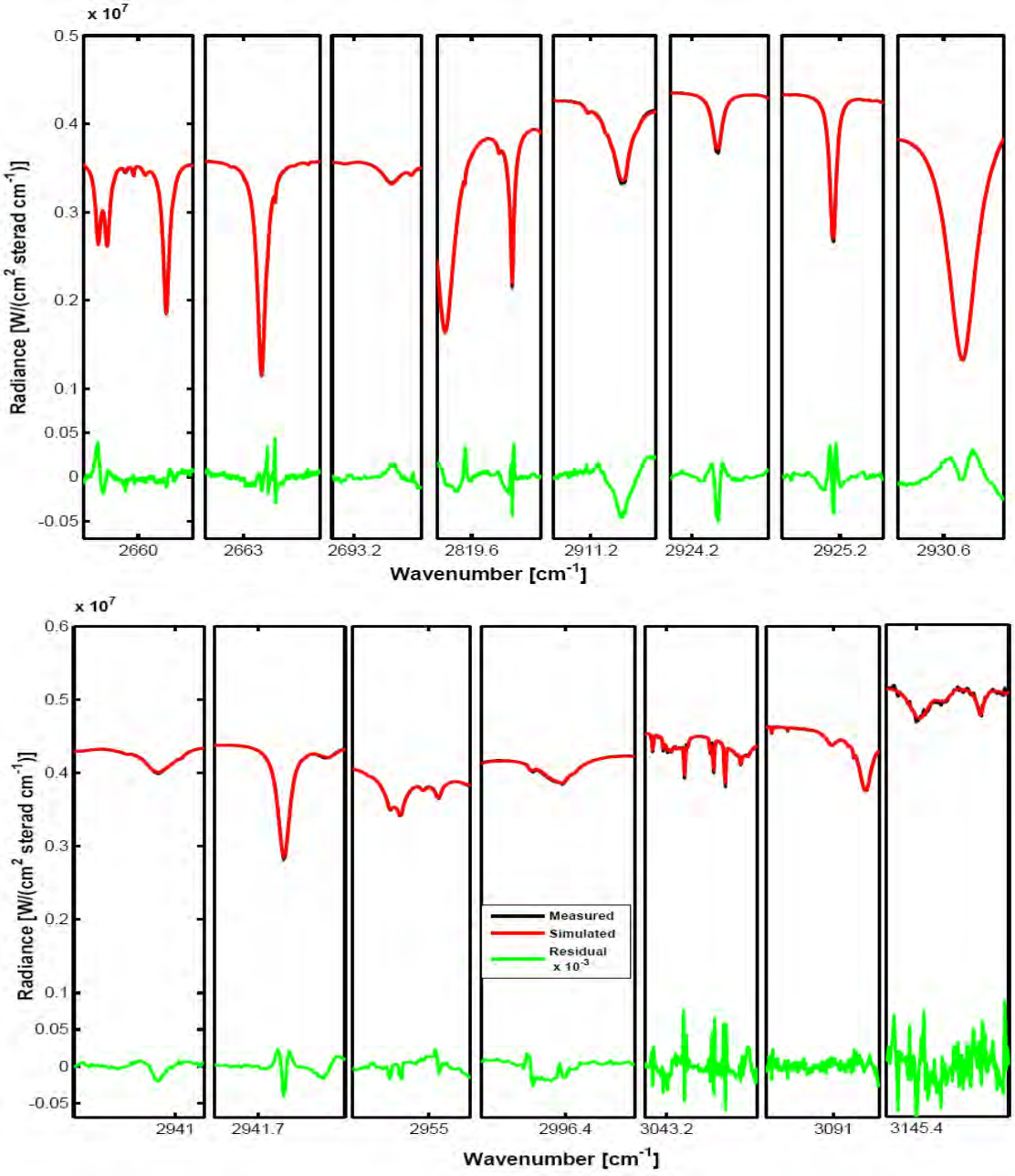

Figure 4.1: Spectral microwindows used for the ground-based FTIR retrievals. Shown is an example for a typical measurement at Addis Ababa (12 December 2012, 11:45 UTC; DOFS for H_2O: 2.14). Black line: measurement; red dashed line: simulation; blue line: residual (difference between measured and simulated).

covariance matrix $\mathbf{S}_a$. The elements of the averaging kernel for a given altitude give the sensitivity of the retrieved profile at that altitude to the real profile at each altitude, and its full width at half maximum is a measure of the vertical resolution of the retrieval at that altitude. Error estimation analysis is based on the analytical method suggested by [76]:

$$\hat{\boldsymbol{x}} - \boldsymbol{x} = (\hat{\mathbf{A}} - \mathbf{I})(\boldsymbol{x} - \boldsymbol{x}_a) + \hat{\mathbf{G}}\hat{\mathbf{K}}_p(\boldsymbol{p} - \hat{\boldsymbol{p}}) + \hat{\mathbf{G}}\epsilon \tag{4.2.9}$$

where $\hat{\boldsymbol{p}}$, $\boldsymbol{p}$ are the estimated and real model parameters, respectively, $\hat{\mathbf{G}}$ is the gain matrix, $\hat{\mathbf{K}}_p$ is the model parameter sensitivity matrix and ϵ represents noise. The first term in Eq.(4.2.9) represents the smoothing error. The second term stands for the estimated error due to uncertainties in input parameters, such as instrumental parameters or spectroscopic data, the $\boldsymbol{p} - \hat{\boldsymbol{p}}$ is only valid for fully correlated perturbations of $\boldsymbol{p}$ (assuming that $\boldsymbol{p}$ is a vector). In addition, the third term represents the error due to the measurements noise.

4.3 Characterization of H_2O and HDO/H_2O abundances

4.3.1 Aposteriori processing

The characteristics of the water vapour isotopologue remote sensing products is rather complex so that applying the aposteriori corrections for such kind of joint retrieval of isotopologues would be beneficial in terms of making sensitive to the same atmosphere air mass as well as minimizing the cross-dependence of the species. As a proxy state concept introduced by [3] allows for reasonably characterizing the retrieved

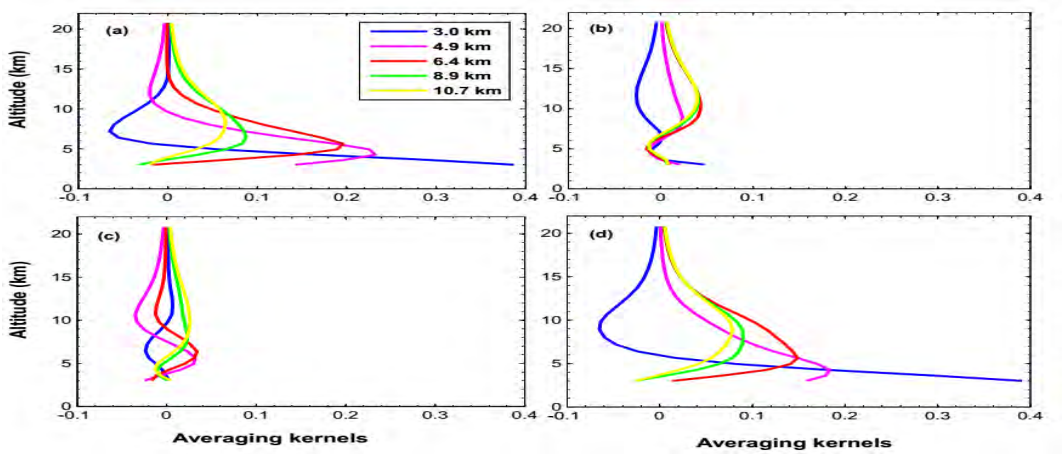

Figure 4.2: FTIR averaging kernels on the basis of $\ln[H_2O]$ and $\ln[HDO]$ (bottom panels) at the altitude levels of 3.0 (blue), 4.9 (magenta), 6.4 (red), 8.9 (green), and 10.7 (yellow) km (12 December, 2012, at 11:45 UTC), without applying aposteriori process.

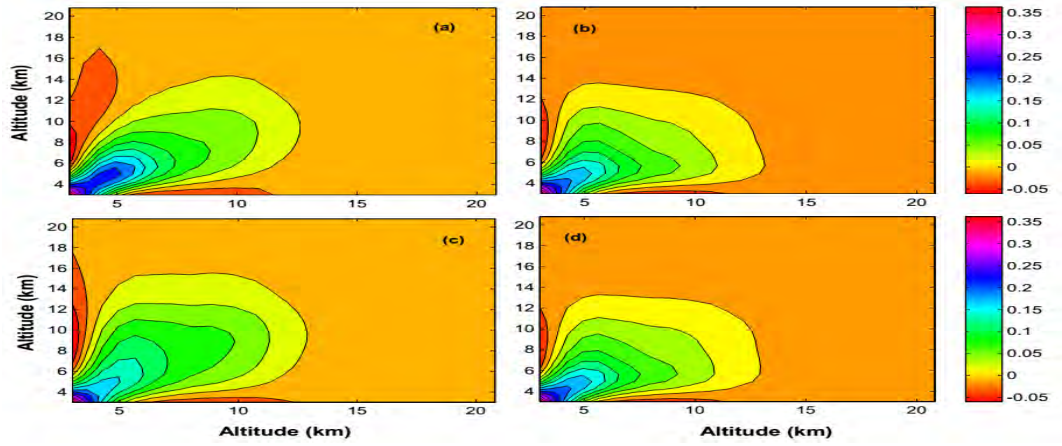

Figure 4.3: FTIR averaging kernels matrices for $\ln[H_2O]$ (top panels) and $\ln([HDO]/[H_2O])$ (bottom panels). Right and left panels are with and without applying aposteriori process, respectively, in a same date as given in Fig. 4.2.

Table 4.1 Assumed uncertainties used for error estimation.

Error source	Acronym	Uncertainty
Measurement noise	NOI	0.3%
Baseline (channeling and offset)	BAS	0.1% and 0.1^o
Mod. eff. and pha. err.	ILS	10% and 0.1 rad
Temperature profile	TEMP	1-5 K
Line of sight	LOS	0.01^o
Solar lines (Intensity and ν scale)	SOL	1% and 10^{-7}
Spectroscopic parameters	SPE	1-2%

products, namely humidity (or H_2O) and δD (or HDO/H_2O). From the first retrieved tropospheric {ln[H_2O], ln[HDO]}-state, the aposteriori corrected H_2O and δD values can be produced. The state {(ln[H_2O] + ln[HDO])/2} captures the large variations that are common to H_2O and HDO, then it is a good proxy for H_2O variations, and referred to as {H_2O}-proxy state. The state {ln[HDO] - ln[H_2O]} describes relatively small variations in the HDO/H_2O ratio, then it is a good proxy for δD variations, and referred to as δD-proxy state. Since the two isotopologues do not vary independently, there might be a better orthogonal basis for describing the tropospheric water vapour state. The rows of $\mathbf{P}$ describe this basis: the first n rows span the {(ln[H_2O] + ln[HDO])/2} and the second n rows the {ln[HDO] - ln[H_2O]}-state:

$$\mathbf{P} = \begin{pmatrix} -\frac{1}{2} \parallel & \frac{1}{2} \parallel \\ - \parallel & \parallel \end{pmatrix} \tag{4.3.1}$$

where $\parallel$ stands for an $n \times n$ identity matrix. The averaging kernel can be visualized by a transformation of $\mathbf{A}$ onto the basis described by the rows of matrix $\mathbf{P}$:

$$\mathbf{A}' = \mathbf{PAP}^{-1} = \begin{pmatrix} \mathbf{A}'_{HH} & \mathbf{A}'_{IH} \\ \mathbf{A}'_{HI} & \mathbf{A}'_{II} \end{pmatrix} \tag{4.3.2}$$

The adaptation of vertical resolution and sensitivity of the humidity profiles and the correction of cross-dependence, can be undertaken by aposteriori applying a matrix $\mathbf{C}$

to the retrieved variation of {ln[H_2O] + ln[HDO])/2, ln[H_2O] - ln[HDO]}-state vector:

$$\mathbf{C} = \begin{pmatrix} \mathbf{A}_{\|}^{'} & 0 \\ \mathbf{-A}_{HI}^{'} & \| \end{pmatrix} \tag{4.3.3}$$

The aposteriori corrected averaging kernel for the {ln[H_2O], δD}-proxy state is:

$$\mathbf{A}^{''} = \mathbf{C}\mathbf{A}^{'} \tag{4.3.4}$$

Apply the aposteriori corrections for originally retrieved {ln[H_2O], ln[HDO]}-state $\hat{\mathbf{x}}$ using the matrices $\mathbf{P}$ and $\mathbf{C}$ the correction operator. Then, the corrected {ln[H_2O], ln[HDO]}-state $\hat{\mathbf{x}'}$ is given as:

$$\hat{\mathbf{x}}^{'} = \mathbf{P}^{-1}\mathbf{C}\mathbf{P}(\hat{\mathbf{x}} - \hat{\mathbf{x}}_a) + \hat{\mathbf{x}}_a \tag{4.3.5}$$

Subsequently, we calculate H_2O and δD values from the corrected {ln[H_2O], ln[HDO]}-state $\hat{\mathbf{x}'}$. This aposteriori correction assures that the H_2O and δD products represent the same atmospheric air mass, which is important for the correct interpretation of δD signal from observations. Moreover, it guarantees that the cross-dependence of retrieved δD on atmospheric humidity variations is minimized. This cross-dependence might lead to an erroneous correlation between H_2O and δD. The details description about the aposteriori processing techniques can be obtained from [3].

4.3.2 Vertical resolution and sensitivity assessment

According to Rodgers optimal estimation (OEM) theory, the averaging kernel is the partial derivative of a retrieved state vector with respect to the true state vector. This averaging kernel provides the information about the retrieved state vectors, i.e., when its value is very small (close to 0), nearly all information about the retrieved

state vector derived from the apriori assumption of the state vector; when it is large (close to 1) then the information in the retrieval comes mainly from the measured spectra. In this study, the characterization of the retrievals of H_2O and HDO/H_2O ratio have been discussed thoroughly in terms of vertical resolution of the retrieval, its sensitivity to the apriori information and degree of freedoms for signal (DOFs). The spectral resolution of a measurement affects the amount of vertical information derived from the spectral line shape of a measured species [76].

Fig. 4.2 shows an example of FTIR averaging row kernels of the originally retrieved water vapour state for selected altitudes (3.0, 4.9, 6.4, 8.9, and 10.7 km) at 11:45 UTC taken 12 December, 2012. The row kernels reveal the atmospheric altitude regions that are represented by the retrieved states. All panels in the figure describe: The top left panel (a) shows the altitude regions of real atmospheric ln[H_2O] variations that affect retrieved ln[H_2O], the top right panel (b) shows the altitude regions of real atmospheric ln[HDO] variations that affect retrieved ln[H_2O], the bottom left panel (c) shows the altitude regions of real atmospheric ln[H_2O] variations that affect retrieved ln[HDO], the bottom right panel (d) shows the altitude regions of real atmospheric ln[HDO] variations that affect retrieved ln[HDO], respectively. As can be observed, both the retrieved ln[H_2O] and ln[HDO] amounts are affected by both variations of ln[H_2O] and ln[HDO]. The variability of the ln[HDO] is very small as compared to the variability of ln[H_2O]. It is observeed that the FTIR resolves the vertical structures of H_2O profile much finer than the respective isotopologues ratio structures. The vertical resolution, defined as full width at half maximum (FWHM) of the averaging kernels, of H_2O profiles are about 2.5 and 6 km for the lower and middle troposphere, respectively while the vertical resolution of the δD profiles are

Table 4.2 Statistical and systematic errors in H_2O total column due to the assumed uncertainty sources listed in Table 1.

Error source (Acronym)	Statistical (in %)	Systematic (in %)
NOI	0.20	-
BAS	0.20	0.20
ILS	< 0.04	< 0.04
TEMP	0.60	0.20
LOS	< 0.10	< 0.01
SOL	< 0.10	< 0.01
SPE	-	0.70
Total	0.68	0.76

about 2.5 km in the lower troposphere and 7 km in the middle troposphere. Typical degrees of freedoms (DOFs) are 2.4 for H_2O and 1.7 for δD profiles. The sensitivity (sum along the row of the averaging kernels matrix) provides the vertical information to what extent the retrieved mixing ratio profiles derived from the measured spectra. For H_2O profile, the sensitivity is larger than 67% for altitudes below about 10.7 km; regarding δD profiles the sensitivity is about 60% for altitudes below 7.2 km. Thus, the retrieved H_2O and δD values are not the representative of the same airmass. Therefore, it has been performed the aposteriori correction for the originally retrieved ln[H_2O] and ln[HDO] states based on the aposteriori processing techniques as suggested by [3]. Smoothing the vertical resolution and sensitivity of the H_2O profiles to the poorer vertical resolution and sensitivity of the δD profiles for making better scientific interpretation. Fig. 4.3 shows the averaging kernels matrices plot; the left top and bottom panels demonstrate the sensitivities of H_2O and δD profiles without applying the aposteriori processing, respectively, similarly the right panels display sensitivities but applying the aposteriori processing.

Table 4.3 Statistical and systematic errors in H_2O and δD total columns after applying the aposteriori processes. Stat. represents Statistical and Syst. refers Systematic

Error source (Acronym)	H_2O Stat. (in %)	H_2O Syst. (in %)	δD Stat. (‰)	δD Syst. (‰)
NOI	0.20	-	0.50	-
BAS	0.20	0.20	0.90	0.90
ILS	0.02	0.02	0.10	0.10
TEMP	0.30	0.10	3.00	1.30
LOS	< 0.10	< 0.06	0.10	0.10
SOL	0.002	0.01	0.01	0.01
SPE	-	0.50	-	4.00
Total	0.43	0.55	3.20	4.30

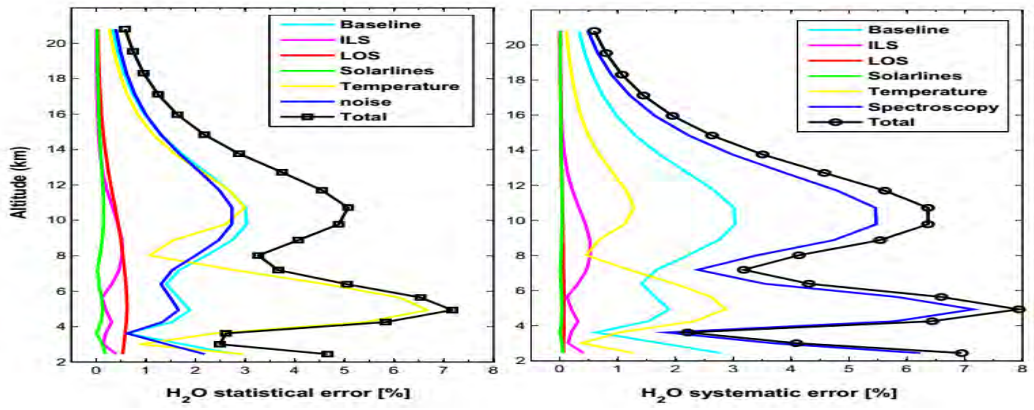

Figure 4.4: Error budget of H_2O retrieval from FTIR solar spectra (11:45 UTC 12 December, 2012). Left: Estimated uncertainty profiles for statistical error. Right: Systematic error contributions. The acronyms in the legend are depicted in Table 4.1

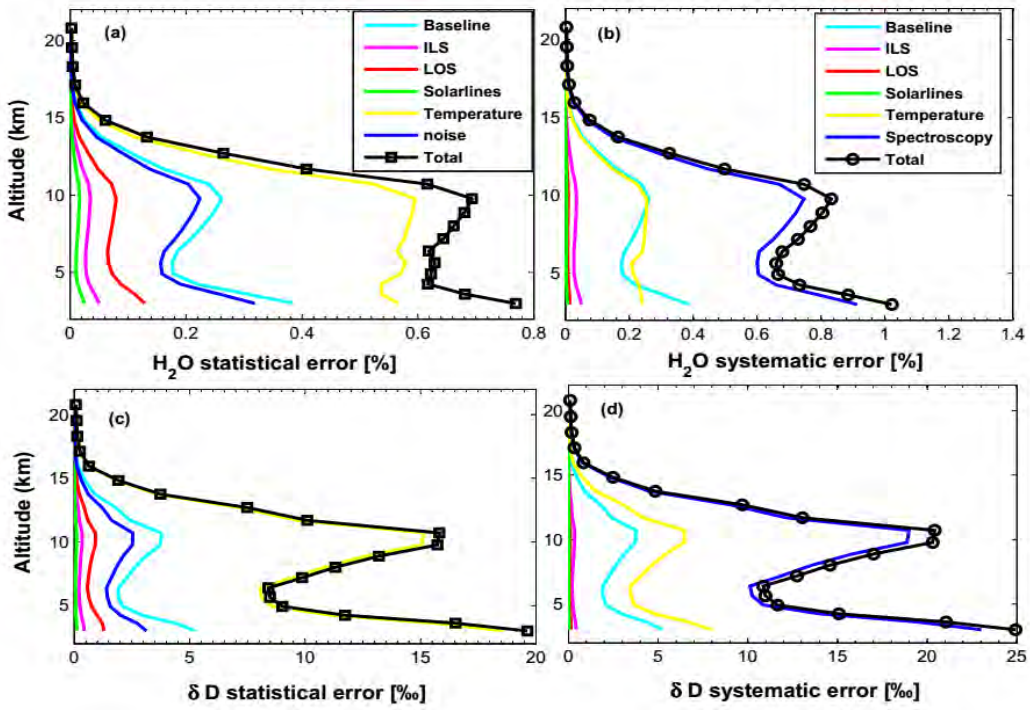

Figure 4.5: Error budget of H_2O (top panels) and δD (expressed as ln([HDO]/[H_2O])) (bottom panels) retrievals after applying aposteriori process (11:45 UTC 12 December, 2012). Left: Estimated uncertainty profiles for statistical error. Right: Systematic error contributions.

4.3.3 Error analysis

It has been used the absorption signatures of H_2O and HDO in the mid-infrared region (2400 - 3200 cm^{-1}) in order to determine their VMR profiles and column amounts in the atmosphere. Fig. 4.1 shows an example of measured spectra (black line) and the corresponding simulated spectra (red), as well as the residual spectra (green) in each microwindows for one of the measurements taken on 12 December, 2012. The microwindows have strong, but mostly not saturated, and well-isolated H_2O and HDO absorption lines. The spectral microwindows that are considered in this study are derived from ALFIP (Automatic Line FInding Program) software [118] and from the reported paper [119]. The major absorption lines of interfering gases in these spectral microwindows are O_3, N_2O, CH_4, and HCl. There are also minor interfering absorbers are $H_2^{18}O$, and CO_2. In addition to H_2O and HDO, the simultaneous retrieval of O_3, N_2O, CH_4, and HCl profiles are made in order to minimize the interference errors [120]. For the retrieval of H_2O and HDO, the spectroscopic line parameters are taken from the High Resolution Transmission data (HITRAN) 2008 [121], with 2009 updates for the line-by-line simulations of the spectral signatures.

In this section, it has been estimated the errors of the H_2O and δD profiles based on the assumed uncertainty sources as listed in the Table 4.1. This error analysis is vital for the overview of the achievable data quality. Fig. 4.4 depicts H_2O profile error estimates for different source of errors. Fig. 4.4 shows the statistical error (left panel) and systematic error (right panel) profiles for a typical H_2O retrieval. The quantified sources of errors are temperature, measurement noise, instrumental line shape, solar lines, line of sight, zero baselines offset, and spectroscopy. It has been observed that baseline and atmospheric temperature uncertainties are the leading

random error sources, whereas the uncertainty of spectroscopic parameters are the main systematic error source. The total statistical error is found to be 2.5 - 7.3% in the troposphere while the total systematic error is less than 8%. Fig. 4.5 illustrates the estimated errors (upper panels for H_2O, lower panels for δD) after applying a posteriori treatment. Measurement noise as well as uncertainties in the tropospheric temperature structure and the baseline dominate the random error of H_2O and δD. The systematic errors are clearly controlled by uncertainties in the spectroscopic line parameters, which can give rise to a δD error of 100-200 ‰. Uncertainties in water vapour spectroscopy remain an important problem [122]. Errors in line intensity and half widths reveal mainly in systematic shifts of the retrieved data while errors in the coefficient of temperature dependence of air-broadened half width effects the retrieval differently depending on atmospheric temperature. According to indices of uncertainty in HITRAN 2008 [121], uncertainties in the intensity of water vapour spectral lines ranges from 5 to 10% (that is about 50-100 ‰ in terms of δ-values) while uncertainty in air broadening coefficients typically ranges between 2 and 5%. Uncertainty in the coefficient of temperature dependence of air-broadened half-width ranges between 10% and 20% and may introduce a bias that depends on atmospheric temperature. This error can lead to tangible under- or overestimation of concentration of the species of interest depending on the atmospheric conditions (dry or wet conditions).

Chapter 5

Intercomparison of δD and H_2O amounts from various instruments

5.1 Methodology for intercomparison of VMR profiles

The closest satellite measurements (on the same day as the ground-based FTIR measurements, from June, 2009 to March, 2013) within ±2 degrees of latitude and ±5 degrees of longitude are selected for intercomparison. The more stringent latitudinal criterion has proven to be a good choice for all comparisons, since latitudinal variations are in general more pronounced than longitudinal ones. These criteria yielded 26, 13, and 18 days of coincident H_2O measurements between FTIR with AIRS, TES level 2, and TES level 3, respectively. The satellite data (AIRS and TES) used in the following comparisons have considerably better vertical resolution than ground-based FTIR profiles due to observation geometry, spectral windows, and measurement

techniques. The vertical resolution of satellite measurements of profiles are therefore degraded to facilitate a comparison between the two sets of profiles, that is, the satellite measurement profiles are smoothed using the averaging kernels calculated during the ground-based FTIR retrieval process as proposed by [108]. Using the approach presented in [3], the smoothed profiles of water mixing ratios ($\hat{\boldsymbol{x}}_s$) from the model or satellites are obtained as:

$$\hat{\boldsymbol{x}}_s = \exp[\ln(\boldsymbol{x}_a) + \hat{\mathbf{A}}''_{HH}(\ln(\boldsymbol{x}_s) - \ln(\boldsymbol{x}_a)] \tag{5.1.1}$$

where $\boldsymbol{x}_s$ represents the original (unsmoothed profiles) model output or satellite measurement profile, $\hat{\boldsymbol{x}}_s$ is the smoothed profile, and $\boldsymbol{x}_a$ and $\hat{\mathbf{A}}''_{HH}$ are the apriori profile and the aposteriori processing applied averaging kernel matrix for H_2O VMR profile derived from ground-based FTIR instrument, respectively. In a similar way, the smoothed profiles of δD (expressed as $\boldsymbol{R}_s$ = HDO/H_2O) with respect to lower resolution data can be expressed as:

$$\boldsymbol{R}_s = \exp[\ln(\boldsymbol{R}_a) + \hat{\mathbf{A}}''_{DD}(\ln(\boldsymbol{R}_s) - ln(\boldsymbol{R}_a))] \tag{5.1.2}$$

where $\boldsymbol{R}_s$ is the smoothed δD profile, and $\boldsymbol{R}_a$ and $\hat{\mathbf{A}}''_{DD}$ are the apriori profile and the aposteriori processing applied averaging kernel matrix for δD profile from FTIR, respectively. Absolute differences for each profiles and the mean value as function of altitude is calculated as:

$$\triangle_{\text{abs}}(z) = \frac{1}{N(z)} \sum_{i=1}^{N(z)} [\text{FTIR}_i(z) - \text{s}_i(z)] \tag{5.1.3}$$

and the standard deviation of the differences $\sigma_{diff}(z)$ is computed as:

$$\sigma_{diff}(z) = \sqrt{\frac{1}{N(z)} \sum_{i=1}^{N(z)} [\text{FTIR}_i(z) - \text{s}_i(z) - \triangle_{\text{abs}}(z)]^2} \tag{5.1.4}$$

where $N(z)$ is the number of coincidences at z, $\mathrm{FTIR}_i(z)$ is the FTIR VMR at z and the corresponding $\mathrm{s}_i(z)$ VMR for the validation instrument or model output. Note that the term absolute, as used in this work, refers to differences between the compared values, in VMR as opposed to percentage or relative differences, in other words: absolute differences can be negative. To calculate the profile of the mean relative difference, as a percentage, is expressed as:

$$\triangle_{\mathrm{rel}}(z) = 100(\%) \times \frac{1}{N(z)} \sum_{i=1}^{N(z)} \frac{[\mathrm{FTIR}_i(z) - \mathrm{s}_i(z)]}{[\mathrm{FTIR}_i(z) + \mathrm{s}_i(z)]/2} \tag{5.1.5}$$

In some cases, there seems to be a discrepancy between the apparent differences given by the sign of the mean absolute and mean relative differences. This arises due to the fact that the mean relative differences are not calculated from the mean VMR profiles but from each pair of coincident profiles (Eq. 5.1.5). Thus, the mean relative differences can become negative, even though the mean absolute differences are positive. A comparison of the integrated column amounts between FTIR and its correlative measurements/simulated output has been done by employing the FTIR averaging kernels for smoothing. Once the profiles are convolved with FTIR averaging kernels, then the integrated column amounts (IC) for those instruments and model with respect to the FTIR pressure levels are calculated using trapezoidal integral method which is given as:

$$IC = \frac{1}{\rho_v g} \int_{P_T}^{P_\circ} q dp \tag{5.1.6}$$

where $P_\circ$ is pressure at the lower level, P_T is pressure at the upper level of the troposphere, ρ_v is the density of the atmospheric vapour, g is a gravity of the Earth surface, and q denotes volume mixing ratio (VMR). The limit of the integration is chosen based on the vertical sensitivity of the measurement derived from instrument. The relative differences of the integrated column amounts between FTIR and its

correlative measurements from AIRS, TES level 2, TES level 3 instruments, and IMK MESSy simulated output for coinciding dates can be expressed as:

$$\text{Rel. diff.}(\%) = \left(\frac{[\text{FTIR}_i(IC) - \text{s}_i(IC)]}{[\text{FTIR}_i(IC) + \text{s}_i(IC)]/2}\right) \times 100 \tag{5.1.7}$$

where IC represents integrated column amount and $\text{s}_i(IC)$ refers to correlative satellite measurement or model output.

5.2 Intercomparison of H_2O VMR profiles

Fig. 5.1 (left top panel) shows an example of a comparison of H_2O VMR profiles between ground-based FTIR and IMK MESSy model output on 18 December, 2010. Fig. 5.1 (left bottom panel) depicts the absolute difference between FTIR and smoothed IMK MESSy profiles of H_2O. Below 3.6 km, FTIR H_2O VMR exceeds slightly MESSy H_2O VMR. Moreover, the statistical relationship for VMR profiles comparisons between the FTIR and MESSy (the smoothed profiles) is made during the measurement period that has been taken by FTIR from 2009 to 2013. By applying the temporal coincidence of ± 1 hours, 103 days of coincident measurements (a total of 336 data points) are obtained. All FTIR data points within the 1 hour interval are considered for comparison. Fig. 5.2 (left top and bottom panels) shows the statistical relationship for all 103 coincidences for H_2O VMR. The left-top panel shows the mean absolute differences (g/kg) and the left-bottom panel is the mean relative differences (%). Error bars represent the standard deviation. The mean relative differences are within -20.6 to 7.8% with the corresponding standard deviation from 23.6 to 40.2% in the altitude range between 2.4 and 8.9 km. The temporal differences might be the possible reasons for the discrepancy between them, since H_2O amounts

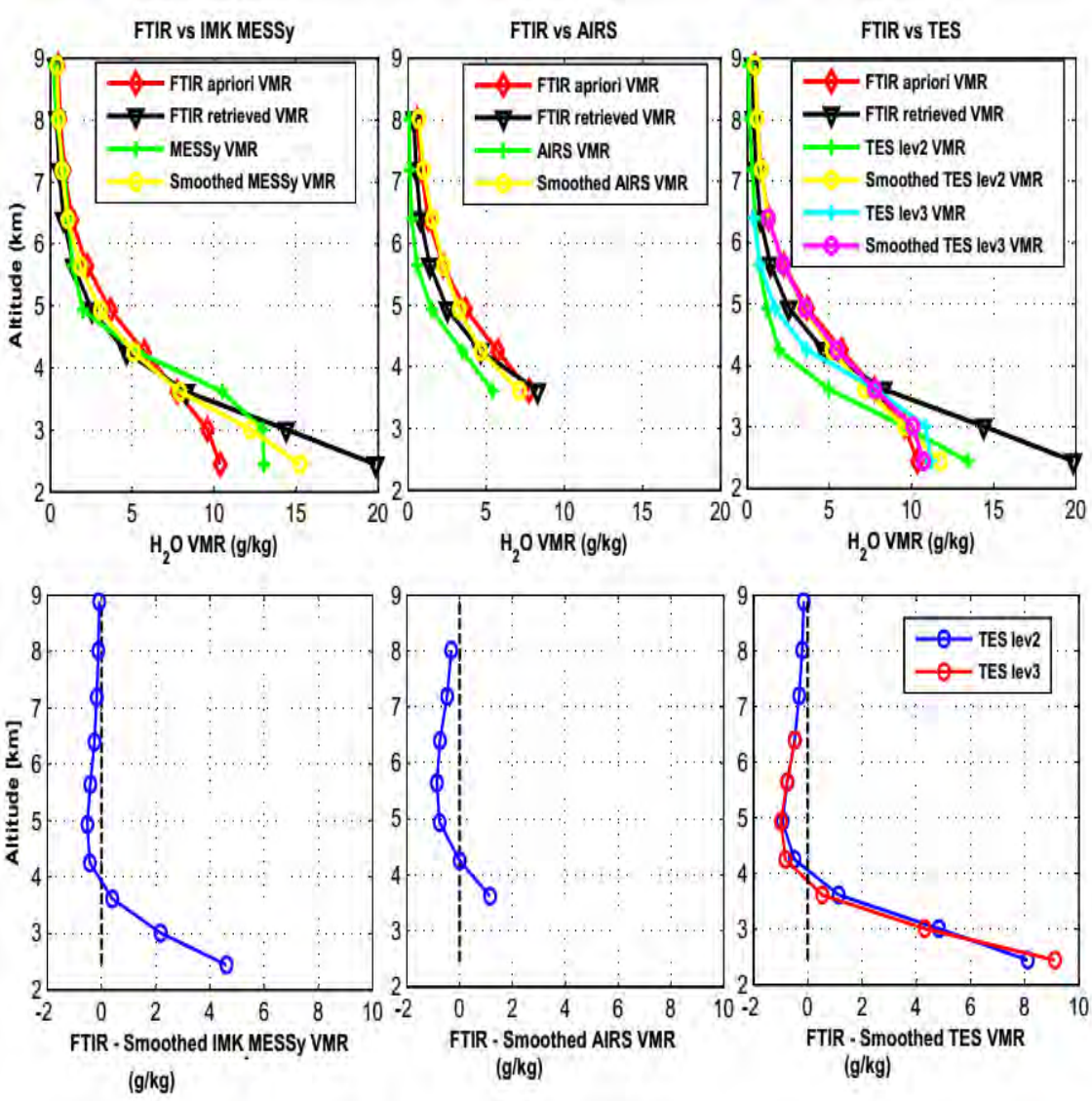

Figure 5.1: Top: Comparisons of H_2O VMR profiles on 18 December, 2010. FTIR apriori (red with diamond symbol) and FTIR daily mean (black with triangle symbol) are shown in top panels, MESSy smoothed (yellow with circle) and MESSy (green with plus sign symbol) (left top panel), TES smoothed (yellow with circle) and TES (green with plus sign symbol) (middle top panel), and AIRS smoothed (yellow with circle) and AIRS (green with plus sign symbol) (right top panel). Bottom: Absolute differences (in g/kg) between FTIR and smoothed MESSy (left bottom panel), FTIR and smoothed TES (middle bottom panel) and FTIR and smoothed AIRS (right bottom panel).

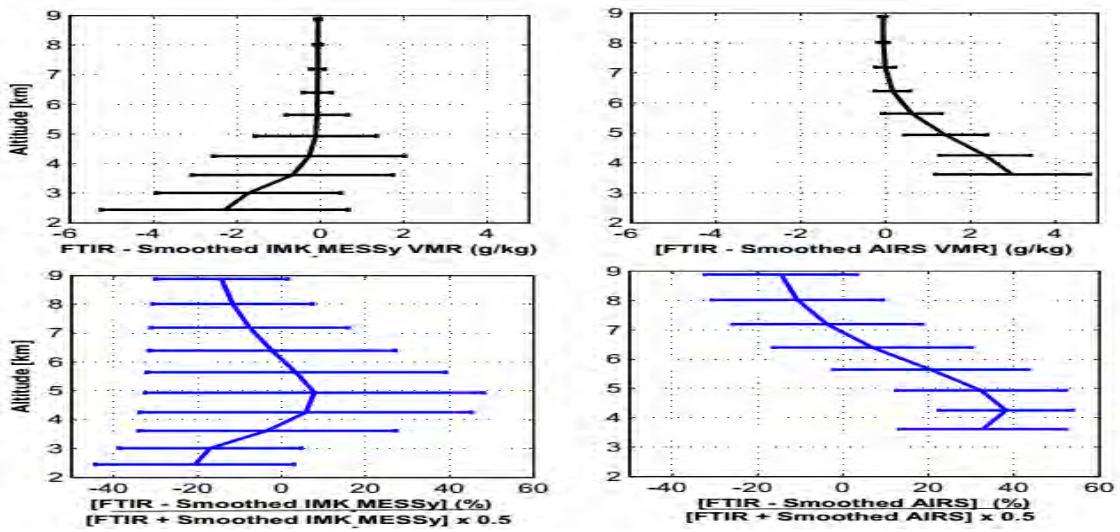

Figure 5.2: Statistics for intercomparison of H_2O VMR profiles between FTIR and MESSy and AIRS. Top: Mean of the differences and its standard deviation (shown as error bar) for FTIR-MESSy (left) and FTIR-AIRS (right). Bottom: the same as top panels but for relative differences.

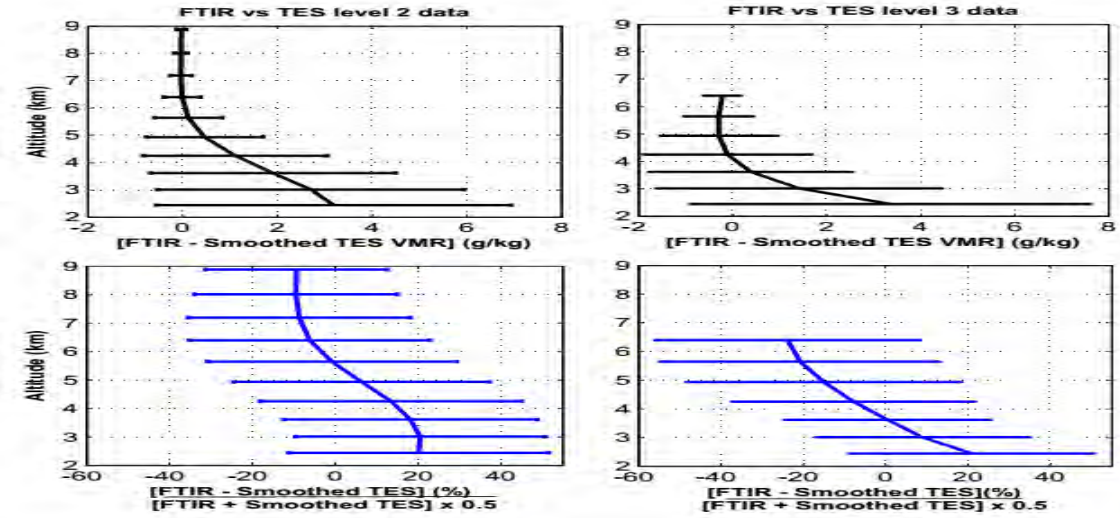

Figure 5.3: Similar to Fig. 5.2 but for intercomparison of FTIR with TES-level 2 (left panels) and TES-level 3 (right panels).

vary quite rapidly. The temporal extent of the FTIR measurements is in the order of minutes so that the measurements are well able to detect instantaneous small scale features. On the contrary, the models temporal output step is 1 hour. It represents atmospheric features averaged over 1 hour. This disparity will cause the FTIR data to be more variable on short time scales than the model data.

The comparison of H_2O profiles derived from the FTIR and AIRS in the altitude between 3.6 and 8.9 km have been analyzed. Middle panels of Fig. 5.1 show that the comparison of H_2O profiles from ground-based FTIR with AIRS on 18 December, 2010. Fig. 5.1 (middle bottom panel) depicts the absolute difference between FTIR and smoothed AIRS profiles of H_2O. On this day, FTIR H_2O VMRs are slightly larger than AIRS measurements over the entire altitude region. The magnitude of the largest absolute difference is about 2.9 g/kg, with the corresponding relative difference of 32.7%, at 3.6 km. In addition, it is drawn up the statistical relationship for 26 coincident measurements of the two instruments, as shown in Fig. 5.2. The mean relative differences are within 6.8% to 32.7% in the altitude range between 3.6 to 8.9 km.

The comparison of H_2O VMR profiles between FTIR and TES including both level 2 version 05 and level 3 version 02 is also performed. Based on selecting the coincident days with ± 2 degrees of latitude and ± 5 degrees of longitude, 13 and 18 numbers of coincident days for TES level 2 and level 3, respectively are resulted. Similar to the above sections a single day profile comparisons is examined, taken on 18 December, 2010. Right panels of Fig. 5.1 show the comparison of H_2O profiles from ground-based FTIR to TES (yellow represents for smoothed level 2 and cyan for smoothed level 3 data) on 18 December, 2010. Below 4 km, our FTIR instrument estimates larger

than TES measurements in both cases. Fig. 5.3 depicts the statistical relationship for the coincident H_2O VMR profiles between FTIR and TES (both level 2 and level 3) observations. The left-panels demonstrate differences between FTIR and TES level 2, whereas the right-panels depict for FTIR and TES level 3. An overview of the results suggests that there is no significant difference between FTIR and both TES level 2 and level 3. The mean relative differences are generally found to be -20 to 20% in the altitude range between 2.4 to 6.4 km.

Intercomparisons depicted in Figs. 5.1-5.3 show differences on the level of agreement between correlative measurements as a function of altitude. At lower levels, FTIR values tend to exceed both AIRS and TES instruments, while above 5 km, FTIR values tend to less than these instruments. Temporal and spatial differences, as well as differences in the instrument measurement techniques could be the possible reasons for the discrepancy between them. At the lowest level, higher FTIR H_2O amounts are noticed as compared to the other instruments, this might be explained by the topographic and surface influences on its measured values that would be expected to be high. For instance, temperature on the lowest levels at the measured site is assumed to be higher than in the free troposphere, which probably will lead to higher H_2O amounts. Moreover, tropical region of the troposphere is well characterized by strong dynamics, it is obvious that this would be a significant factor for the differences in the measurements. Apart from that, the discrepancy of the result could be partly explained by known contributions to the systematic error budget of the comparison. The other possible reason is that the average values are calculated on the basis of log retrievals, this might be causing bias for H_2O species because of large vertical gradients. The extent of such impact on water vapour has been reported in [123].

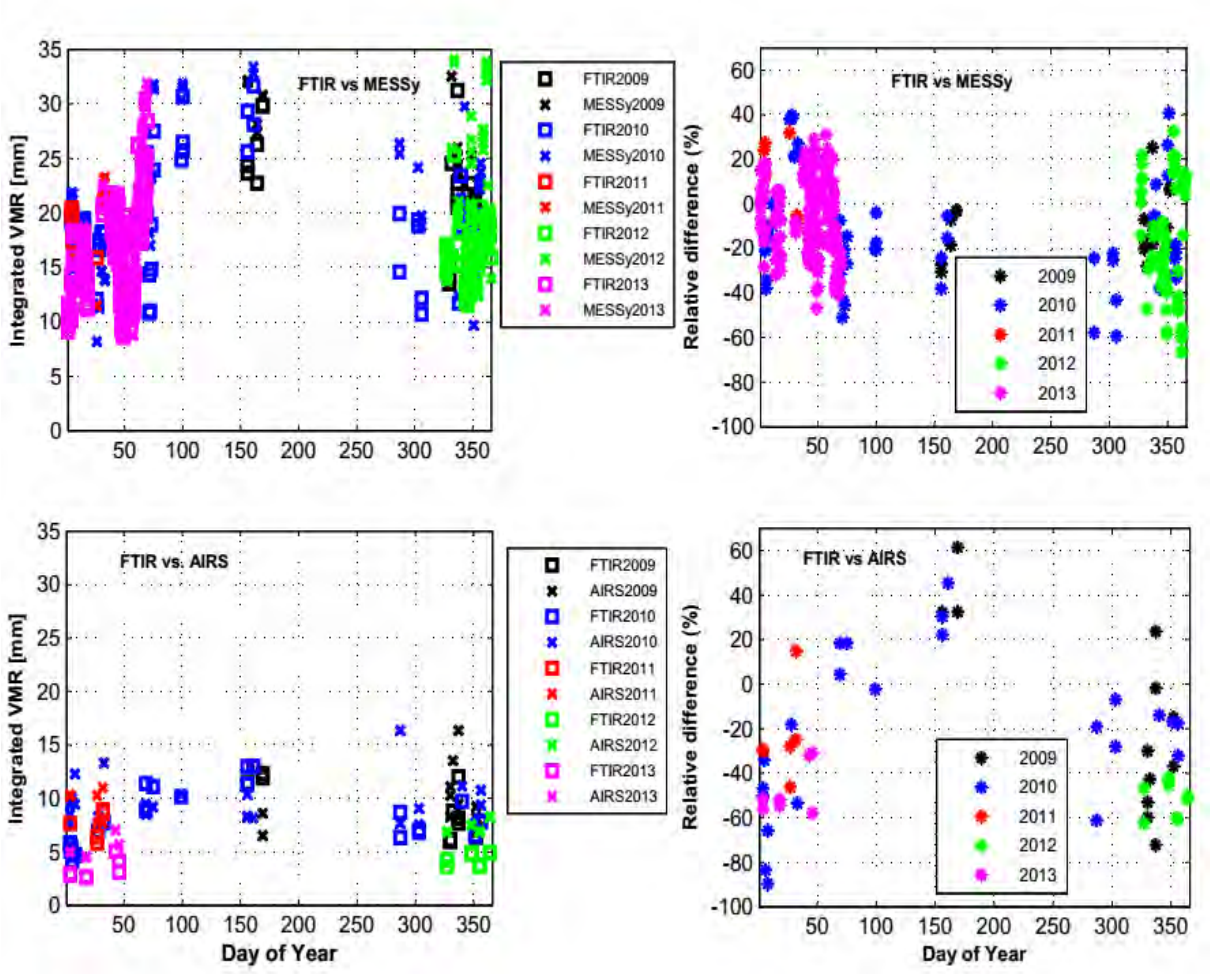

Figure 5.4: Top-left panel shows integrated column amounts of H_2O for FTIR (open square) and the corresponding MESSy simulated output (cross) for different observations years (in color), and bottom-left panel shows integrated column amounts between FTIR (open square) and AIRS (cross). Right panels depict the relative differences between FTIR and MESSy (right top panel), and FTIR and AIRS (right bottom panel).

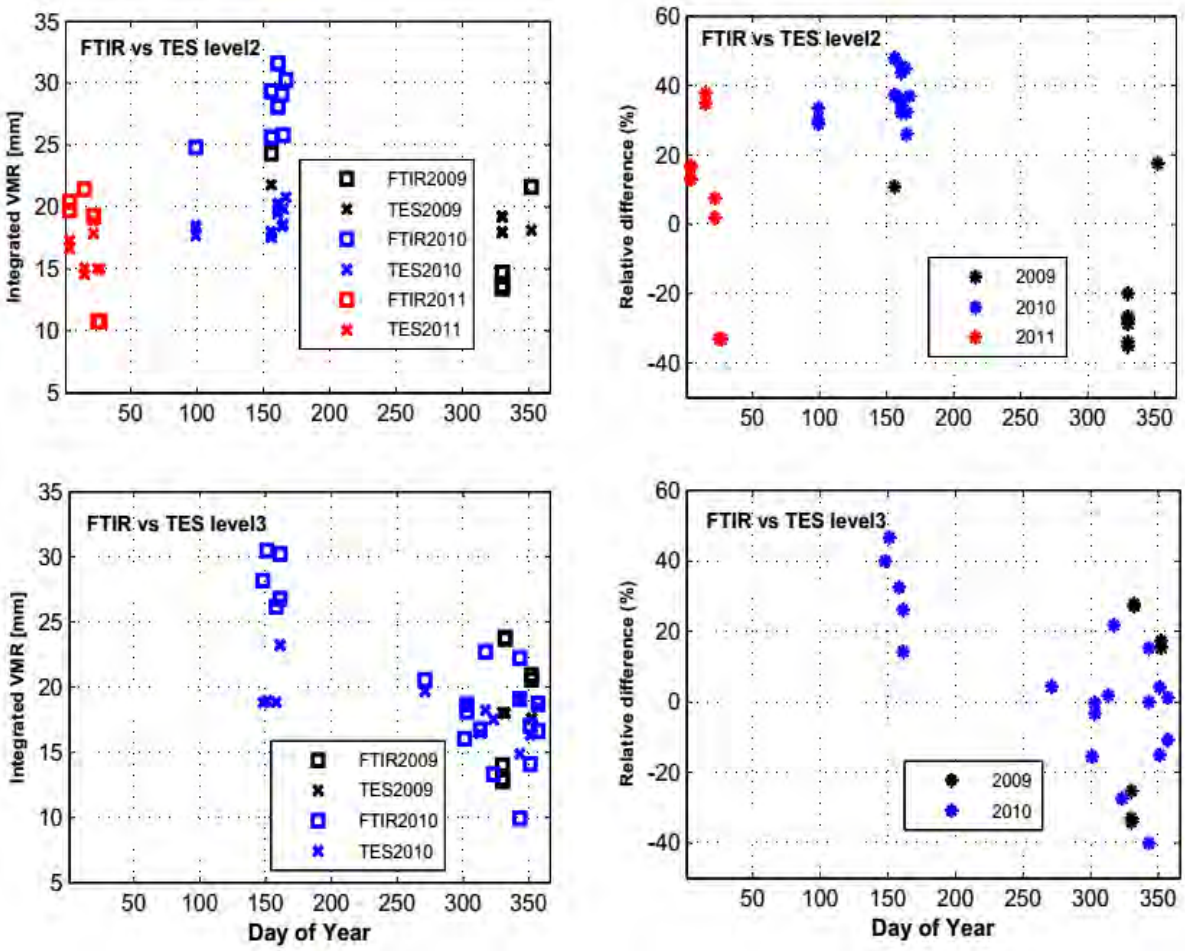

Figure 5.5: Similar to Fig. 5.4 but for intercomparison of FTIR with TES-level 2 and TES-level 3 as shown in the figure legend.

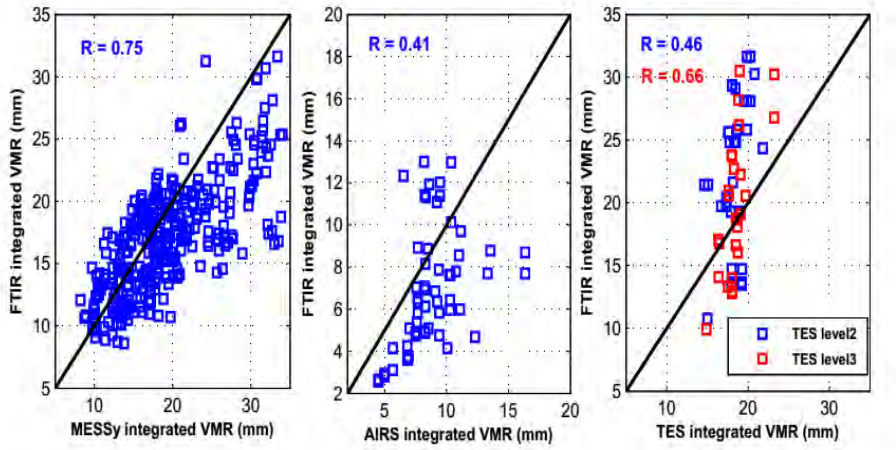

Figure 5.6: Scatter plot of integrated column amounts of H_2O measured by ground-based FTIR versus those observed by MESSy, AIRS, and TES (level 2 and level 3). The correlation coefficient (R) for the comparisons is shown in all panels. The black solid line shows the one-to-one line of 100% correlation.

Table 5.1. Summary of the comparison between H_2O columns amount derived from FTIR and MESSy, AIRS, TES (level 2 and level 3) over Addis Ababa. R is correlation coefficient, N represents number of coincident days, T is total number of data points.

Comparison of FTIR with	R	N	T	Mean Relative Difference (%)
MESSy	0.75	103	336	-9.4±21.7
AIRS	0.41	26	58	-28.6±33.6
TES level 2	0.46	13	35	15.4±27.6
TES level 3	0.66	18	18	3.5±23.7

5.3 Intercomparison of H_2O column amounts

The left top panel in Fig. 5.4 depicts the comparisons of the time series of H_2O integrated column amounts of FTIR measurements and MESSy while in the right top panel, the relative difference between them is displayed. As evident from Table. 5.1, a mean relative difference of -9.4 ± 21.7% is statistically significant. In general, FTIR column amounts are about 9.4% less than MESSy values. The linear relationship between them is also examined in terms of correlation coefficient. The correlation coefficient of integrated column amounts between FTIR and MESSy is 0.75 (see left panel of Fig. 5.6), which suggests better relationship between them. For further investigation, a cross-comparison of H_2O abundance of MESSy and ECMWF ERA-interim reanalysis data is also performed (see Fig. 5.8).

Fig. 5.4 (left bottom panel) demonstrates the comparison of H_2O column amounts of FTIR and AIRS. The 26 coincident days are obtained based on the coincidence criteria as stated in the earlier section. The right bottom panel of Fig. 5.4 illustrates the relative differences between FTIR and smoothed AIRS integrated column amounts. The relative differences between the FTIR and AIRS column amounts are generally within the range of -90 to +60%. In fact, about ninety two percent of the differences are in the range of -65% to +30%. This suggests that the absolute difference of the column amount is bounded within ±6.0 mm. In general, the mean relative difference is found to be (-28.6 ± 33.6)% (see Table 5.1). Fig. 5.6, middle panel, displays the correlation between FTIR and AIRS column amounts of H_2O for the given coincident data as characterized by the correlation coefficient of 0.41.

FTIR H_2O integrated column amounts are also compared to TES measurements.

Fig. 5.5 shows the comparisons of the time series of H_2O integrated column amounts and the collocated TES level 2 (left top panel) and TES level 3 (left bottom panel) measurements while right panels display the relative differences between them. The mean relative difference, on 13 coincidences, between FTIR and TES level 2 is (-15.4 $\pm$ 27.6)%, whereas the mean relative difference of FTIR with that of TES level 3 is (3.5 $\pm$ 23.7) on the given 18 coincidences. This would suggest that they are in good level of agreement. Furthermore, the correlation coefficients are obtained 0.46 for FTIR versus TES level 2 and 0.66 for FTIR versus TES level 3. The FTIR measures systematically higher H_2O integrated columns than the TES instrument since large contribution for integrated H_2O amount is coming from lower level troposphere, close to the surface. In other studies, for e.g. in [119], it has been reported a good agreement in the comparison between FTIR H_2O VMR profiles and Vaisala RS92 radiosonde measurements and is found to be the relative difference generally within 20% in the troposphere, which is also comparable to the differences found in the comparison of H_2O VMR profiles of FTIR with TES.

Some of the differences between the FTIR and satellite observations could have arisen from a strong gradient in H_2O spatial and temporal variations, even though there is no large difference in space and time for the criteria used to determine coincident measurements. Apart from that, different spectroscopic windows used by FTIR and other instruments used for the comparisons might have also some contribution to the observed differences.

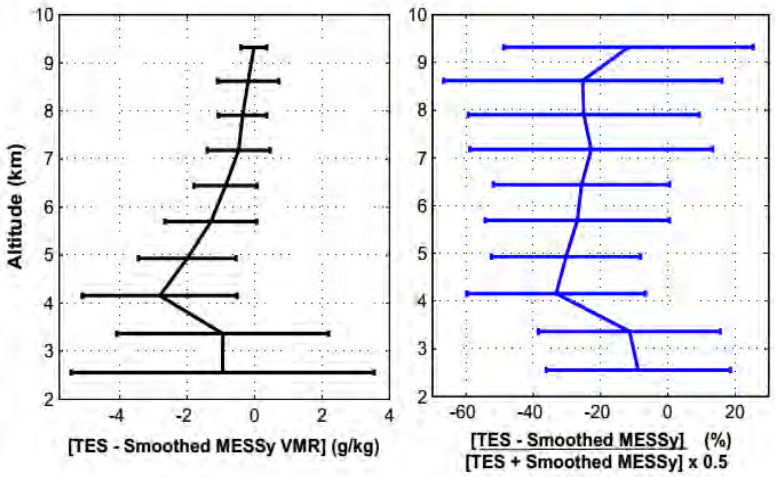

Figure 5.7: Similar to Fig. 5.2 but for differences between TES and MESSy.

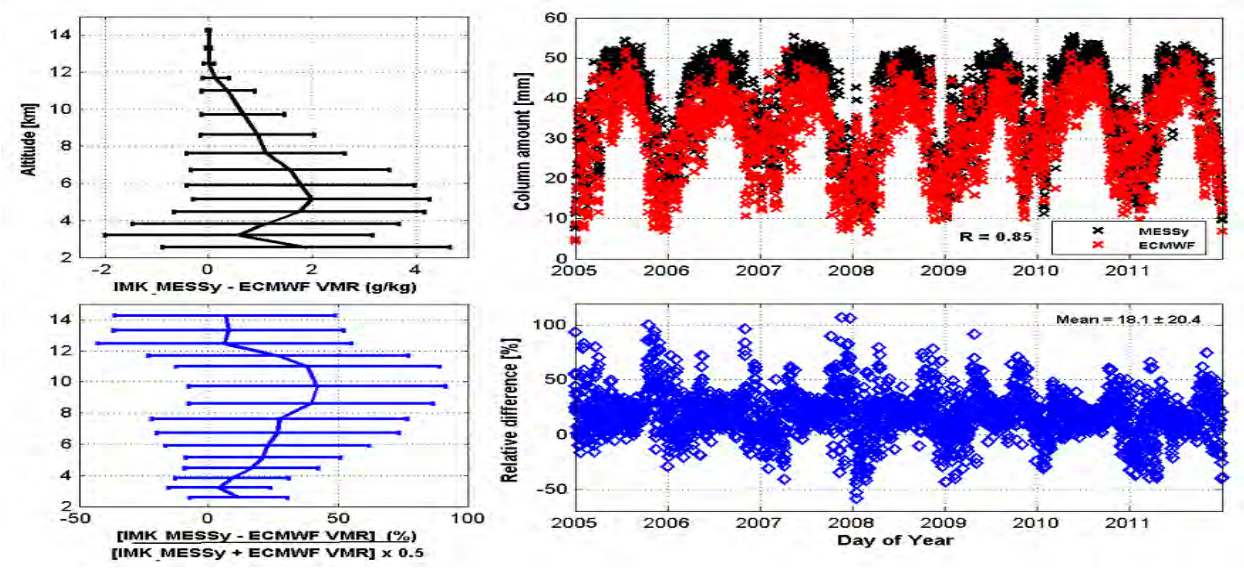

Figure 5.8: Left panels: Similar to Fig. 5.2 but for differences between MESSy and ECMWF. Right panels: The time series of integrated column amounts of H_2O (top panel) and relative differences (bottom panel) during 2005-2011.

5.4 Comparison of H_2O amounts from MESSy to TES and ECMWF

This section discusses the intercomparison of H_2O VMR profiles from MESSy to TES and ECMWF. Based on coincidence criteria, a total 145 number of days is yielded between MESSy and TES during a period between 2007 to 2011. The H_2O VMR profiles obtained from MESSy are smoothed by TES averaging kernels. Fig. 5.7 shows the statistical relationship for all 145 coincidences for H_2O VMR profiles between TES and MESSy, irrespective of season. The overall result reveals no significant difference between them. The comparison result shows that MESSy VMRs are slightly larger than TES measurements over the entire altitude range. The mean relative differences lie between -33.2 to -8.8% in the altitude range of 2.6 and 9.3 km where the mean absolute differences are within -2.8 g/kg and -1.0 g/kg with the corresponding standard deviation from 2.3 to 4.5 g/kg. The largest absolute difference is about -2.8 g/kg and the corresponding relative discrepancy is about -33.2% at the altitude of 4.2 km.

Fig. 5.8 illustrates the comparison between MESSy and ECMWF. Right panels: The time series of integrated column amounts of H_2O (top panel) and relative differences (bottom panel) during 2005-2011, whereas left panel shows the statistical relationship for all H_2O VMR profiles. In general, MESSy estimates more than ECMWF as can be seen the overall patterns of VMR differences as well as the time series of the integrated column amounts. In addition, the result suggests that the maximum relative difference of integrated column amounts is exhibited during winter season which is a dry season so that the amount of water vapour is minimum. The correlation

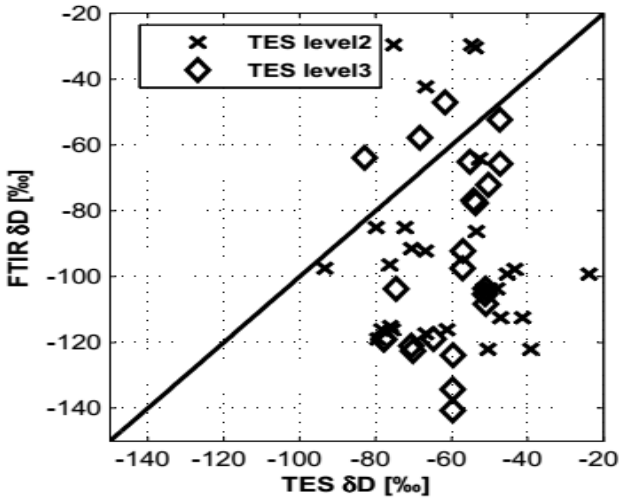

Figure 5.9: Scatter plot δD measured by ground-based FTIR versus those observed by TES-level 2 and TES-level 3 datasets. The black solid line shows the one-to-one line of 100% correlation.

coefficients of integrated column amounts between MESSy and ECMWF is 0.85, which suggests better relationship between the them.

5.5 Comparison of δD amounts from FTIR to TES

As for H_2O VMR intercomparison, to compare δD amounts as derived from FTIR to TES, we have taken into account spatio-temporal sampling and instrument sensitivity through collocation and convolution with FTIR averaging kernels. Here, the comparison of δD amounts between them is made at a single altitude level which is 3.6 km where the HDO sensitivity is found to be maximum. Fig. 5.9 demonstrates the scatter plot of δD measured by ground-based FTIR versus those observed by TES-level 2 (x symbol) and TES-level 3 (diamond symbol). The result generally shows

that the FTIR δD values is relatively depleted as compared to the corresponding TES observations. The absolute mean difference is about -38.6‰ which can be explained by the combined instruments precision which is about -35‰.

Chapter 6

Tropospheric H_2O, δD, and $\delta^{18}O$ budget in cycle

6.1 Spatio-temporal variations of isotope composition of water vapour

The overall continental and global patterns in isotopic composition of water are fairly well described by condensation temperature and Rayleigh fractionation during rain-out. However, these processes do not fully explain the isotopic variability in the tropics. To evaluate the spatial (the region confined in 3°N-15°N latitude and 33°E-48°E longitude) and seasonal patterns of water vapour isotopic composition as derived from TES satellite dataset measuring tropospheric water vapour and its δD, some meteorological variables are explored to explain the variability observed in it. The isotopic composition of water undergoes seasonal fluctuations imposed by seasonality of climatic parameters such as temperature, relative humidity (RH), moisture

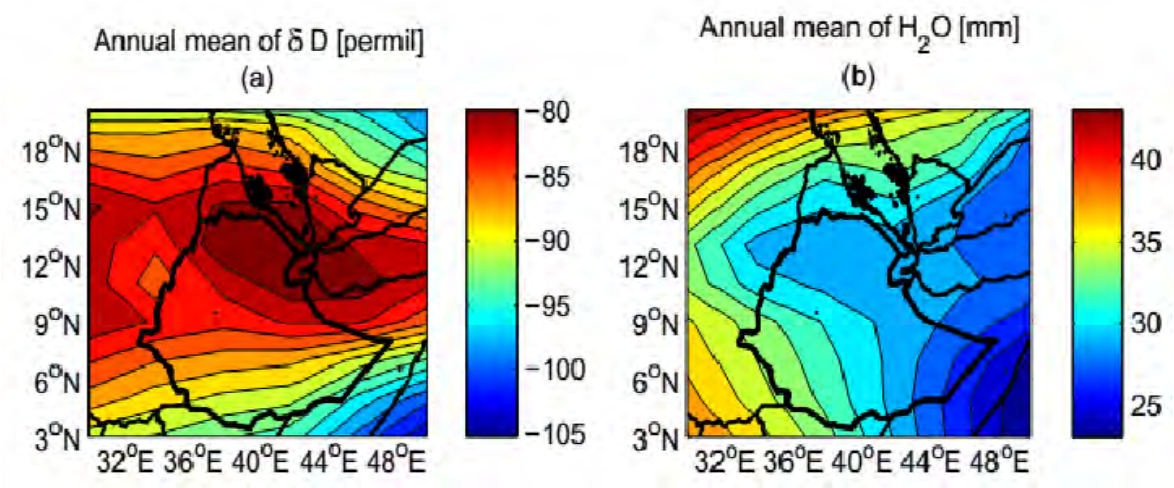

Figure 6.1: Spatial patterns of annual mean of integrated δD (‰) (a) in vapour and H_2O (mm) (b) over Ethiopia, based on TES observations during a period of 2005-2010.

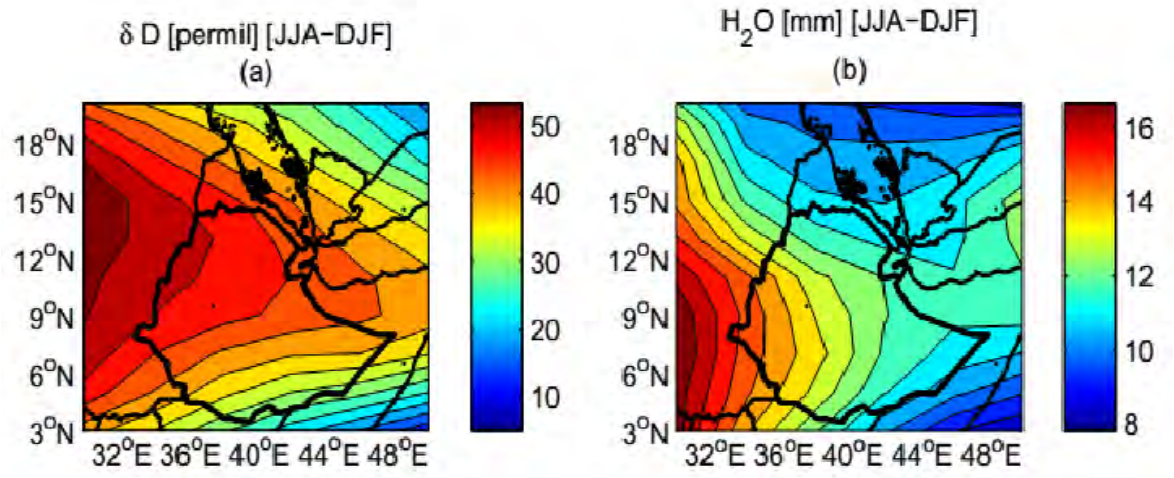

Figure 6.2: Seasonal difference (JJA-DJF) of δD (‰) (a) and water vapour [mm] (b) over Ethiopia, using TES measurements from 2005 to 2010.

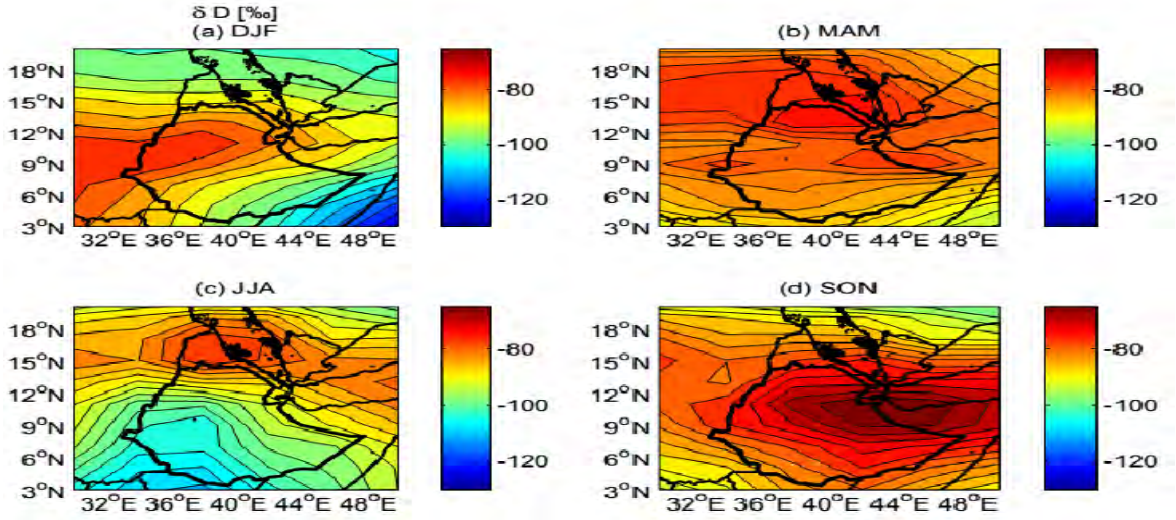

Figure 6.3: Seasonal patterns of integrated water vapour δD (‰) over Ethiopia, based on TES measurements from 2005 to 2010. (a) winter (December, January, and February; DJF); (b) Spring (March, April, and May; MAM); (c) summer (June, July, and August; JJA); (d) fall (September, October, and November; SON).

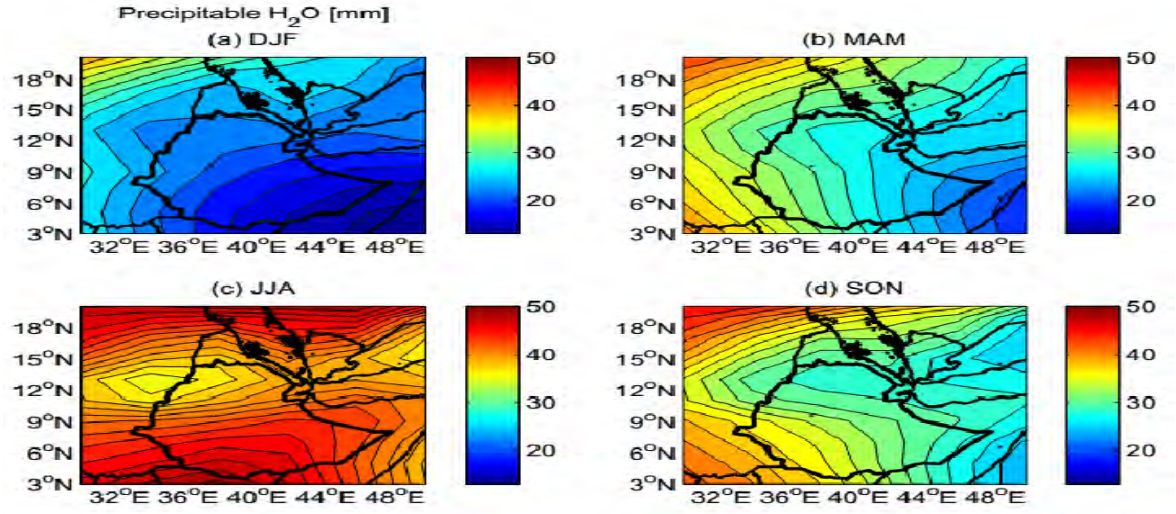

Figure 6.4: Similar to Fig. 6.3 but for integrated water vapour [mm].

flux fields which are derived from the ECMWF ERA-interim reanalysis dataset as well as the fluctuations of incoming/outgoing radiation fluxes due to water for which the parameter of outgoing longwave radiation (OLR) is derived from the National Oceanic and Atmospheric Administration (NOAA) reanalysis data. Therefore, qualitative analysis is performed in the relationships of water vapour and its δD amounts along with the variables of relative humidity, moisture flux fields, and OLR so as to explain the role of local and large-scale processes. Here, the applied moisture flux fields are calculated as vertically integrated values, each representing the atmospheric column between 1000-500 hPa, as well as moisture flux fields at particular pressure level. The divergence of moisture fluxes are computed so as to estimate the rate at which the atmospheric vapour losses due to precipitation or gaining due to evapotranspiration. In this case, positive and negative values of the moisture flux divergence represent the source (related to evapotranspiration) and sink (related to condensation/precipitation) of water vapour, respectively, following the air parcel motion. The global distribution of precipitation is strongly influenced by the availability of water at the continental surface. First, the replenishment of atmospheric water by evaporation, known as continental moisture recycling, sustains precipitation in downwind continental regions. Large fluxes of moisture into and out of the atmosphere by evapotranspiration and precipitation replace atmospheric water vapour, on average, every ten days according to global model estimates [4]. The land-surface evapotranspiration (ET) also makes an important contribution to the spatiotemporal variations of water vapour δD. In most studies dealing with moisture recycling the extent to which precipitation in some location depends on moisture recycling is linked directly to the recycling ratio, R, the fraction of recycled moisture in precipitation. Moisture

recycling can be quantified by the regional recycling ratio (R_r), which measures the contribution of evaporation from a particular region to precipitation inside the same region. The bulk recycling equation applied by [126] is given as:

$$R_r = \frac{E_r}{E_r + 2F_r} \tag{6.1.1}$$

where R_r is the region's mean fraction of recycled moisture in precipitation, F_r is the region's horizontal moisture influx, and E_r is the region's land-surface evaporation.

The spatial distribution of water vapour and its δD amounts in the time scale of seasonal and annual mean basis are presented. Fig. 6.1 illustrates the annual mean of integrated water vapour (b) and its δD (a) over Ethiopia (3°N-15^{o}N, 33^{o}E-48°E) based on TES observations during a period of 6 years, from January, 2005 to December, 2010. As we have seen the spatial distribution of the annual mean of δD over the our region, it is generally influenced by the continental effect, with values decreasing from northeast lowlands to southwest region, which is consistent with the global pattern of δD content [31, 94]. Over the southwest of the region of the domain, the relative humidity is larger than 60% which is substantially high and the observed negative relationship between δD and relative humidity is governed mostly by abundant vapour and enhanced rainout in the region [127, and references therein]. The continental effect is strongly interlinked with the seasonal effect. The alternating of wet and dry seasons over the region of Ethiopia is mainly characterized by the annual movements of the Intertropical Convergence Zone (ITCZ). Wet season is described in association with the northward movement of the ITCZ, whereas the dry season is described in association with the southward movement of the ITCZ. In Fig. 6.2, seasonal difference between summer and winter (JJA-DJF), for δD (‰) (a) and water vapour

[mm] (b), is shown; the maximum difference in δD is found to be in the northern part of the domain, while maximum difference in water vapour amount is occurred over the southwest region. This might be explained by the response of isotope signal with regard to ITCZ movements. The amount effect in isotopic composition of water is in particular occurred in the area where it is affected by the northward movement of the ITCZ. In addition to the mixing and continental effect, there are also different factors such as altitude effect, continental moisture recycle, and seasonal effect, that can cause the enrichment-depletion tendency over the region. Isotope compositions in precipitation originating from the same water vapour source with the same isotope composition will vary in highlands and lowlands. As the distance between the airmass and its source increases during transport, this will enhance the Rayleigh distillation; more isotopic depletion in rainfall. As moisture is transported from a higher altitude to a lower one, more evaporation and re-evaporation processes take place, causing more enrichment in δD compositions in the lowlands and more depleted compositions in the mountains [128]. Isotope compositions vary with distance inland as the heavier isotope forms precipitate first, leaving the vapour enriched in the lighter isotope forms with increasing distance from the origin of the vapour source [129]. Evaporation also occurs with seasonal changes, as precipitation is more susceptible to fractionation processes with the increase in temperature during the summer than during the winter [125]. Moreover, atmospheric water vapour has a differing isotopic composition than rain or snowfall, when evaporation occurs, the isotopic composition of precipitation will be enriched with decreasing elevation as the lighter isotope forms are evaporated first [130].

Furthermore, seasonality of the combined observation of water vapour and its deuterium content over the domain of interest is well presented. Seasonal variations of water vapour δD can provide better constraints on dynamic processes in the atmosphere [31]. It has been depicted the seasonal variations of integrated water vapour δD (see Fig. 6.3) and integrated water vapour (see Fig. 6.4) based on TES data. As can be seen in the figures, for each season, the amount of integrated water vapour and the corresponding δD have distinct pattern over Ethiopia such that different isotope effects/signals are identified. As studied the detailed climatology over Ethiopia in [103, and references therein], most of the western Ethiopia as well as the highlands of south and the east have tropical rainy climate, while the highlands in southwest have warm temperate and tropical rainy climates. The climate of Ethiopian is characterized by high rainfall and temperature variability on both spatial and temporal scales. The variability in distribution is related to altitude, latitude, humidity, and winds, which are the significant factors in affecting the weather system of the country. In winter period, low water vapour amount (Fig. 6.4 (a)) and corresponding large negative values of δD (Fig. 6.3 (a)) appeared over southeast of Ethiopia since this period is characterized by the coldest/dry season, as well as it is highly influenced by the dry continental northeasterly winds. On the other hand, the enrichment characteristic of δD is exhibited over southwest region where it is illustrated a slightly elevated precipitation, as demonstrated in panel (a) of Fig. 6.5, and low relative humidity (see Fig. 6.7) may suggest a higher contribution of continental evapotranspiration to precipitation ($> 50\%$) [131], thus leads to enrichment in δD of vapour.

Spring season (March, April, and May) is the warmest period almost all over the

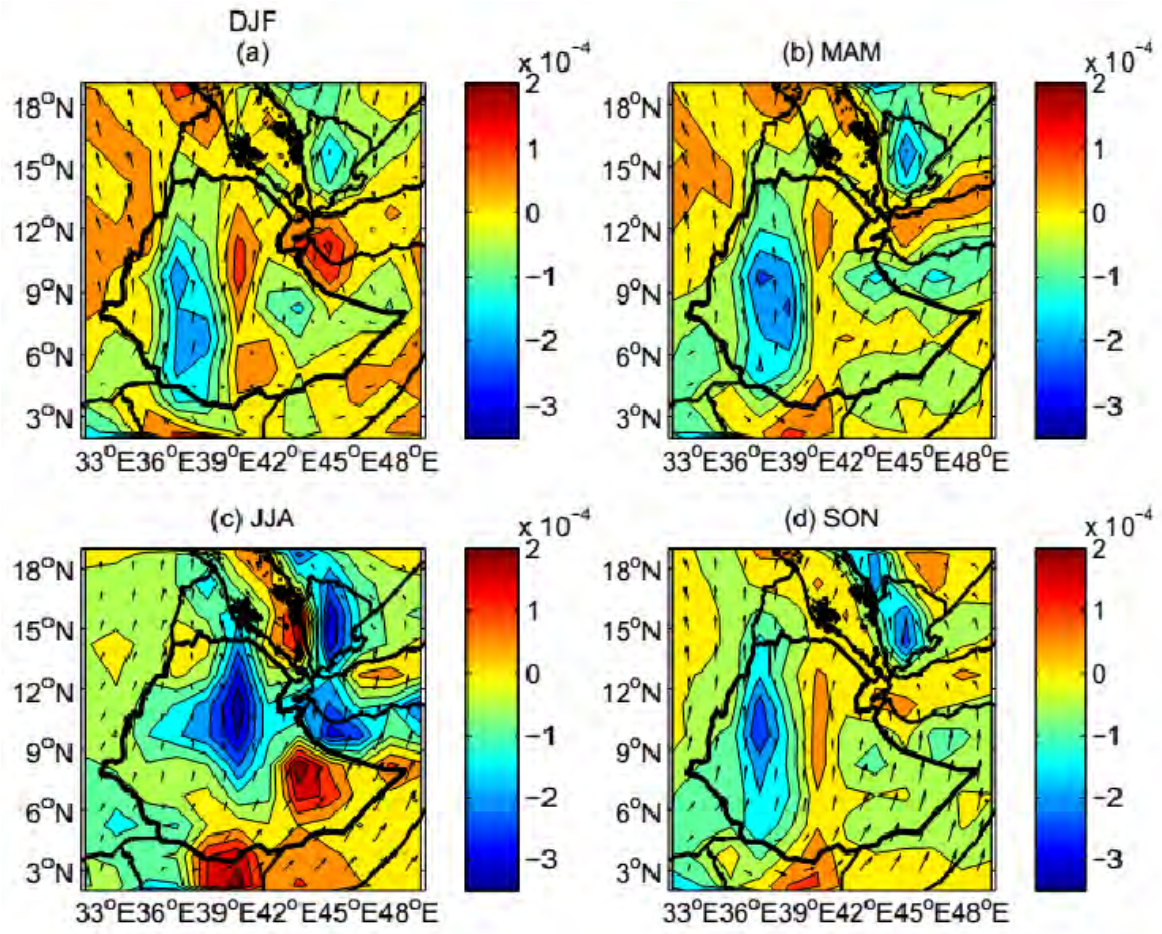

Figure 6.5: Seasonal patterns of vertically integrated moisture flux divergence (kg m^{-2} s^{-1}) (shaded) and vertically integrated moisture flux vectors (kg m^{-1} s^{-1}) (vector) over Ethiopia, calculated from the ECMWF ERA-interim reanalysis data. (a) winter (December, January, and February; DJF) (b) Spring (March, April, and May; MAM); (c) summer (June, July, and August; JJA); (d) fall (September, October, and November; SON).

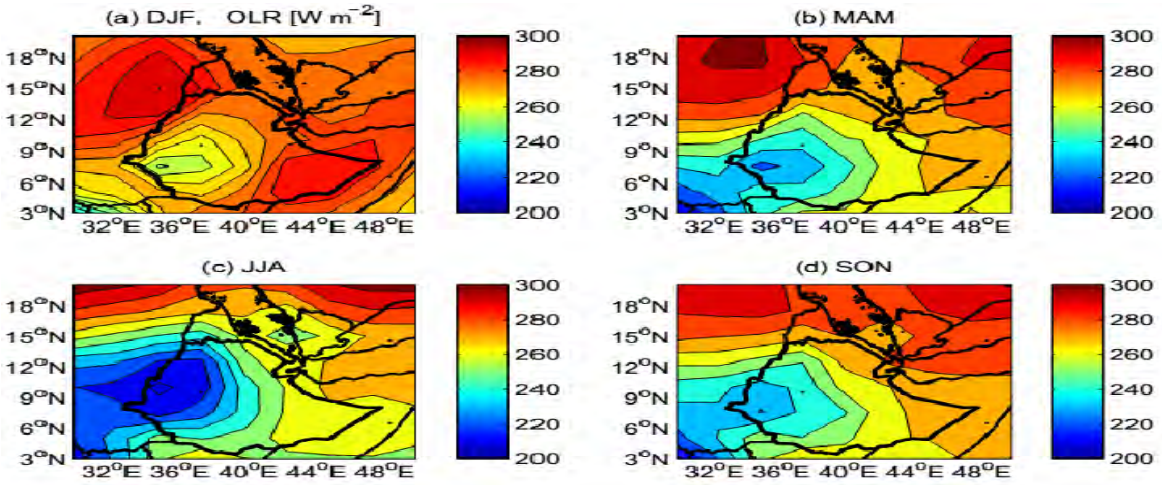

Figure 6.6: Seasonal patterns of outgoing longwave radiation [W m^{-2}] over Ethiopia, using NOAA reanalysis data. (a) winter (December, January, and February; DJF); (b) Spring (March, April, and May; MAM); (c) summer (June, July, and August; JJA); (d) fall (September, October, and November; SON).

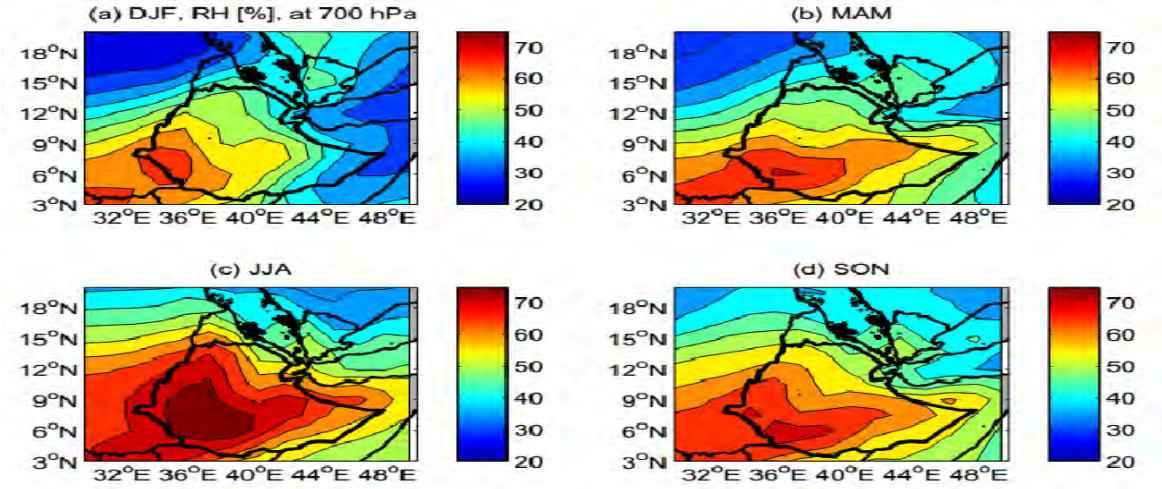

Figure 6.7: Seasonal patterns of relative humidity (RH) [%] over Ethiopia, using ECMWF ERA-interim reanalysis data from 2005 to 2010.

country. During this period, the overall result of δD in vapour indicates the characteristics of enrichment, which might be linked with the contribution of local and continental evapotranspiration. Specifically, more enriched values of δD is well captured over the northeast region where it covers the desert part of the domain of the region, as displayed in Fig. 6.3 panel (b), with low relative humidity, below 50% (see the RH distribution in Fig. 6.7). Moreover, the relative contribution of moisture source using vertically integrated moisture flux divergence fields are assessed; local evapotranspiration is quite large over northeast, whereas continental evapotranspiration is more significant over northwest, as can be illustrated in panel b of Fig. 6.5. In conditions of weak or infrequent rainfall, precipitation re-evaporates relatively quickly or at relatively high altitudes, causing ambient vapour to acquire a relatively high δD characteristic of moisture from near the surface. In brief, liquid precipitation that falls through the atmospheric column below cloud base is subjected to two fractionation processes: first, rain water equilibrates its isotopic composition with the surrounding moisture. The equilibration time depends on drop size and relative humidity. As the moisture at lower levels is typically less depleted than the precipitation at cloud base, the precipitation becomes enriched, and the isotopic composition of the rain at the surface closely resembles that of the moisture near the surface [132]. The larger the rain drops, the higher the fall velocity, and the lower the exchange with the surrounding moisture. Secondly, when precipitation falls through layers of low relative humidity, evaporation from falling droplets leads to an enrichment of the remaining rain, and consequently significantly enriched isotopic signals at the surface. This can in particular be the case in the vicinity of desert areas [49].

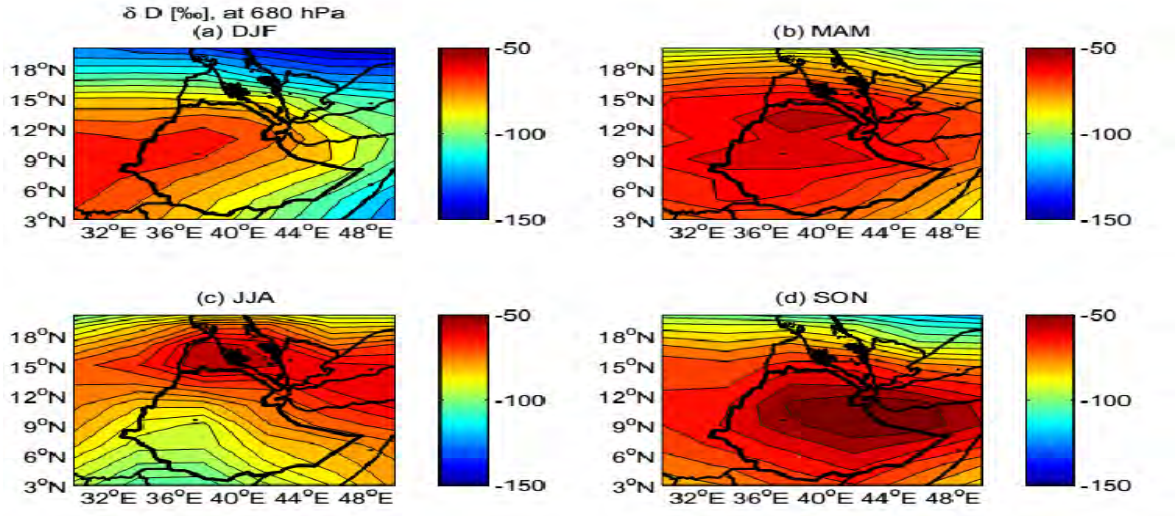

Figure 6.8: Seasonal patterns of δD [‰] at 680 hPa over Ethiopia, based on TES measurements from 2005 to 2010. (a) winter (December, January, and February; DJF); (b) Spring (March, April, and May; MAM); (c) summer (June, July, and August; JJA); (d) fall (September, October, and November; SON).

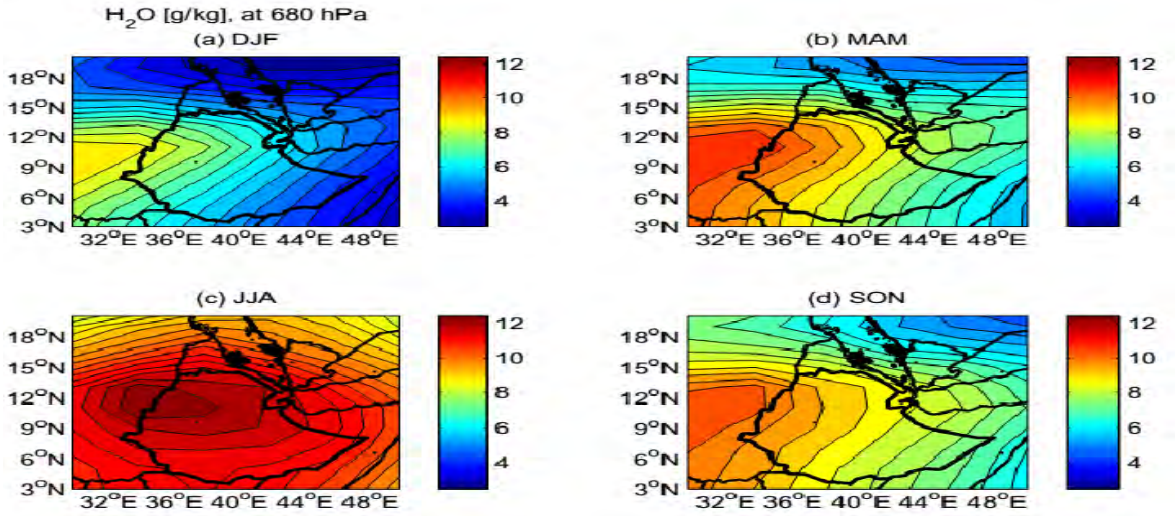

Figure 6.9: Similar to Fig. 6.8 but for H_2O VMR.

In summer season, the contrasting effect has been identified on the combined observation of water vapour and its deuterium content; which means that more negative values in δD (Fig. 6.3 (c)) for the corresponding amount of water vapour (Fig. 6.4 (c)) are clearly noticed. Particularly, this so-called amount effect appears to be large over southwest region. During summer (wet) season, Ethiopia experiences generally southwesterly moisture laden air from South Atlantic and Indian Ocean so that it gets large amount of rainfall [103, references therein]. As stated in the earlier section, the amount effect is closely associated with the northward movement of ITCZ and, to a lesser extent, in other convective precipitation regimes. As reported in recent studies, the amount effect, which is explained by anti-correlated relationship between δD in rainfall and rain rate, is largely modulated by the δD of water vapour in the lower to mid-troposphere. The moisture transport characteristics of monsoon systems are at present not well understood. Again, such systems lead to sustained heavy precipitation with large droplets and relative humidity close to saturation below the cloud, which can allow for the communication of depleted isotopic signals from high altitudes to ground level. Moist convection, depending on the strength, has a significant role in the enrichment-depletion processing of δD in vapour. Conceptually, convection is a process acting mainly on the vertical scale. Moist convection is triggered either by adiabatic, diabatic, or orographic processes in (conditionally) unstable air. Therefore, the spatial variations of moist convection at seasonal time scales in terms of outgoing longwave radiation (OLR) values has been displayed in Fig. 6.6. Strong moist convection, on the order of 220 W m^{-2}, is found to be over the southwest region as depicted in panel c of Fig. 6.6. However, in this particular region, the moisture loss due to precipitation is relatively low, as evident in panel c of Fig. 6.5 and the

relative humidity is high. Rapid vertical upward motion leads to rapid condensation and precipitation formation with large droplets and intense showers. Precipitation falling back through the updraughts equilibrates with the surrounding vapour, and is hence in general less depleted than stratiform precipitation. Large drop size and high precipitation intensity however counteract equilibration. Rapid transport in cold downdraughts can in addition reduce equilibration and lead to episodes of more depleted precipitation. In the same way as depleted moisture from higher altitudes can be recycled into the convective cloud via entrainment, new depleted layers of water vapour form in the high-altitude outflow regions of convective systems [132, 133]. In addition to the rainout of heavy isotopes during condensation, the extent of re-evaporation and exchange under the condensation level is believed to contribute the amount effect [134]. The higher relative humidity during intense convective events reduces both re-evaporation and exchange, and hence reduces the isotopic enrichment of the resulting precipitation. These post-condensation effects are argued by Dansgaard in 1964 [44] to be the primary cause of the amount effect. However, in 1982 Yapp [135] compares observational samples for which post-condensation processes are minimal and finds that a significant component of the amount effect is due to the intensity of precipitation events and the total amount of precipitation.

The monsoon is a large scale wind circulation phenomenon that brings large amount of moisture over our region. During the onward movement of air moisture, the heavy isotopes get systematically depleted and the recycling of moisture due to condensation and subsequent evaporation cause a difference in relative enrichment in deuterium and oxygen isotopic composition. As local precipitation will generally be more isotopically depleted than oceanic moisture, continental recycling reduces the isotopic ratio of

vapour compared to oceanic evaporation [136]. However, as recycling reduces the net rainout of moisture during inland transport, it increases the isotopic ratio of vapour compared to a situation of no recycling, reducing the continental precipitation δD gradient. The cooling of atmospheric moisture during orographic lifting over mountain ranges will also lead to isotopic rainout with altitude.

Seasonal effect of water vapour and its δD amount at 680 hPa (represents lower troposphere) and 464 hPa (represents mid-troposphere) pressure levels are examined based on TES data. Basically, these two different pressure levels are considered according to the sensitivity of vertical information derived from TES averaging kernels of the species. Fig. 6.8 and Fig. 6.9 demonstrate seasonal variation of δD and H_2O VMR at 680 hPa, respectively, whereas Fig. 6.10 and Fig. 6.11 depict δD and H_2O VMR at 464 hPa, respectively over the domain of the study. The spatial patterns of H_2O VMR and its δD in the respective altitudes for each season reflect a similar characteristics with that of the integrated column amounts; during winter period the enriched δD values are displayed over the southwest region; in fall (SON) season the enhanced δD values are confined in the northern part; both spring (MAM) and summer (JJA) seasons exhibit the enrichment characteristics of δD nearly the same parts of the domain (around northeast-southeast region). As discussed in earlier chapter, the water vapour isotopic composition in the lower troposphere is sensitive to the origin of water vapour and precipitation, such as continental recycling [24, 58] or air mass origin [27]. In the tropics, the fraction of the vapour originating from continental evaporation increases with altitude and reaches a maximum in the upper troposphere, which is due to fast injection of continental-evaporated water vapour by deep convection over land regions. If the increase in H_2O VMR is associated

with an increase in moisture convergence, then this moisture convergence will bring moisture from further away and with a larger proportion of oceanic moisture. For further understanding of the processes that are responsible for the seasonal variations of δD in vapour over the region, as diagnostic purpose seasonal patterns of moisture flux divergence (kg m^{-2} s^{-1}) at 700 hPa and 500 hPa pressure levels are assessed, as illustrated in Fig. 6.12 and Fig. 6.13, respectively. Lower relative humidity (most values $< 60\%$) implies lower condensation/precipitation, thus leads to continental moisture recycling, and the subsequently it turns out to be high δD values, such characteristics are appeared over the northern part of the region during summer and spring seasons (see Fig. 6.12 and Fig. 6.7). The slightly elevated precipitation (see Fig. 6.12) and low relative humidity ($> 50\%$) in winter (see Fig. 6.7) may suggest a higher contribution of continental evapotranspiration to precipitation [131], which leads to enrichment of δD in vapour. In our study, this effect is also observed toward the west along the center of the region, as shown in panel (a) of Fig. 6.7.

The highest variability in δD is observed in October and June. The most plausible explanation for this variability is related to the northward and southward passage of the ITCZ over central Ethiopia. This creates variable local atmospheric condition. Strong convection and high altitude condensation with in the air column associated with the front of the ITCZ while it is moving north results in the most depleted δD.

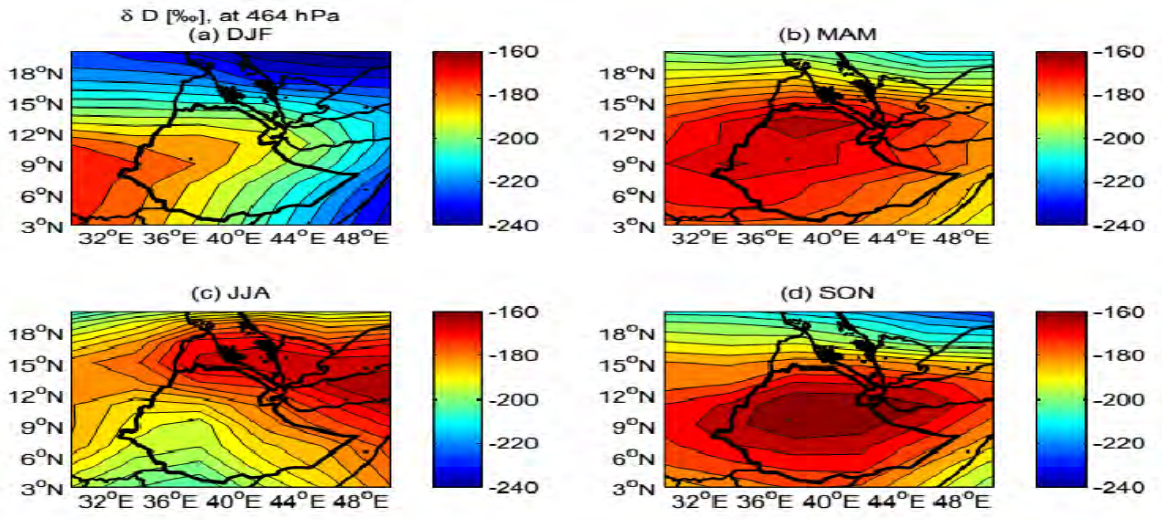

Figure 6.10: Similar to Fig. 6.3 but for pressure level of 464 hPa.

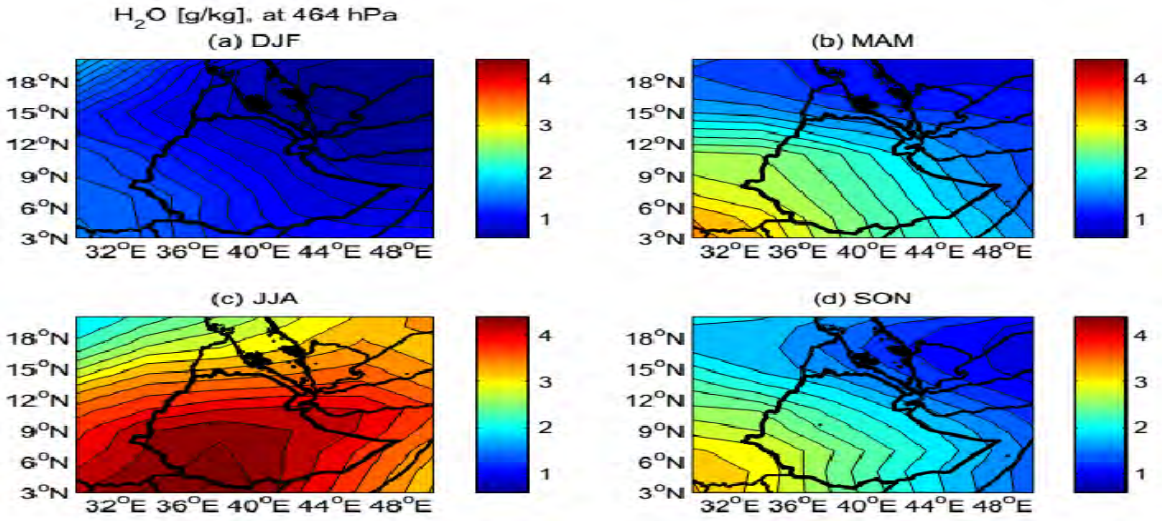

Figure 6.11: Similar to Fig. 6.3 but for H_2O VMR at pressure level of 464 hPa.

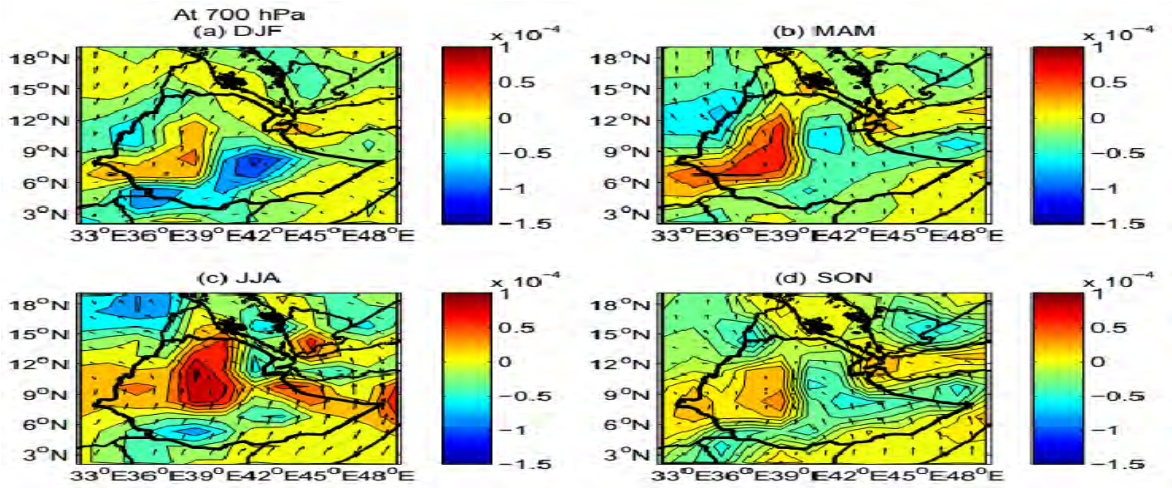

Figure 6.12: Seasonal patterns of moisture flux divergence (kg m^{-2} s^{-1}) and moisture flux vector at 700 hPa over Ethiopia, calculated from the ECMWF ERA-interim reanalysis data. (a) Winter (December, January, and February; DJF) (b) Spring (March, April, and May; MAM); (c) Summer (June, July, and August; JJA); (d) Autumn (September, October, and November; SON).

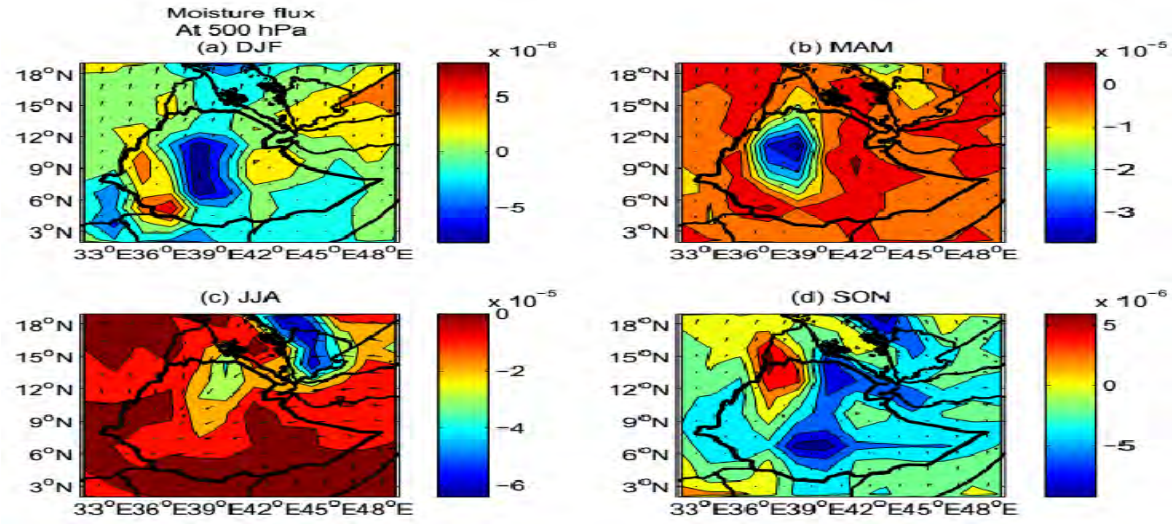

Figure 6.13: Similar to Fig. 6.12 but for pressure level of 500 hPa.

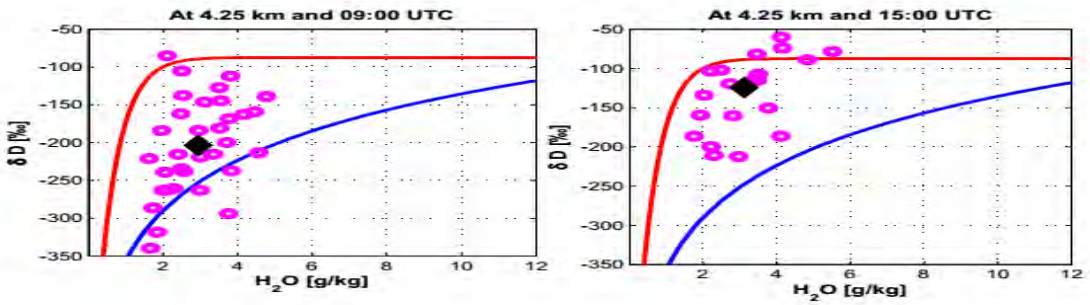

Figure 6.14: Scatter plot of hourly water vapour (H_2O) versus its δD at measurement site (green dots) derived from FTIR, December, 2012 to March, 2013. Black diamond symbols represent mean values of water vapour versus its δD. The blue line represents Rayleigh distillation line calculated for initial condition of δD = -79‰ (a value for vapour in equilibrium with ocean water) at T = 25°C. The red curve denotes the mixing line based on two isotopically distinctive air masses (δD = -350‰ and δD = -79‰) initializing at a water vapour mixing ratio of 0.5 g/kg.

6.2 The relationships among δD, δ^{18}O, and H_2O

6.2.1 δD versus H_2O for VMR profiles from FTIR

The discrepancy between the observations and a simple Rayleigh fractionation-based prediction is a baseline for our investigation to understand the processes that determine the distribution of H_2O and δD values in the troposphere. Here, we have analyzed the relative contribution of tropospheric processes that are responsible for the variations of water vapour and its δD contents in the lower troposphere at the measurement site located in Addis Ababa, based on ground-based FTIR observations. In order to characterize the role of these processes, we have employed a method of physical modeling with which we have constrained the coupled observations between

δD and H_2O VMR. Detailed descriptions about the physical modeling can be found in [6]. Using theoretical curves, we have illustrated the relationships between δD and H_2O for VMR amounts on hourly basis during a period between November, 2012 and March, 2013. Fig. 6.14 illustrates the observations (cyan circle symbols) are conducted at local time of 09:00 UTC (left panel) and 15:00 UTC (right panel) at the altitude level of 4.25 km. In this figure, the blue line represents Rayleigh distillation line calculated for initial condition of δD = -79‰ (a value for vapour in equilibrium with ocean water) at T = 25°C. The red curve denotes the mixing line based on two isotopically distinctive air masses (δD = -350‰ and δD = -79‰) initializing at a water vapour mixing ratio of 0.5 g/kg. In fact, a simple single-process modeling approach can be confounded by more complex airmass histories involving such as air mass mixing. Airmass mixing during transport can lead to large deviations from a Rayleigh prediction [140]. Using such qualitative approach, the mean situation of morning observations is more closely described by the Rayleigh condensation curve, whereas for afternoon observations it is better explained by the mixing curve. For instance, as reported in the previous studies the water vapour isotopic composition in the lower troposphere, which were conducted at different sites, is mainly sensitive to the origin of water vapour and precipitation, such as continental recycling [24, 58], local evapotranspiration [138, 139], or air mass origin [27]. These findings are consistent with results presented in this study.

However, as such qualitative analysis, we find that some observations do not follow either a pure Rayleigh distillation line or mixing line. Thus, it leads to further investigation in terms of quantitative relationship between δD and q (q represents H_2O) at different altitude levels with respect to the local observation time of 09:00 UTC and

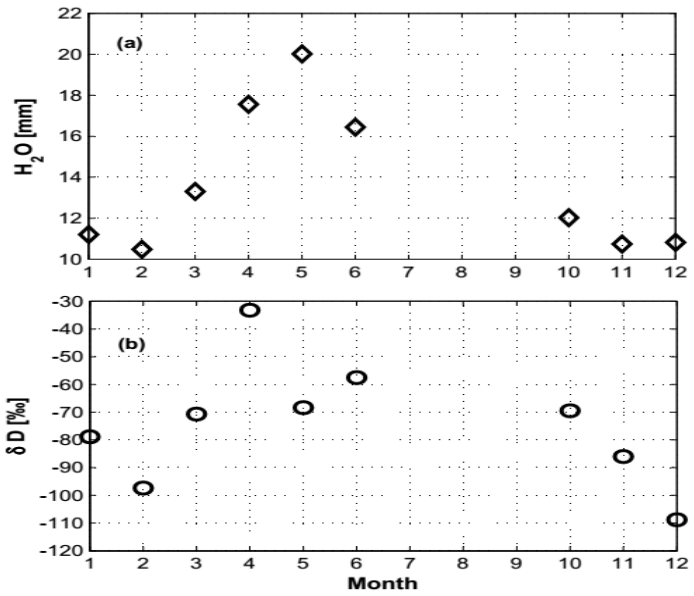

Figure 6.15: Monthly mean of column integrated H_2O (top panel) and δD amounts (bottom panel) as derived from FTIR during a period of June, 2009 to March, 2013.

Table 6.1. Relationships between FTIR H_2O (represented by q) (g/kg) and δD during a period between December, 2012 and March, 2013 are given below. Measurements considered at the local time of 09:00 UTC and 15:00 UTC, at 4.25 km altitude level, separately. **NS** means statistically insignificant and R is correlation coefficient.

	At 09:00 UTC	At 15:00 UTC
R for ln(q) vs. δD	0.44	0.34 (**NS**)
R for 1/q vs. δD	-0.47	-0.33 (**NS**))

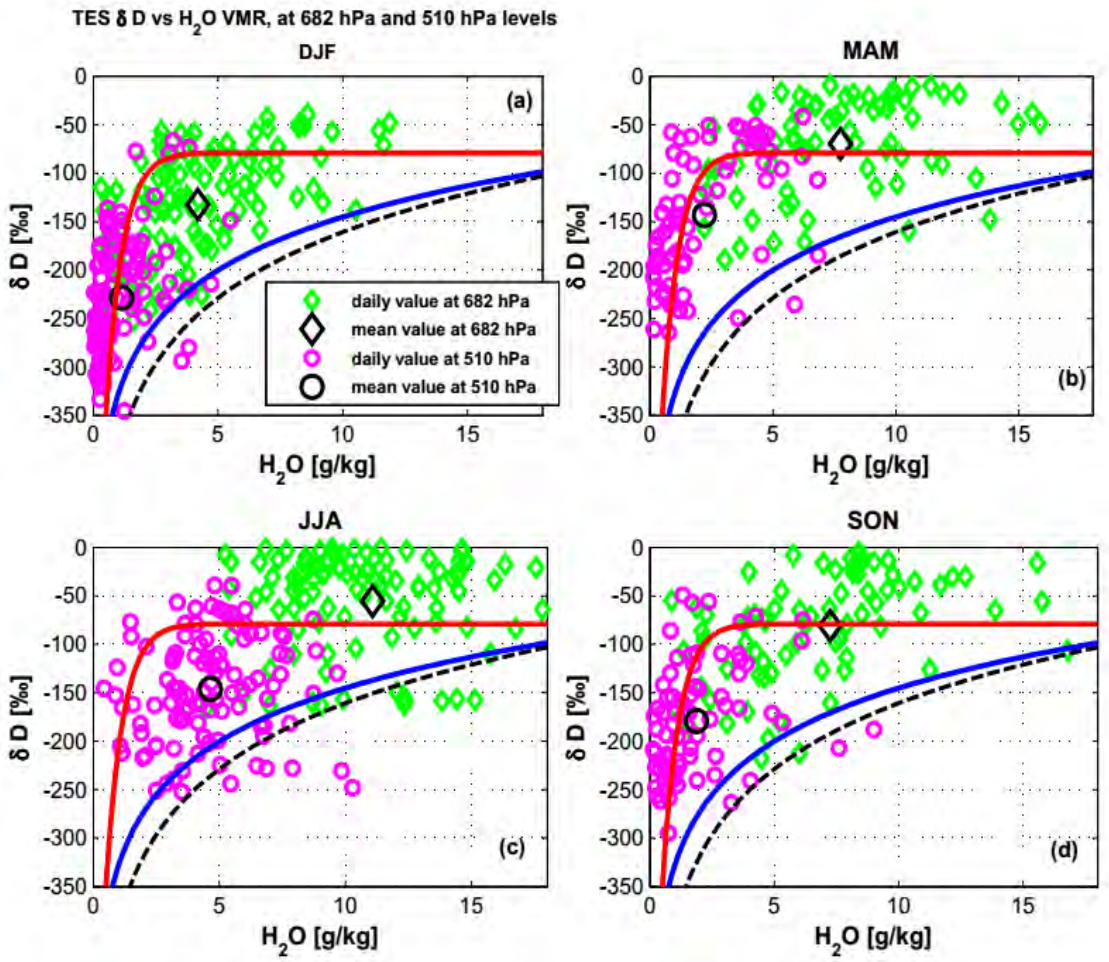

Figure 6.16: Scatter plot of daily water vapour versus its δD at measurement site (green diamond symbols) at 682 hPa and (magenta circle symbols) 510 hPa as derived from TES level 2 data in the period between 2005 and 2012. Black diamond symbols represent seasonal mean values of water vapour versus its δD. The blue line represents Rayleigh distillation line calculated for initial condition of δD = -79‰ (a value for vapour in equilibrium with ocean water) at T = 25°C. The black broken line shows modified Rayleigh distillation line (considered 30% re-evaporation process). The red curve denotes the mixing line based on two isotopically distinctive air masses (δD = -350‰ and δD = -79‰) initializing at a water vapour mixing ratio of 0.5 g/kg.

15:00 UTC separately from December, 2012 to March, 2013, as given in Table 6.1. The role of Rayleigh condensation process is determined by the linear relationship between δD and $\ln(q)$. This result showed that δD of atmospheric water vapour at the measurement site exhibited statistically significant ($p<0.001$) ln-linear dependence on q, which suggests there is a dominating effect of Rayleigh distillation accompanied by the advection of airmass. And also, the influence of mixing process is determined from the expected co-variation between δD and $1/q$ [141]. As evident in Table 6.1, the magnitude of the correlation strength between δD and $\ln(q)$ is found to be slightly larger for the observations taking at 15:00 UTC than 09:00 UTC local time for the corresponding altitude level of 4.25 km. This suggests that the Rayleigh condensation process is more affected by mixing process during the observation conducted at 09:00 UTC. At 15:00 UTC, the magnitude of correlation coefficients are given, but statistically insignificant, which might be explained by the influence of the boundary convective mixing and the strength of wind speed. As reported in [142, 55], the impact of wind speed strength on the effect of the non-equilibrium fractionation process is described. For high wind speeds the water vapour transport is the same for all the isotopes. For small wind speeds, molecular diffusivity has a more pronounced impact on water vapour transport, which leads to non-equilibrium isotopic fractionation.

6.2.2 δD versus H_2O from TES

Based on TES observations, we are able to identify the prominent atmospheric processes that controlling the seasonal variations of water vapour and its δD amounts in the troposphere using a similar qualitative approach as stated in the previous section. Fig. 6.14 displays water vapour (g/kg) versus its δD (‰) for each season on

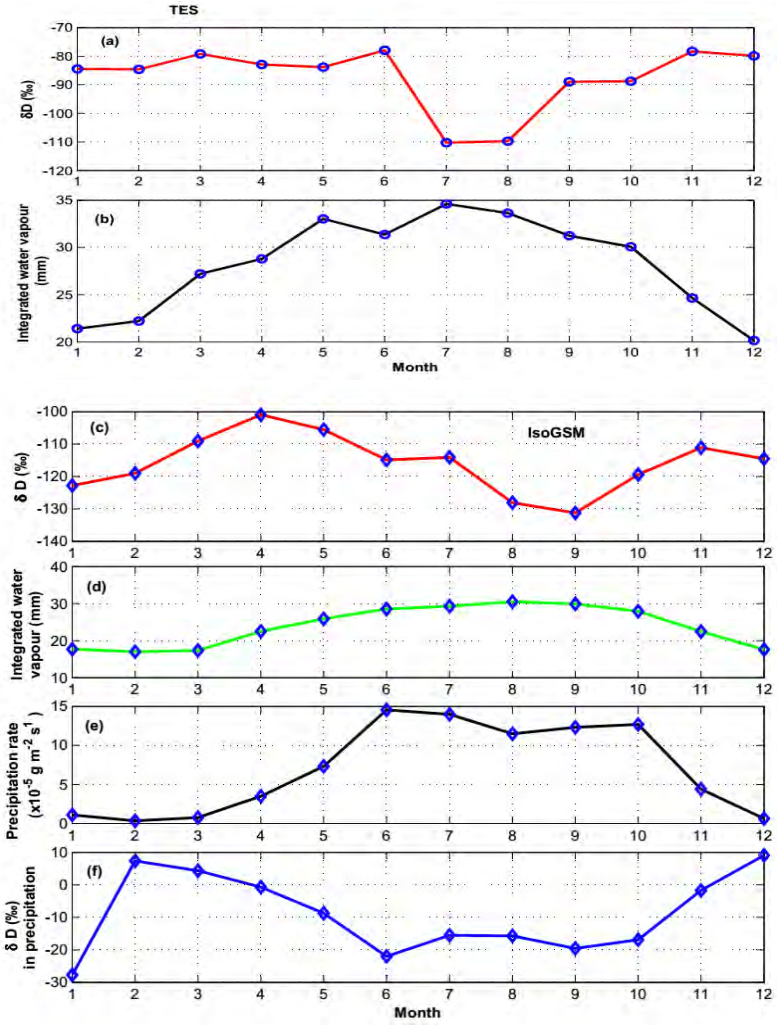

Figure 6.17: Monthly mean from TES observations and IsoGSM model, 2005-2010. For TES: (a) isotopic composition in integrated water vapour and (b) integrated water vapour (mm). For IsoGSM: (c) isotopic composition in integrated water vapour, (d) integrated water vapour (mm), (e) precipitation rate, and (f) isotopic composition of precipitation

the daily basis at the measurement site (green diamond symbols) at 682 hPa and (magenta circle symbols) 510 hPa as derived from TES level 2 data in the period between 2005 and 2012. Black diamond and circle symbols represent seasonal mean values of H_2O vs. δD at 682 hPa and 510 hPa, respectively. The blue line represents Rayleigh distillation line calculated for initial condition of δD = -79‰ (a value for vapour in equilibrium with ocean water) at T = 25°C. The black broken line shows modified Rayleigh distillation line (considered 30% re-evaporation process). The red curve denotes the mixing line based on two isotopically distinctive air masses (δD = -350‰ and δD = -79‰) initializing at a water vapour mixing ratio of 0.5 g/kg. Rayleigh distillation means that all water that condenses during the transport pathway is immediately removed from the airmass. Measurements that lie above the Rayleigh curve, suggesting that advective mixing between moist air with relatively high δD and dry air with relatively low δD controls the isotopic composition of the water vapour, this explains a large number of observations that made almost all seasons. Measurements that fall below the Rayleigh curve are associated with convective moisture recycling, whereby the vapour and liquid coexist after condensation and entrainment of low δD water vapour from unsaturated down drafts decreases the isotopic ratios in the convective system [e.g., [38, 143]], and this could partly describe some observations in summer season. Enrichment characteristics are identified at 682 hPa level in all seasons, which is likely caused by local moisture source (this effect might be more important in spring, summer, and autumn) and continental moisture recycling (this effect might be dominate in winter) due to the enriched signature of transpiration.

In addition, the seasonal cycles on the integrated water vapour and its δD content

are also examined. Fig. 6.17 shows the time series of monthly mean of TES column integrated water vapour (b) and its δD (a). This monthly mean is computed only from the day time observations. As illustrated in the figure, the maximum and minimum amounts of water vapour are observed during summer and winter, respectively. However, in these seasons the corresponding δD amounts are exhibited on the reverse of H_2O abundance pattern, enriched values in winter and depleted values in summer. This seasonality on the distribution of water vapour isotopologues is further diagnosed with the help of isotope-enabled GCM (IsoGSM) simulated model output using qualitative approach. In a similar figure, the monthly mean isotopic composition from IsoGSM is illustrated in Fig. 6.17: (c) isotopic composition in integrated water vapour, (d) specific humidity (g/kg), (e) precipitation rate, and (f) isotopic composition of precipitation from the simulated values by the IsoGSM. The model output shows a good agreement in patterns of precipitation rate, its isotopic composition, winter-enriched and summer depleted. As a result, we found that the consistent patterns on the distributions of water vapour amount between TES observations and IsoGSM model. In IsoGSM case, monthly mean fields calculation is based on every 6 hour. Obviously, the different temporal sampling of observation and model could impart the discrepancy. In addition, the TES instrument preferentially samples clear-sky conditions because remotely sensed δD has its own sensitivity and is subject to sampling biases related to the presence of clouds [93]. The clear-sky air parcels are relatively dry and enriched in heavy isotope compared to those of cloudy observations over tropics.

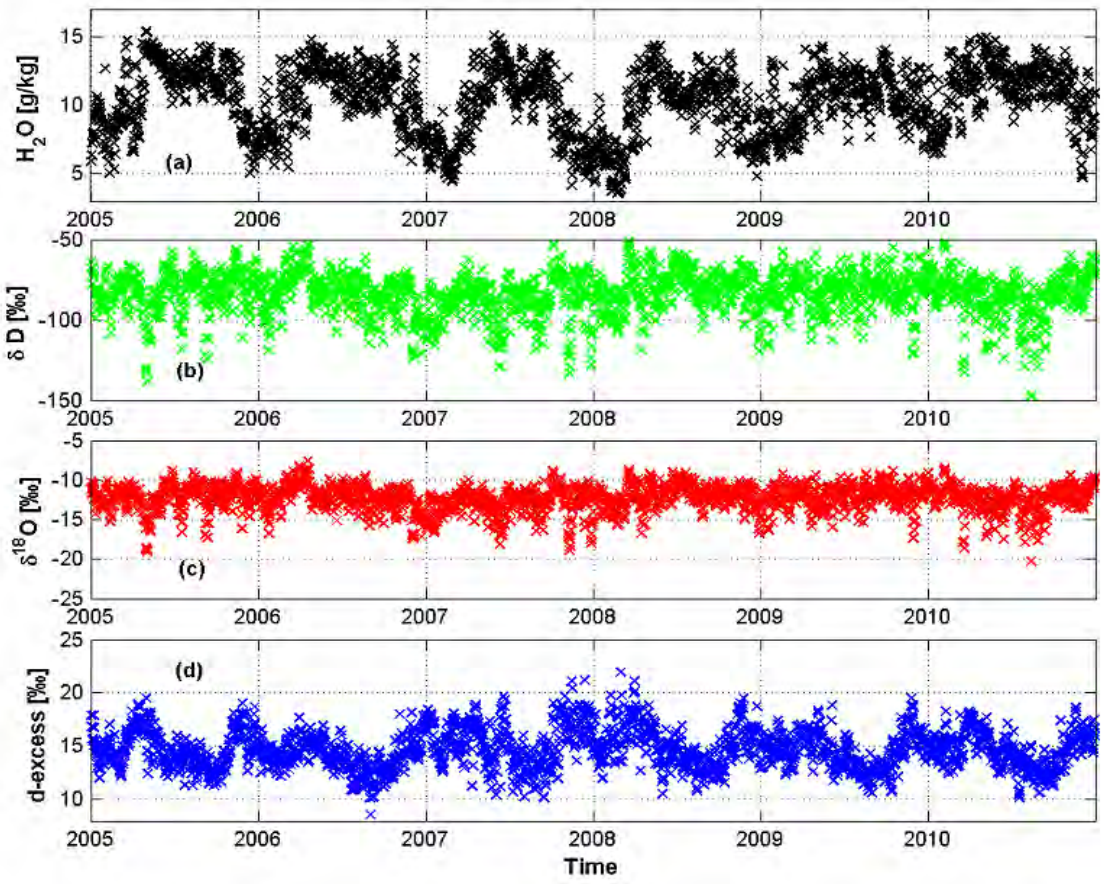

Figure 6.18: The time series of (a) H_2O, (b) δD, (c) δ^{18}O, and (d) d-excess in the near surface vapour from IsoGSM model output on daily mean basis a period between 2005-2010.

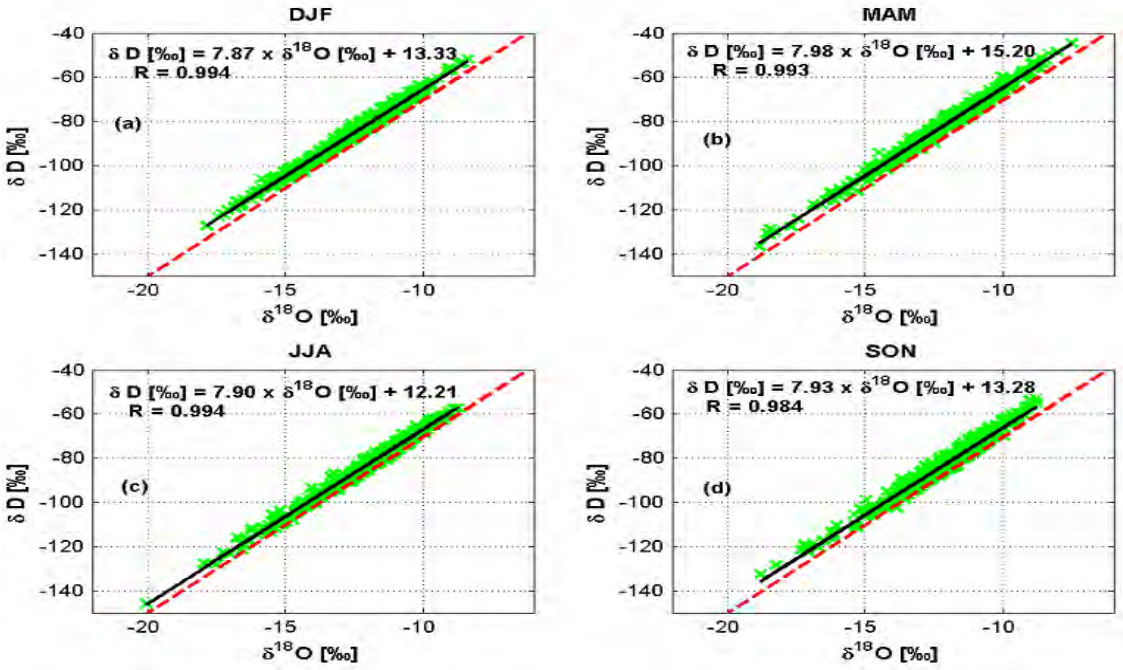

Figure 6.19: δ^{18}O versus δD in the near surface vapour from IsoGSM model during 2005-2010. For reference, the GMWL is plotted in each panels (red broken line). Deuterium-excess (d) is a measure of the deviation from the GMWL in δD (‰). All panels represent different seasons: (a) December, January and February (DJF), (b) March, April and May (MAM), (c) June, July and August (JJA), and (d) September, October and November (SON).

6.2.3 H_2O, δD, and δ^{18}O from IsoGSM

The use of an isotope enabled IsoGSM provides us with additional large scale information for the interpretation of our local observations. Thus, we have presented IsoGSM simulated results of the isotopic composition of water vapour near the surface and precipitable vapour. The temporal variations of water vapour and its isotopic compositions (δD, and δ^{18}O) near the surface are related to the atmospheric processes such as air mass advection, precipitation, evapotranspiration and entrainment from the free atmosphere [144, 145, 146]. Fig. 6.21 illustrates the time series of daily mean of H_2O (a), δD (b), δ^{18}O (c), and d-excess (d) in the near surface vapour from IsoGSM model output during 2005-2010. Thus the clear seasonal cycles are exhibited in H_2O and d, with the respective ranges of variation from 3 g/kg to 16 g/kg and 8 to 23 ‰, respectively. In the case of H_2O, maximum values are observed in summer, and minimum values in winter, whereas in d maximum and minimum values are found in winter and summer, respectively. As reported in [44], the low d values in heavy tropical rainfall are the result of deep convectional cooling and reduced influence of enrichment processes. Generally higher d values can be attributed to continental moisture recycling, which increases the d of moisture by repeated evaporation from soil water with higher d compared to ocean water. Post-condensational exchange can thus lead to an increase of d in vapour during light rainfall at relative humidity less than 100 % [148].

We found that the diurnal cycle of d is slightly greater than the day to day variations, this indicates that there is a dominating effect of local scale processing. The observed values of d during midday is larger than the evening and the morning values. In early interesting work regarding d diurnal cycles as reported in [138] in the meta-analysis

of water vapour measurements from six different sites located in various ecosystems (forest, grassland, agricultural and urban settings), all of which showed the general feature of d midday increase with remarkably similar phases in the time progression. Throughout all the studies mentioned, the magnitude of d daily variations ranges from $\sim$5 ‰ to $\sim$20 ‰ from site to site, but all share the same timing (decrease during the evening and the night with more rapid recovery in the morning). Similarly, the mechanism that control the diurnal cycle of d in the mature open canopy ponderosa pine forest reported in [139], the diurnal cycle of d is a result of dew-fall and vapour-liquid interaction within the canopy. The morning burst is caused by initiation of transpiration and one would therefore expect an inverse relationship between the strength of the diurnal d cycle and the increase in humidity during the morning burst.

δD vs. δ^{18}O

We have assessed the relationship between δD and δ^{18}O in the near surface vapour and in the integrated vapour on seasonal time scale. Fig. 6.19 shows the relationship between surface vapour δD and δ^{18}O through the period 2005 to 2010 for each seasons including correlation coefficients and fitted parameters on daily mean basis, and Fig. 6.20 illustrates their relationship in the precipitable vapour. GMWL is plotted in all panels in the given figures represented by the red broken line is used as reference. Near surface vapour δD and δ^{18}O are distributed closely along the GMWL, suggesting that no significant evaporative enrichment takes place. The slope of the water line depends on relative humidity (RH) during secondary sub-cloud evaporation, such that evaporation of droplets after condensation from the cloud lead to a slope less

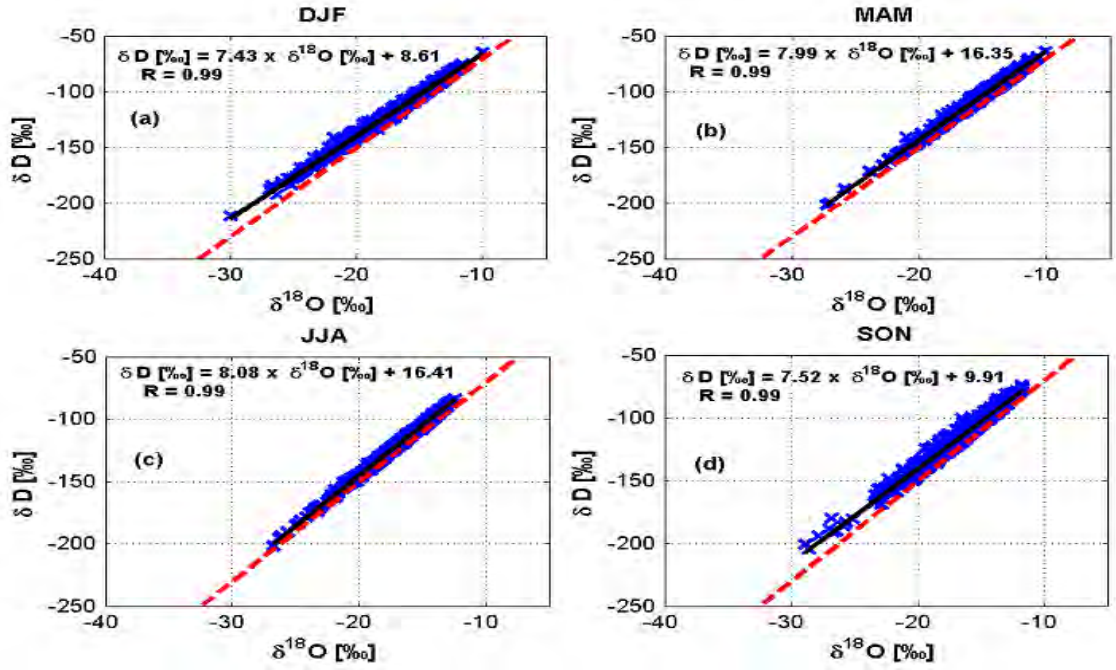

Figure 6.20: Similar to Fig. 6.19 but for precipitable vapour.

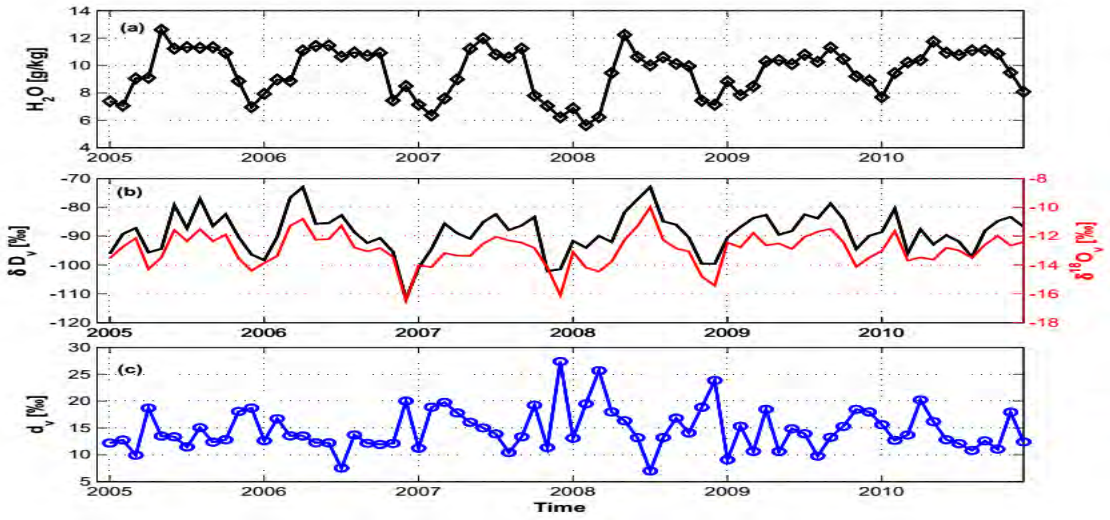

Figure 6.21: The time series of H_2O (a), $\delta^{18}O$ (red line) and δD, (black line) (b), d_v (c) in vapour on monthly mean basis from IsoGSM model simulations during 2005-2010.

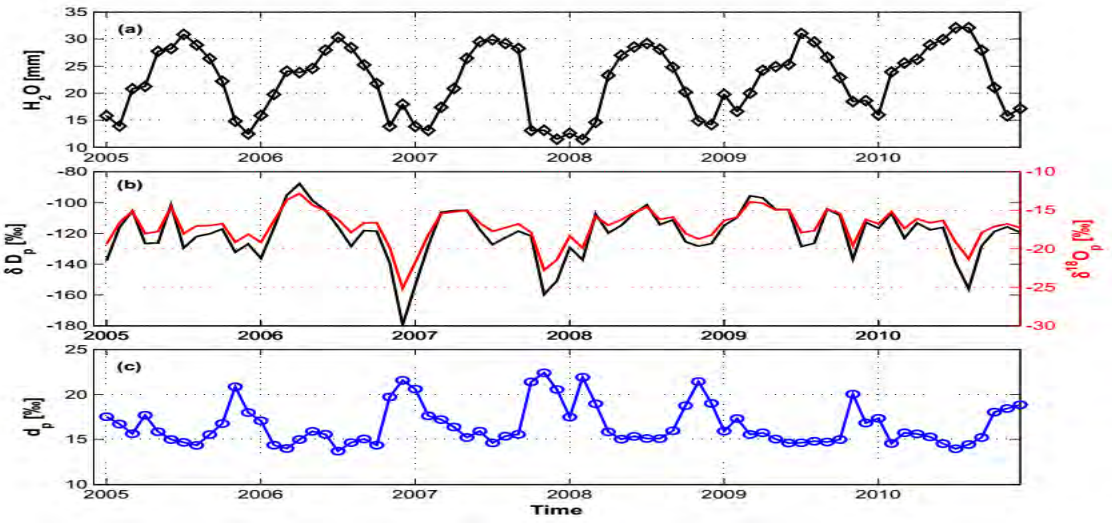

Figure 6.22: The time series of (a) H_2O, (b) $\delta^{18}O$ (red line) and δD, (black line), (c) d_p in precipitable vapour on monthly mean basis from IsoGSM model output during 2005-2010.

Table 6.2. The mean, standard error of the mean (mean ± standard deviation) on the daily mean basis for the IsoGSM model outputs of H_2O (g/kg), δD_v, $\delta^{18}O_v$ and d_v (‰) in a 2m specific humidity for each seasons (DJF (December to February), MAM (March to May), JJA (June to August), SON (September to November)) during a period 2005-2010 are given below.

	DJF	MAM	JJA	SON
H_2O	7.90 ± 1.98	10.85 ± 2.38	11.54 ± 1.21	10.59 ± 1.97
δD_v	-85.63 ± 12.98	-81.87 ± 13.27	-83.10 ± 13.17	-81.99 ± 11.82
$\delta^{18}O_v$	-12.58 ± 1.64	-12.16 ± 1.65	-12.06 ± 1.66	-12.02 ± 1.47
d_v	15.01± 1.48	15.42 ± 1.57	13.39 ± 1.43	14.13 ± 2.09

than 8 [147]. As shown in Fig. 6.19, values of the slope exhibit slight variations in all seasons, values ranging from 7.87 to 7.98 ($R \geq 0.984$) which is slightly less than the slope of GMWL. This explains the temperature-dependent effect of equilibrium fractionation on δD is slightly less than δ^{18}O. All intercept values are larger than 10 ‰ (see Fig. 6.19 and Table 6.3), which are attributed to the local contribution. In the integrated vapour, the values of the slope are 7.43 in winter season and 7.52 in autumn season, the corresponding intercepts are 8.61 (winter) and 9.91 (autumn), as shown in Fig. 6.20. Thus, the overall results suggest the temperature-dependent effect of equilibrium in both winter and autumn seasons. In summer and spring, the slope is almost 8, the corresponding intercepts are 16.41 (summer) and 16.35 (spring) (see Fig. 6.20), which is greater than the intercept defined by GMWL of 10. Summer and spring seasons are rather well driven by the local processing. In the other way, we have quantified the relationships for δD versus d and δ^{18}O versus d in precipitable vapour with respect to seasonal time scale, provided in Table 6.4. Variations in d that are mainly driven by large changes in δD will reflect temperature dependency. Or, variations in d that are mainly driven by changes in δ^{18}O should rather reflect

remote/distant moisture source changes. The correlations shows for δD versus d is -0.552 and for δ^{18}O versus d is -0.623 during winter (dry) season. These findings indicate the variability is largely modulated by remote source moisture variability in winter season. However, in summer (wet) season we found positive correlations, R = 0.219 for δD versus d and R = 0.155 for δ^{18}O versus d. Furthermore, seasonal cycle of δD and H_2O in precipitable vapour is examined (see Fig. 6.17). Summer period is better revealed by 'amount effect'. Interestingly, recent studies have revealed the 'amount effect' characterizing by the anti-correlation between δD in rainfall and rain rate in the lower and mid-troposphere. In conditions of weak or infrequent rainfall, precipitation re-evaporates relatively quickly or at relatively high altitudes, causing ambient vapour to acquire a relatively high δD characteristic of moisture from near the surface. But in persistently rainy and more humid conditions, precipitation tends to evaporate more slowly while falling more rapidly, thus allowing relatively depleted rainwater formed aloft to equilibrate with vapour at low levels such that this vapour gradually becomes depleted as well [134].

Table 6.3. The statistical relationships for d vs. H_2O (g/kg) and δ D vs. $\delta^{18}O$ in the near surface vapour from IsoGSM during a period 2005-2010. Linear Least Squares Fits Between daily means in each seasons, m = slope, b = intercept, R = correlation coefficient, and P = statistical significant test.

	DJF	MAM	JJA	SON
d vs. H_2O				
R	-0.454	-0.117	0.218	-0.595
P-value	< 0.0001	< 0.0001	< 0.005	< 0.0001
Slope	-0.340	-0.077	0.258	-0.632
b	17.7	16.25	10.41	20.82
δ D vs. $\delta^{18}O$				
R	0.994	0.993	0.994	0.984
P-value	< 0.0001	< 0.0001	< 0.0001	< 0.0001
Slope	7.87	7.98	7.903	7.93
b	13.33	15.20	12.21	13.28

Table 6.4. Statistical and regression analysis among H_2O (mm), δD, $\delta^{18}O$ and d (deuterium excess) in the precipitable vapour from IsoGSM model, 2005-2010. These are given with respect to seasons on daily mean basis.

	DJF	MAM	JJA	SON
d vs. H_2O				
R	-0.576	-0.499	-0.398	-0.764
p	< 0.0001	< 0.0001	< 0.005	< 0.0001
m	-0.33	-0.165	-0.193	-0.453
b	24.06	20.7	20.75	28.13
δ D vs. $\delta^{18}O$				
R	0.995	0.996	0.998	0.987
p	< 0.0001	< 0.0001	< 0.0001	< 0.0001
m	7.43	7.99	8.08	7.52
b	8.61	16.35	16.41	9.91
δ D vs. d				
R	-0.552	0.078	0.219	-0.200
p	< 0.0001	< 0.06	< 0.0001	< 0.0001
$\delta^{18}O$ vs. d				
R	-0.629	-0.011	0.155	-0.358
p	< 0.0001	< 0.8	< 0.0001	< 0.0001

Chapter 7

Upper troposphere and lower stratosphere water vapour budget

Recent study [151] reported the diurnal variations of both H_2O and carbon monoxide (CO) in the Upper Troposphere (UT) (146 hPa) and the Tropical Tropopause Layer (TTL) which is represented by a pressure level of 100 hPa in the inter-tropical belt (20° N - 20° S) using Microwave Limb Sounder (MLS) version 2.2 datasets for 2005 - 2008 period. In such analysis showed, on average in September-November and in March-May, strong evidence of H_2O diurnal variations over land attributed to the diurnal cycle of convection intensity displaying maximum in late afternoon followed by a morning decrease [152]. H_2O and CO diurnal variations in the UT are consistent with that of vertical transport by deep convection. Larger water vapour and CO concentrations were found at night than during the day, because of the convective uplift in the afternoon and the early evening. Both concentrations are observed to decrease with the weakening of convection and the horizontal mixing, resulting in a minimum around local noon. Diurnal variations were also observed at higher levels in the TTL

but, while the CO concentration remained the largest at night, that of H_2O was found largest during the day. Since H_2O and CO are lofted simultaneously, but H_2O was transformed into ice [151]. Their diurnal variations in the TTL were then associated to the diurnal cycle of temperature, itself linked to the diurnal cycle of the cooling resulting from convective lofting of adiabatically cooled air. Very recently, [153] reported that the water vapour concentration showed a systematic diurnal cycle with a night-time peak in the tropical upper troposphere and the opposite in the TTL (121 to 68 hPa) and the tropical Lower Stratosphere, of larger amplitude above continents than continental-oceanic areas such as the maritime continent or full oceanic areas such as the Western Pacific.

On the account of those reasons, it has been dealt with one of the most debated aspect of the TTL and the LS budget of water vapour. Therefore, it is encouraged for making further studies in identifying of the detailed mechanisms that are responsible for the budget of H_2O amount in the region between upper troposphere and lower stratosphere at local scale. The focus of our site is located within inner tropics, its latitude and longitude are 9.01°N and 38.76°E, respectively. The role of local convection and temperature in determining the water vapour amount on the upper troposphere and lower stratosphere are quantified. Therefore, for this purpose of analysis, the following parameters are considered; outgoing long wave radiation (OLR) (W m^{-2}), derived from NCEP/NCAR reanalysis data, cirrus cloud fraction taken from MODIS observations, and H_2O, Ice Water Content (IWC), and Temperature (T) at different pressure levels, observed from the Microwave Limb Sounding (MLS) version 3.3 datasets, from January, 2005 to March, 2013 period.

7.1 The role of local convection on the budgets of water vapour

Measurements of OLR and cirrus cloud fractions are important proxies/indicators for the evaluation of convection strength. Fig. 7.1 demonstrates the composite annual mean of outgoing longwave radiation (OLR) (W m^{-2}) (left panel) and cirrus cloud fraction (right panel) over Ethiopia (3°N-15°N latitude and 33°E-48°E longitude) from January, 2005 to March, 2013. This suggests that there is a clear spatial variations of the convection strength over the domain of the region. Cumulonimbus clouds, representative of deep convection, have high cold tops and they radiate little longwave radiation to outer space. Regions with low OLR are therefore associated with deep convection. Areas of OLR with values less than 236 and 220 W m^{-2} can be considered as an estimation of the convective outflow location in the middle (∼400 hPa) and in the upper (∼100 hPa) tropical troposphere, respectively. As shown in the left panel of Fig. 7.1, OLR values less than 240 W m^{-2} displayed by blue color, which is a representative of deep convection. Thus, the role of convection is quite significant on the distribution water vapour in the atmosphere at the observation site. Fig. 7.2 displays the time series of monthly mean of OLR (W m^{-2}) (black line) and H_2O VMR at 215 hPa, over Addis Ababa, in the period between January, 2005 and March, 2013. OLR values are taken from NCEP/NCAR reanalysis data and H_2O VMR at 215 hPa are obtained from MLS observation datasets. In general, it has been observed that there is a strong coherent variations of OLR and H_2O VMR at 215 hPa in the plot. During the summer (June-July-August) season, the OLR values recorded in the range between 236 and 210 W m^{-2}, as shown in Fig. 7.2, which is a

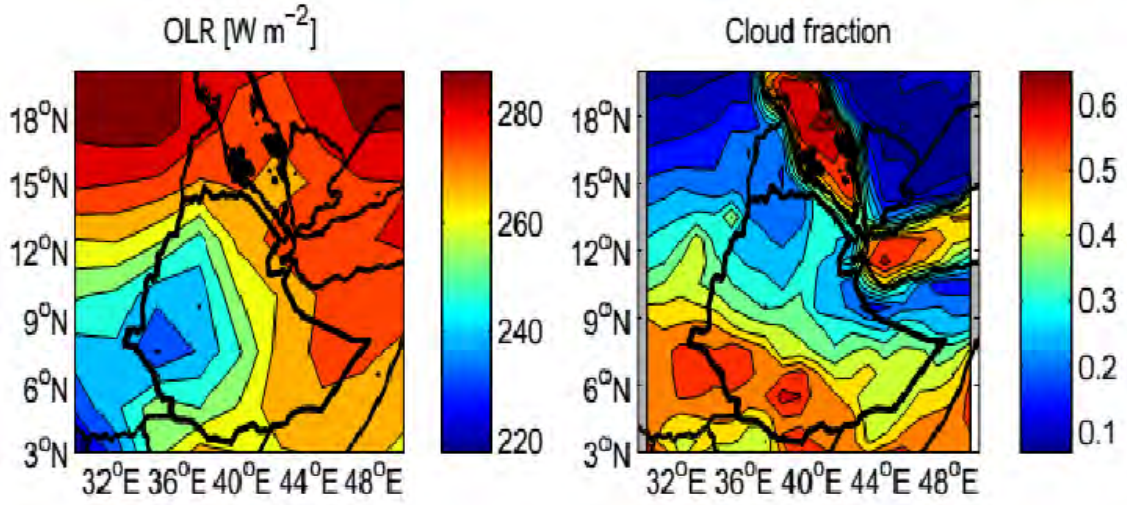

Figure 7.1: Maps of composite annual mean of outgoing longwave radiation (OLR) (W m^{-2}) (left panel) and cloud fraction (right panel) over Ethiopia, in the period between January, 2005 and March, 2013.

representative of convection in the middle and upper troposphere. This suggests the upper troposphere water vapour budget is largely controlled by the local deep convection during summer season over the observation site. On the contrary, in winter season (December, January, February), the role of convection driven transport process is negligible. Previous studies have shown that average relative humidity in the 550-200 hPa layer tends to increase with the amount of deep convective clouds [154]. Recent simultaneous observations of upper tropospheric water vapour and cloud ice from the Microwave Limb Sounder (MLS) on the Aura satellite provide new evidence for tropical convective influence on upper troposphere water vapour and its associated greenhouse effect [155]. It is found that water vapour within the TTL are inconsistent with gradual ascent and dehydration by in-situ cirrus formation, however, it is significantly influenced by the convective ice lofting and evaporation in the TTL.

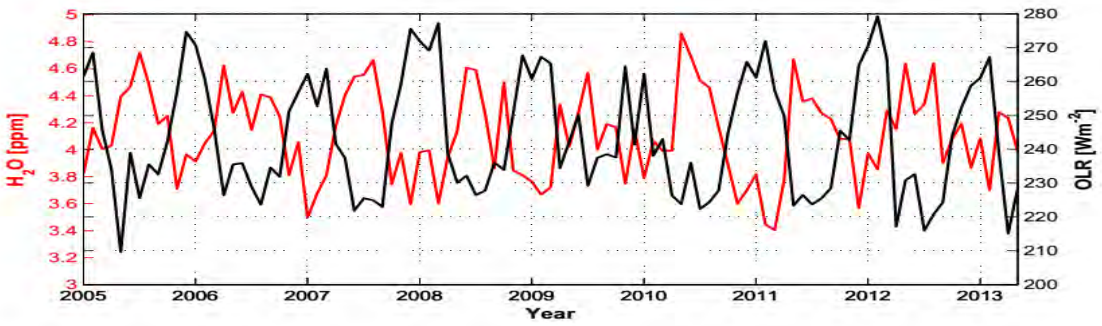

Figure 7.2: Time-series of monthly mean outgoing longwave radiation (OLR) (W m^{-2}) as derived from NCEP/NCAR reanalysis data (black line) and H_2O VMR at 215 hPa from MLS observations (red line), in the period between January, 2005 and March, 2013.

Table 7.1. Summary for correlations among T, H_2O and ice water content (IWC) derived from MLS. Below the given box T represents temperature at 100 hPa and number in the subscript of the parameters indicate pressure level.

H_2O_{100},IWC_{100}	T,IWC_{100}	T,H_2O_{100}	T,H_2O_{82}	T,H_2O_{68}	T,H_2O_{56}
-0.73	-0.78	0.88	0.83	0.80	0.76

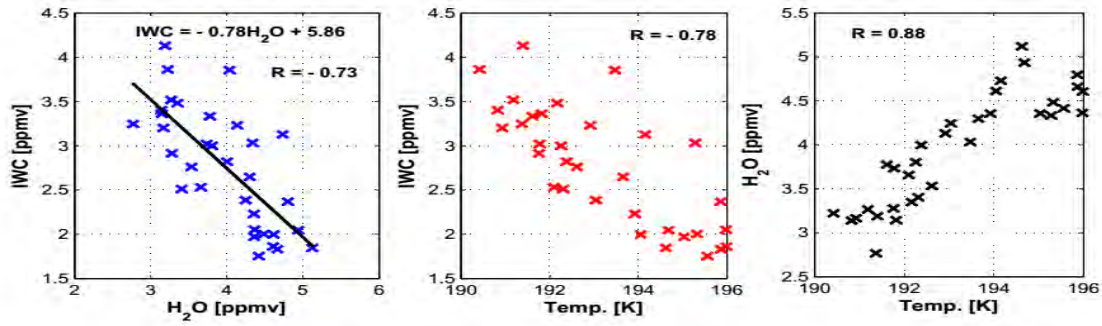

Figure 7.3: Scatter plots of seasonal mean of H_2O versus IWC (left panel), T versus IWC (middle panel), and T versus H_2O (right panel), derived from MLS datasets during a period January, 2005 - March, 2013. All are considered at 100 hPa pressure level.

7.2 The role of temperature on the budgets of water vapour

Air masses entering the stratosphere in the tropics must pass through the low temperature at the tropopause with substantial dehydration. This was first recognized by [12] after the observation of surprisingly low water vapour concentrations in the lower stratosphere. The process of temperature dependent dehydration can be observed in the so-called atmospheric tape recorder [156]. The variations in TTL water vapour are slowly carried upward into the stratosphere [157]. In this part of analysis, the role of temperature at 100 hPa is explored on the budget of water vapour at the TTL (121 to 68 hPa) and LS using correlation analysis. Since water vapour is transported upward and poleward from the tropics by the Brewer-Dobson circulation (BDC) it is expected H_2O to be lagged in phase with tropical 100 hPa temperatures at higher altitudes and higher latitudes. The time lag is between 1 week at 100 hPa ($\sim$16.4 km) and 21 weeks at 56 hPa ($\sim$20.1 km) which corresponds to an average vertical ascent rate of about 0.3 mm s^{-1} between the two levels [157]. On account of these assumptions in the transport process it is determined the time lag in order to find the maximum correlation of temperature and H_2O over the study site. The time series of monthly mean temperature at 100 hPa along with H_2O VMR at 82 hPa, 68 hPa and 56 hPa are displayed in Figs. 7.4, 7.5, and 7.6, respectively. These results of the correlation coefficients reflect a significant role of temperature on the regulation of water vapour in the respective layers. The correlation decreases as the altitude increases because of mixing with other air masses and in situ water vapour production by the oxidation of methane.

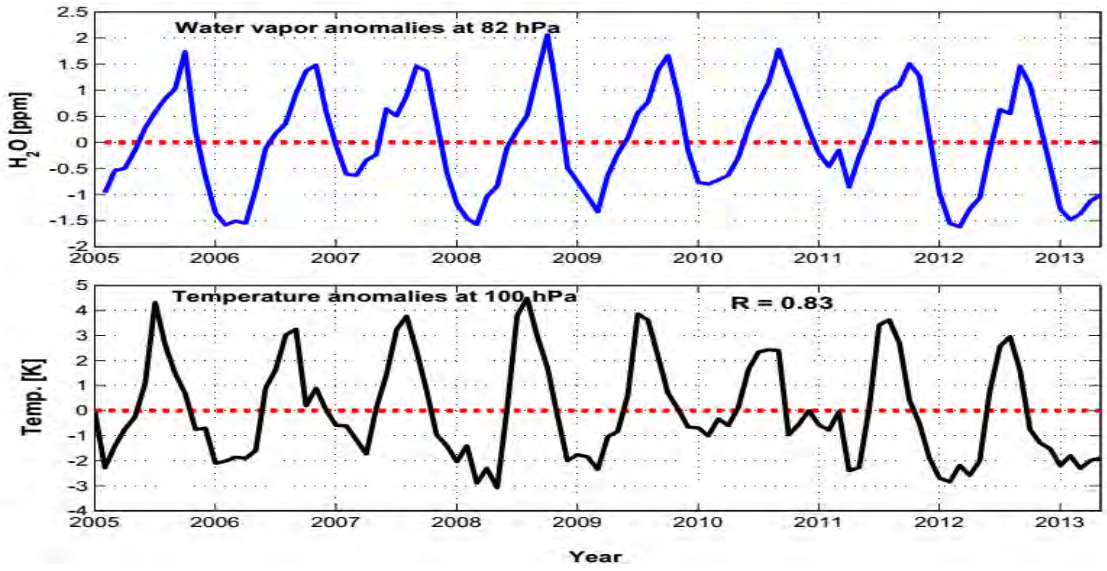

Figure 7.4: Time-series of monthly mean H_2O VMR at 82 hPa (top panel) and temperature at 100 hPa (bottom panel), both derived from MLS observation datasets for the period January, 2005 - March, 2013

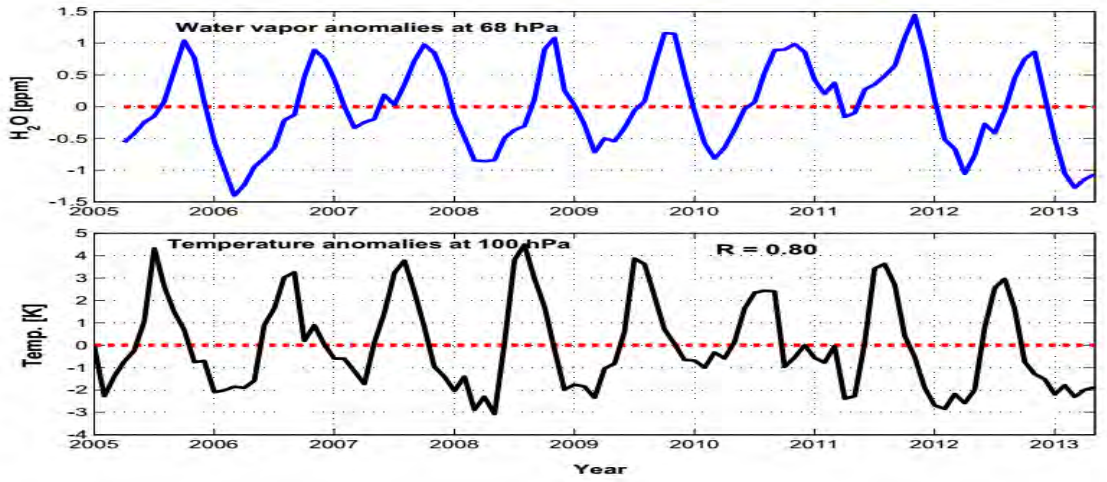

Figure 7.5: Similar to Fig. 7.4 but for H_2O VMR at pressure level of 68 hPa.

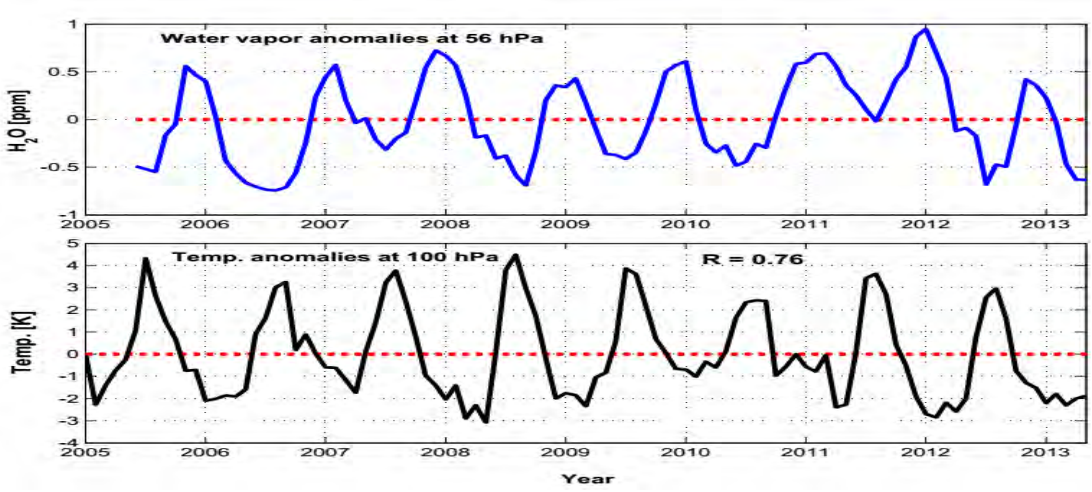

Figure 7.6: Similar to Fig. 7.4 but for H_2O VMR at pressure level of 56 hPa.

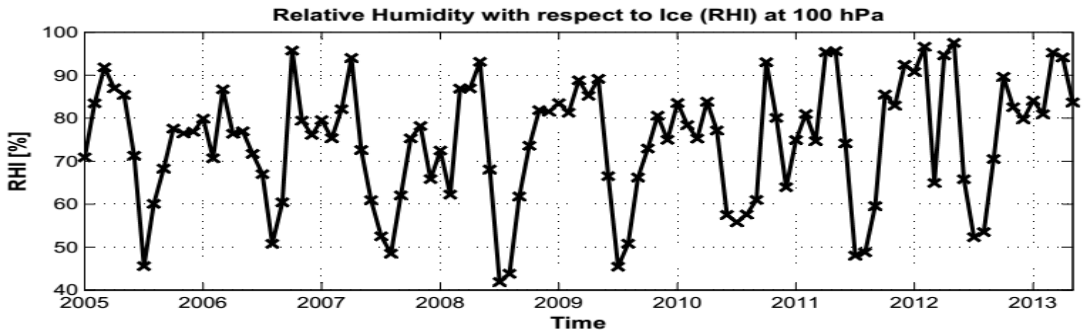

Figure 7.7: Time-series of monthly mean Relative Humidity with respect to Ice (RHI) [%] at 100 hPa from MLS observation datasets during the period January, 2005 to May, 2013.

The temperature is also the key parameter which determines the partitioning of vapour and ice in the TTL. It is anticipated that temperature acts as the regulator for the coherent water vapour and cloud variabilities by balancing the partition between water vapour and ice in cirrus clouds. It is important to quantify how much of the seasonal cycle of H_2O in the TTL is due to a varying supply from below or due to regulation by local temperature. Therefore, to address this issue the combined relationship of among cirrus ice water content (IWC), H_2O, and T derived from AURA/MLS data over a period of 2005-2013 are assessed. The knowledge of the balance of water vapour and ice water content is essential. The correlations among seasonal averages of H_2O, IWC, and T at 100 hPa as well as the slope of H_2O versus IWC of the regression line are illustrated in Fig. 7.3 and Table 7.1. As shown in the figure, the correlation coefficients of H_2O versus IWC (left panel) and T versus IWC (middle panel) are -0.73 and -0.78 respectively while T versus H_2O (right panel) exhibits a positive correlation, 0.88. In addition, the slope of linear regression line of seasonal averages of IWC versus H_2O is -0.78. This result strongly suggests that cirrus clouds to a large extent serve as a seasonal reservoir for TTL water vapour. Water switches seasonally between ice and vapour. High IWC values are almost directly linked to the lowest H_2O values during winter season (DJF). The correlation between H_2O versus IWC reflects the influence of tropospheric air that stems mostly due to deep overshooting convection.

Chapter 8

Conclusions

The water cycle is closely linked to the global energy and radiation budgets and has thus fundamental importance for climate on global as well as regional scales. Therefore, stable water isotopic measurements have been widely used to study the hydrological cycles, particularly, processes related to water movement among different reservoirs, e.g., atmospheric moisture cycling, evaporation, transpiration, groundwater recharge, and runoff [6].

Global scale datasets of atmospheric water vapour isotopologues have become available from different remote-sensing instruments. Due to the observational geometry and the spectral ranges that are used, only few satellites sample water isotopologues in the lower troposphere, where the bulk of hydrological processes within the atmosphere take place. Here, FTIR is one of the remote-sensing instrument that can provide the product of water vapour isotopologues. The FTIR solar absorption spectra have been recorded at Addis Ababa (9.01°N latitude, 38.76°E longitude, 2443 m altitude above sea level), Ethiopia from June, 2009 to March, 2013. In order to retrieve the amount of tropospheric water vapour stable isotopologues (in particular H_2O and HDO) from the FTIR spectra, extensive product characterization has been

performed in this study. On the basis of this, it is well documented the sensitivity, the vertical resolution and error analysis. This characterization is very important in order to understand the complex nature of the isotopologues remote sensing data. The H_2O profiles have a DOF on average 2.4, while for HDO/H_2O ratio profiles have a DOF on average 1.5. The sensitivity of both species is limited to the lower and middle troposphere. From error analysis, the measurement noise, the atmospheric temperature profiles, the uncertainty in the spectroscopy and spectral baseline are the main error sources. The study shows the initial retrieval products of H_2O and δD values are not the representative of the same airmass. Therefore, the aposteriori correction for the originally retrieved ln[H_2O] and ln[HDO] are applied based on the aposteriori processing techniques as presented in [3] so as to properly interpret these remote sensing products.

The observed level of agreement is determined from the intercomparison of H_2O profiles and column amounts from FTIR with model and satellites instruments. A good agreement is observed in the comparison of total column amounts of H_2O from FTIR and TES level3, with the overall mean relative differences of (3.5$\pm$23.7)%, which is statistically insignificant. This mean relative difference is found to be less as compared to the mean relative differences of (5.4$\pm$19.5)% in the comparison of H_2O column amounts between FTIR and GPS reported in [158]. The FTIR measures systematically higher H_2O integrated columns than the TES instrument since large contribution for integrated H_2O amount is coming from lower level troposphere, close to the surface. The intercomparison of H_2O VMR and column amounts from ground-based FTIR and those satellites reported in this work establishes two major features that characterize both satellite and FTIR instruments. First, the good agreement

between the H_2O VMRs and column amounts from FTIR with corresponding observations from satellites builds confidence in the FTIR observations. Second, though the satellite observations are already validated elsewhere, this is the first time observations of H_2O from these instruments are compared with ground-based FTIR observations over tropical Africa. As a result, the observed agreement between the FTIR H_2O observations with that of satellite observations builds also confidence in the validity of satellite observations over this particular region. Furthermore, the results of this intercomparison of FTIR observations with the satellites can ensure that FTIR observations can now be used to validate existing and future satellite missions.

The added value of the δD remote sensing data (FTIR and TES) is evaluated by comparing δD versus H_2O curves. From FTIR data, the added value of δD reflects dominant Rayleigh distillation process at the morning, whereas convective mixing is most likely significant at the afternoon observations. As for FTIR, we have evaluated the added value of δD from TES in the respective pressure levels of 682 hPa and 510 hPa at seasonal time scale at Addis Ababa. Enrichment characteristics are identified at 682 hPa level in all seasons, which is likely caused by surface influence which happened due to convection transport. In addition, δD vapour that falls below the Rayleigh curve is generally associated with moisture recycling in convective clouds, and this could partly describe some observations in summer season. Using TES observations, the spatial distributions and seasonal cycle of water vapour δD over Ethiopia have been elucidated and the main controls involving in local and large-scale processes are identified. The results show that water vapour δD values for both annual- and seasonal-scales exhibit a clear spatial structure of enriched values in the northeast, with gradual depletion extending towards the southwest region. The

seasonal variation of δD in vapour composition of the region is mainly controlled by differences in sources of moisture owing to the seasonal movement of the ITCZ and local factors such as amount and temperature effects. There is a good relation between the seasonal variation in isotopic composition of water vapour over Ethiopian and the seasonality in Ethiopian climate.

It has been dealt with one of the most debated aspect of the TTL and the LS budget of water vapour at local scale. The role of convection and temperature on the TTL and the LS water vapour budget are determined using Aura/MLS observations of water vapour, ice water content, temperature and OLR values from NOAA during a period between January, 2005 and March, 2013 over Addis Ababa, Ethiopia. Upper troposphere water vapour budget is largely controlled by convection during summer season over the observation site. The role of temperature at 100 hPa is explored on the budget of water vapour at the TTL (121 to 68 hPa) and LS (pressure $\leq$ 56 hPa) using correlation analysis and thus, reflects a significant role of temperature on the regulation of water vapour (ranging the correlation from R = 0.88 (at 100 hPa) to R = 0.76 (at 56 hPa)) in these layers. However, the correlation decreases as the altitude increases because of mixing with other air masses and in situ water vapour production by the oxidation of methane. The temperature is also the key parameter which determines the partitioning of vapour and ice in the TTL. It is found that cirrus clouds to a large extent serve as a seasonal reservoir for TTL water vapour.

Bibliography

[1] Pierrehumbert, R.: The hydrologic cycle in deep-time climate problems, Nature, 419, 191198, 2002.

[2] Harries, J. E.: The Greenhouse Earth - A view from space, Q. J. Roy. Meteor. Soc., 122, 799818, 1996.

[3] Schneider, M., Barthlott, S., Hase, F., González, Y., Yoshimura, K., García, O. E., Sepúlveda, E., Gomez-Pelaez, A., Gisi, M., Kohlhepp, R., Dohe, S., Blumenstock, T., Wiegele, A., Christner, E., Strong, K., Weaver, D., Palm, M., Deutscher, N. M., Warneke, T., Notholt, J., Lejeune, B., Demoulin, P., Jones, N., Griffith, D. W. T., Smale, D., and RobinsonJ.: Ground-based remote sensing of tropospheric water vapour isotopologues within the project MUSICA, Atmos. Meas. Tech., 5, 30073027, 2012.

[4] Trenberth, K. E., Smith, L., Qian, T., Dai, A., and Fasullo, J.: Estimates of the global water budget and its annual cycle using observational and model data, J. Hydrometeorol., 8(4), 758-769, doi:10.1175/JHM600.1., 2007.

[5] Willett, K. M., Gillett, N. P., Jones, P. D., and Thorne, P. W.: Attribution of observed surface humidity changes to human influence, Nature, 449(7163), 710-712, doi:10.1038/nature06207. 168, 549-561, doi:10.1007/s00442-011-2091-0, 2007.

[6] Worden, J., Noone, D., Bowman, K., Beer, R., Eldering, A., Fisher, B., Gunson, M., Goldman, A., Herman, R., Kulawik, S. S., Lampel, M., Osterman, G., Rinsland, C., Rodgers, C., Sander, S., Shephard, M., Webster, R., and Worden, H.: Importance of rain evaporation and continental convection in the tropical water cycle, Nature, 445, 528532, doi:10.1038/nature05508, 2007.

[7] Trenberth, K., Fasullo, J., and Kiehl, J.: Earth's global energy budget, B. Am. Meteorol. Soc., 311-323, doi:10.1175/2008BAMS2634.1, 2009.

[8] Holton, J. R. and Gettelman, A.: Horizontal transport and the dehydration of the stratosphere, Geophys. Res. Lett., 28, 27992802, 2001.

[9] Fueglistaler, S., Dessler, A. E., Dunkerton, T. J., Folkins, I., Fu, Q., and Mote, P. W.: Tropical tropopause layer, Rev. Geophys., 47, RG1004, doi:10.1029/2008RG000267, 2009.

[10] Gettelman, A., Salby, M. L., and Sassi, F.: The distribution and influence of convection in the tropical tropopause region, J. Geophys. Res., 107, 4080, doi:10.1029/2001JD001048, 2002.

[11] Fueglistaler, S., Wernli, H., and Peter, T.: Tropical troposphere-to-stratosphere transport inferred from trajectory calculations, J. Geophys. Res., 109, D03108, doi:10.1029/2003JD004069, 2004.

[12] Brewer, A. W.: Evidence for a world circulation provided by measurements of helium and water vapor distribution in the stratosphere, Q. J. Roy. Meteorol. Soc., 75, 351363, doi:10.1002/qj.49707532603, 1949.

[13] Sherwood, S. C. and Dessler, A. E.: On the control of stratospheric humidity, Geophys. Res. Lett., 27, 25132516, 2000.

[14] Sherwood, S. C. and Dessler, A. E.: A model for transport across the tropical tropopause, J. Atmos. Sci., 58, 765779, 2001.

[15] Sherwood, S. C. and Dessler, A. E.: Convective mixing near the tropical tropopause: insights from seasonal variations, J. Atmos. Sci., 60, 26742685, 2003.

[16] Knollenberg, R. G., Kelly, K., and Wilson, J. C.: Measurements of high number of ice crystals in the tops of tropical cumulonimbus, J. Geophys. Res., 98, 86398664, 1993.

[17] Corti, T., Luo, B. P., de Reus, M., Brunner, D., Cairo, F., Mahoney, M. J., Martucci, G., Matthey, R., Mitev, V., dos Santos, F. H., Schiller, C., Shur, G., Sitnikov, N. M., Spelten, N., Vossing, H. J., Borrmann, S., and Peter, T.: Unprecedented evidence for deep convection hydrating the tropical stratosphere, Geophys. Res. Lett., 35, L10810, doi:10.1029/2008GL033641, 2008.

[18] Khaykin, S., Pommereau, J.-P., Korshunov, L., Yushkov, V., Nielsen, J., Larsen, N., Christensen, T., Garnier, A., Lukyanov, A., and Williams, E.: Hydration of the lower stratosphere by ice crystal geysers over land convective systems, Atmos. Chem. Phys., 9, 22752287, doi:10.5194/acp-9-2275-2009, 2009.

[19] Chae, J. H., Wu, D. L., Read, W. G., and Sherwood, S. C.: The role of tropical deep convective clouds on temperature, water vapor, and dehydration in the tropical tropopause layer (TTL), Atmos. Chem. Phys., 11, 38113821, doi:10.5194/acp-11-3811-2011, 2011.

[20] Read, W. G., Schwartz, M. J., Lambert, A., Su, H., Livesey, N. J., Daffer, W. H., and Boone, C. D.: The roles of convection, extratropical mixing, and in-situ freeze-drying in the Tropical Tropopause Layer, Atmos. Chem. Phys., 8, 60516067, doi:10.5194/acp-8-6051-2008, 2008.

[21] Grosvenor, D. P., Choularton, T. W., Coe, H., and Held, G.: A study of the effect of overshooting deep convection on the water content of the TTL and lower stratosphere from Cloud Resolving Model simulations, Atmos. Chem. Phys., 7, 49775002, doi:10.5194/acp-7-4977-2007, 2007.

[22] Yang, Q., Fu, Q., and Hu, Y.: Radiative impacts of clouds in the tropical tropopause layer, J. Geophys. Res., 115, D00H12, doi:10.1029/2009JD012393, 2010.

[23] Flury, T., Wu, D. L., and Read, W. G.: Correlation among cirrus ice content, water vapor and temperature in the TTL as observed by CALIPSO and Aura/MLS, Atmos. Chem. Phys., 12, 683691, 2012. doi:10.5194/acp-12-683-2012, 2012.

[24] Salati, E., DallOlio, A., Matsui, E., and Gat, J. R.: Recycling of water in the Amazon Basin: an isotopic study, Water Resour. Res., 15, 12501258, 1979.

[25] Gat, J. R. and Matsui, E.: Atmospheric Water-Balance in the Amazon Basin - an Isotopic Evapotranspiration Model, J. Geophys. Res., 96, 1317913188, 1991.

[26] Risi, C., Bony, S., Vimeux, F., and Jouzel, J.: Water-stable isotopes in the LMDZ4 general circulation model: Model evaluation for present day and past climates and applications to climatic interpretations of tropical isotopic records, J. Geophys. Res., 115, D12118, doi:10.1029/2009JD013255, 2010.

[27] Tian, L., Masson-Delmotte, V., Stievenard, M., Yao, T., and Jouzel, J.: Tibetan Plateau summer monsoon northward extent revealed by measurements of water stable isotopes, J. Geophys. Res., 106, 2808128088, 2001.

[28] Galewsky, J., and Hurley, J. V.: An advection-condensation model for subtropical water vapor isotopic ratios, J. Geophys. Res., 115, D16116, doi:10.1029/2009JD013651, 2010.

[29] Moyer, E. J., Irion, F. W., Yung, Y. L., and Gunson, M. R.: ATMOS stratospheric deuterated water and implications for troposphere-stratosphere transport, Geophys. Res. Lett., 23, 23852388, 1996.

[30] Boesch, H., Deutscher, N. M., Warneke, T., Byckling, K., Cogan, A. J., Griffith, D. W. T., Notholt, J., Parker, R. J., and Wang, Z.: HDO/H_2O ratio retrievals from GOSAT, Atmos. Meas. Tech. Discuss., 5, 66436677, doi:10.5194/amtd-5-6643-2012, 2012.

[31] Frankenberg, C., Yoshimura, K., Warneke, T., Aben, I., Butz, A., Deutscher, N., Griffith, D., Hase, F., Notholt, J., Schneider, M., Schrejver, H., and Röckmann, T.: Dynamic processes governing lower-tropospheric HDO/H_2O ratios as observed from space and ground, Science, 325, 13741377, doi:10.1126/science.1173791, 2009.

[32] Frankenberg, C., Wunch, D., Toon, G., Risi, C., Scheepmaker, R., Lee, J.-E., Wennberg, P., and Worden, J.: Water vapor isotopologues retrievals from high resolution GOSAT short-wave infrared spectra, Atmos. Meas. Tech. Discuss., 5, 63576386, doi:10.5194/amtd-5-6357-2012, 2012.

[33] Lacour, J.-L., Risi, C., Clarisse, L., Bony, S., Hurtmans, D., Clerbaux, C., and Coheur, P.-F.: Mid-tropospheric δD observations from IASI/MetOp at high spatial and temporal resolution, Atmos. Chem. Phys., 12, 1081710832, doi:10.5194/acp-12-10817-2012, 2012.

[34] Payne, V. H., Noone, D., Dudhia, A., Piccolo, C., and Grainger, R. G.: Global satellite measurements of HDO and implications for understanding the transport of water vapour into the stratosphere, Q. J. Roy. Meteorol. Soc., 133, 14591471, doi:10.1002/qj.127, 2007.

[35] Schneider, M., Hase, F., and Blumenstock, T.: Ground-based remote sensing of HDO/H_2O ratio profiles: introduction and validation of an innovative retrieval approach, Atmos. Chem. Phys., 6, 47054722, doi:10.5194/acp-6-4705-2006, 2006b.

[36] Schneider, M. and Hase, F.: Optimal estimation of tropospheric H_2O and δD with IASI/METOP, Atmos. Chem. Phys., 11, 1120711220, doi:10.5194/acp-11-11207-2011, 2011b.

[37] Steinwagner, J., Milz, M., von Clarmann, T., Glatthor, N., Grabowski, U., Höpfner, M., Stiller, G. P., and Röckmann, T.: HDO measurements with MIPAS, Atmos. Chem. Phys., 7, 26012615, doi:10.5194/acp-7-2601-2007, 2007.

[38] Worden, J., Bowman, K., Noone, D., Beer, R., Clough, S., Eldering, A., Fisher, B., Goldman, A., Gunson, M., Herman, R., Kulawik, S., Lampel, M., Luo, M., Osterman, G., Rinsland, C., Rodgers, C., Sander, S., Shephard, M., and Worden, H.: TES observations of the tropospheric HDO/H_2O ratio: retrieval approach and characterization, J. Geophys. Res., 11, D16309, doi:10.1029/2005JD006606, 2006.

[39] Schneider, M., Yoshimura, K., Hase, F., and Blumenstock, T.: The ground-based FTIR networks potential for investigating the atmospheric water cycle, Atmos. Chem. Phys., 10, 34273442, doi:10.5194/acp-10-3427-2010, 2010b.

[40] De Wit, J. C., der Straaten, C. M. V., and Mook, W. G.: Determination of the absolute hydrogen isotope ratio of V-SMOW and SLAP, Geostandards Newsletter, 4, 3336, 1980.

[41] Baertschi, P.: Absolute ^{18}O content of Standard Mean Ocean Water, Earth and Planetary Science Letters, 31, 341344, 1976.

[42] Mook, W. M. E.: Environmental Isotopes in the Hydrological Cycle. Principles and Applications. UNESCO/IAEA Series, http://www.-naweb.iaea.org/napc/ih/volumes.asp. 2001.

[43] Craig, H.: Standard for Reporting concentrations of Deuterium and Oxygen-18 in natural waters, Science, 13, 18331834, doi:10.1126/science.133.3467.1833, 1961.

[44] Dansgaard, W.: Stable Isotopes in Precipitation, Tellus, 16, 436468, 1964.

[45] Majoube, M.: Fractionnement en oxygne-18 et en deutrium entre lèau et sa vapeur, Journal de Chimie et de Physique, 68, 14231436, 1971a.

[46] Merlivat, L., and Nief, G.: Fractionnement isotopique lors des changements détat solide-vapeur et liquide-vapeur de leau à des temperatures infèrieures à 0C, Tellus, 19, 122127, 1967.

[47] Majoube, M.: Fractionnement en oxygne 18 entre la glace et la vapeur deau, Journal de Chimie Physique, 68, 625636, 1971b.

[48] Arnason, B.: Equilibrium constant for the fractionation of deuterium between ice and water, J. Phys. Chem., 73, 34913494, 1969.

[49] Gat, J. R.: Oxygen and hydrogen isotopes in the hydrologic cycle, Annu. Rev. Earth Planet. Sci., 24, 225262, 1996.

[50] Merlivat, L. and Jouzel, J.: Global Climatic interpretation of the deuterium excess oxygen 18 relationship for precipitation, J. Geophys. Res., 84, 50295033, doi:10.1029/JC084iC08p05029, 1979.

[51] Jouzel, J. and Merlivat, L.: Deuterium and oxygen 18 in precipitation: modeling of the isotopic effects during snow formation, J. Geophys. Res., 89, 1174911757, doi:10.1029/JD089iD07p11749, 1984.

[52] Stewart, M. K.: Stable Isotope Fractionation Due to Evaporation and Isotopic-Exchange of Falling Waterdrops-Applications to Atmospheric Processes and Evaporation of Lakes, J. Geophys. Res., 80, 11331146, 1975.

[53] Gonfiantini, R.: Environmental isotopes in lake studies. In: Handbook of Environmental Isotope Geochemistry 2, P. Fritz and J.Ch. Fontes (Editors), Elsevier, New York, pp. 113-168, 1986.

[54] Celle, H., Daniel, M., Mudry, J., Blavoux, B.: Signal pluie et traage par les isotopes stables en Mditerrane occidentale: Exemple de la rgion avignonnaise (Sud-Est de la France). C. R. dAcad. Sci. Ser. IIA Earth Planet. Sci. 2000, 331, 647650, 2000.

[55] Cappa, C. D., Hendricks, M. B., DePaolo, D. J., and Cohen, R. C.: Isotopic fractionation of water during evaporation, Journal of Geophysical Research, VOL. 108, NO. D16, 4525, doi:10.1029/2003JD003597, 2003.

[56] Craig, H., Gordon, L. I., and Horiben, Y.: Isotopic exchange effects in the evaporation of water, J. Geophys. Res., 68(17), 5079 5087, 1963.

[57] Araguas-Araguas, L., Rozanski, K., Yurtsever, Y., Gu, W. Z., Jin, F., and Lian, Y.: Climatic control of stable isotope composition of precipitation over southeast Asia: In: Isotopes in Water Resources M anagement, Proceedings Series, IAEA, Vienna, 355-357, 1996.

[58] Gat, J. R. and Bowser, C. J.: The heavy isotope enrichment of water in coupled evaporative systems. In: Stable Isotope Geochemistry: A Tribute to Samuel Epstein, H.P. Taylor Jr., J.R. O'Neil and I. R. Kaplan (Editors), The Geochemical Society Special Publication No. 3, pp. 159-168, 1991.

[59] Risi, C., Noone, D., Frankenberg, C., and Worden, J.: Role of continental recycling in intraseasonal variations of continental moisture as deduced from model simulations and water vapor isotopic measurements, WATER RESOURCES RESEARCH, VOL. 49, 41364156, doi:10.1002/wrcr.20312, 2013.

[60] Mook, W. G.: Environmental isotopes in the hydrological cycle: principles and applications: Introduction, theory, methods, review Technical documents in hydrology; 39 Publ: 2000; 291 p., illus.; SC.2000/WS/58, 2000.

[61] Hase, F., Blumenstock, T., and Paton-Walsh, C.: Analysis of the instrumental line shape of high-resolution Fourier transform IR spectrometers with gas cell measurements and new retrieval software, Appl. Opt., 38, 3417−3422, 1999.

[62] Takele Kenea, S., Mengistu Tsidu, G., Blumenstock, T., Hase, F., von Clarmann, T., and Stiller, G. P.: Retrieval and satellite intercomparison of O_3 measurements from ground-based FTIR Spectrometer at Equatorial Station: Addis Ababa, Ethiopia, Atmos. Meas. Tech., 6, 495509, 2013.

[63] Chahine, M., Pagano, T., Aumann, H., Atlas, R., Barnet, C., Chen, L., Divakarla, M., Fetzer, E., Goldberg, M., Gautier, C., Granger, S., Irion, F. W., Kakar, R., Kalnay, E., Lambrigtsen, B., Lee, S., Marshall, J. L., McMillan, W., McMillin, L., Olsen, E. T., Revercomb, H., Rosenkranz, P., Smith, W., Staelin, D., Strow, L., Susskind, J., Tobin, D., and Wolf, W.: The Atmospheric Infrared Sounder (AIRS): improving weather forecasting and providing new insights into climate, B. Am. Meteorol. Soc., 87, 891894, doi:10.1175/BAMS-87-7-891, 2006.

[64] Gettelman, A., Weinstock, E., Fetzer, E., Irion, F., Eldering, A., Richard, E., Rosenlof, K., Thompson, T., Pittman, J., Webster, C., and Herman, R.: Validation of Aqua satellite data in the upper troposphere and lower stratosphere with insitu aircraft instruments, Geophys. Res. Lett., 31, L22107, doi:10.1029/2004GL020730, 2004.

[65] Fetzer, E. J., Read, W. G., Waliser, D., Kahn, B. H., Tian, B., Vömel, H., Irion, F. W., Sun, H., Eldering, A., de la Torre Juarez, M., Jiang, J., and Dang, V.: Comparison of upper tropospheric water vapor observations from the Microwave

Limb Sounder and Atmospheric Infrared Sounder, J. Geophys. Res., 113, D22110, doi:10.1029/2008JD010000, 2008.

[66] Hagan, D., Webster, C., Farmer, C., May, R., Herman, R., Weinstock, E., Christensen, L., Lait, L. R., and Newman, P. A.: Validating AIRS upper atmosphere water vapor retrievals using aircraft and balloon in situ measurements, Geophys. Res. Lett., 31, L21103, doi:10.1029/2004GL020302, 2004.

[67] Tobin, D., Revercomb, H., Knuteson, R., Lesht, B., Strow, L., Hannon, S., Feltz, W., Moy, L., Fetzer, E., and Cress, T.: Atmospheric Radiation Measurement site atmospheric state best estimates for Atmospheric Infrared Sounder temperature and water vapor retrieval validation, J. Geophys. Res., 111, D09S14, doi:10.1029/2005JD006103, 2006.

[68] Young-In Won, Document for AIRS Level-3 Version 5 Standard Products, GES DISC, March 3, 2008.

[69] Worden, J., Kulawik, S. S., Shepard, M., Clough, S., Worden, H., Bowman, K., and Goldman, A.: Predicted errors of Tropospheric Emission Spectrometer nadir retrievals from spectral window selection, J. Geophys. Res., 109, D09308, doi:10.1029/2004JD004522, 2004.

[70] Beer, R., Glavich, T., and Rider, D.: Tropospheric Emission Spectrometer for the Earth Observing Systems Aura satellite, Appl. Opt., 40, 23562367, 2001.

[71] Worden, J., Noone, D., Galewsky, J., Bailey, A., Bowman, K., Brown, D., Hurley, J., Kulawik, S., Lee, J., and Strong, M.: Estimate of bias in Aura TES HDO/H_2O

profiles from comparison of TES and in situ HDO/H_2O measurements at the Mauna Loa observatory, Atmos. Chem. Phys., 11, 44914503, 2011.

[72] Barnes, J. E., Kaplan, T., Vömel, H., and Read, W. G.: NASA/Aura/Microwave Limb Sounder water vapor validation at Mauna Loa Observatory by Raman lidar, J. Geophys. Res., 113, D15S03, doi:10.1029/2007JD008842, 2008.

[73] Jarnot, R. F., Perun, V. S., and Schwartz, M. J.: Radiometric and spectral performance and calibration of the GHz bands of EOS MLS, IEEE Trans. Geosci. Remote Sens., 44(5), 1131−1143, doi:10.1109/TGRS.2005.863714, 2006.

[74] Cofield, R. E. and Stek, P. C.: Design and field-of-view calibration of 114660 GHz optics of the Earth Observing System Microwave Limb Sounder, IEEE Trans. Geosci. Remote Sens., 44(5), 11661181, doi:10.1109/TGRS.2006.873234, 2006.

[75] Pickett, H. M.: Microwave Limb Sounder THz module on Aura, IEEE. Trans. Geosci. Remote Sens., 44(5), 1122−1130, 2006.

[76] Rodgers, C. D.: Inverse Methods for Atmospheric Sounding Theory and Practise, in: Series on Atmospheric, Oceanic and Planetary Physics, World Scientific (publisher), vol. 2, 2000.

[77] Read, W. G., et al.: Aura Microwave Limb Sounder upper tropospheric and lower stratospheric H_2O and relative humidity with respect to ice validation, J. Geophys. Res., 112, D24S35, doi:10.1029/2007JD008752, 2007.

[78] Lambert, A., Read, W. G., Livesey, N. J., Santee, M. L., Manney, G. L., Froidevaux, L., Wu, D. L., Schwartz, M. J., Pumphrey, H. C., Jimenez, C., Nedoluha, G. E., Cofield, R. E., Cuddy, D. T., Daffer, W. H., Drouin, B. J., Fuller, R. A.,

Jarnot, R. F., Knosp, B. W., Pickett, H. M., Perun, V. S., Snyder, W. V., Stek, P. C., Thurstans, R. P., Wagner, P. A., Waters, J. W., Jucks, K. W., Toon, G. C., Stachnik, R. A., Bernath, P. F., Boone, C. D., Walker, K. A., Urban, J., Murtagh, D., Elkins, J. W., and Atlas, E.: Validation of the Aura Microwave Limb Sounder middle atmosphere water vapor and nitrous oxide measurements, J. Geophys. Res., 112, D24S36, doi:10.1029/2007JD008724, 2007.

[79] Livesey, N. J.: EOS MLS Version 3.3 Level 2 data quality and description document, version 3.3 x-1.0, JPL D-33509, Jet Propul. Lab., Pasadena, Calif., 2011.

[80] Wu, D. L., Jiang, J. H., and Davis, C. P.: EOS MLS cloud ice measurements and cloudy-sky radiative transfer model, IEEE T. Geosci. Remote, 44, 11561165, 2006.

[81] Schwartz, M., Lambert, A., Manney, G., Read, W., Livesey, N., Froidevaux, L., Ao, C., Bernath, P., Boone, C., Cofield, R., Daffer, W. H., Drouin, B. J., Fetzer, E. J., Fuller, R. A., Jarnot, R. F., Jiang, J. H., Jiang, Y. B., Knosp, B. W., Kruger, K., Li, J.-L. F., Mlynczak, M. G., Pawson, S., Russell III, J. M., Santee, M. L., Snyder, W. V., Stek, P. C., Thurstans, R. P., Tompkins, A. M.P., Wagner, A., Walker, K. A., Waters, J. W., and Wu, D. L.: Validation of the Aura Microwave Limb Sounder temperature and geopotential height measurements, J. Geophys. Res.-Atmos., 113, D15S11, 19842012, doi:10.1029/2007JD008783, 2008.

[82] Wu, D. L., Jiang, J. H., Read, W. G., Austin, R. T., Davis, C. P., Lambert, A., Stephens, G. L., Vane, D. G., and Waters, J. W.: Validation of the Aura MLS cloud ice water content measurements, J. Geophys. Res., 113, D15S10, doi:10.1029/2007JD008931, 2008.

[83] King, M. D., Kaufman, Y. J., Menzel, W. P., and Tanre, D.: Remote sensing of cloud, aerosol, and water vapor properties from the Moderate Resolution Imaging Spectro-radiometer (MODIS). IEEE Trans. Geosci. Remote Sens., 30, 1-27, 1992.

[84] Liebmann, B. and Smith, C. A.: Description of a Complete (Interpolated) Outgoing Longwave Radiation Dataset, Bull. Am. Meteorol. Soc., 77, 12751277, 1996.

[85] Kanamitsu, M., Kumar, A., Juang, H.-M. H., Schemm, J.-K., Wang, W., Yang, F., Hong, S.-Y., Peng, P., Chen, W., Moorthi, S., and Ji, M.: NCEP dynamical seasonal forcast system 2000, Bull. Am. Meteorol. Soc., 83, 1019-1037, 2002.

[86] Chou, M.-D., and Suarez, M. J.: An efficient thermal infrared radiation parameterization for use in general circulation models, NASA Tech. Rep. TM-1994-104606 Series on Global Modeling and Data Assimilation, 85 pp, 1994.

[87] Moorthi, S., and Suarez, M. J.: Relaxed Arakawa-Schubert: A parameterization of moist convection for general circulation models, Mon. Weather Rev., 120, 9781002, 1992.

[88] Hong, S.-Y., and Pan, H.-L.: Convective trigger function for a massflux cumulus parameterization scheme, Mon. Weather Rev., 126, 25992620, 1998.

[89] Alpert, J., M. Kanamitsu, P. Caplan, J. Sela, and White, G.: Mountain induced gravity wave drag parameterization in the NMC medium-range forecast model, in Proceedings of Conference on 8^{th} Numerical Weather Prediction,pp.726733, Am. Meteorol. Soc., Baltimore, Md., 1988.

[90] Tiedtke, M.: The sensitivity of the time-mean large-scale flow to cumulus convection in the ECMWF model, in Proc. Workshop on Convection in Large-Scale Numerical Models, Reading, pp. 297316, ECMWF, U. K, 1983.

[91] Ek, M. B., Mitchell, K. E., Lin, Y., Rogers, E., Grunmann, P., Koren, V., Gayno, G., and Tarpley, J. D.: Implementation of Noah land surface model advances in the National Centers for Environmental Prediction operational mesoscale Eta model,J. Geophys. Res., 108(D22), 8851, doi:10.1029/2002JD003296, 2003.

[92] Yoshimura, K., Kanamitsu, M., Noone, D., and Oki, T.: Historical isotope simulation using Reanalysis atmospheric data, J. Geophys. Res., 113, D19108, doi:10.1029/2008JD010074, 2008.

[93] Lee, J., Worden, J., Noone, D. Bowman, K., Eldering, A., LeGrande, A., Li, J.-L.F., Schmidt, G., and Sodemann, H.: Relating tropical ocean clouds to moist processes using water vapor isotope measurements. Atmospheric Chemistry and Physics, 11, 741752, 2011.

[94] Yoshimura K, Frankenberg C, Kanamitsu M, et al.: Comparison of an isotopic atmospheric general circulation model with new quasi-global satellite measurements of water vapor isotopologues, J. Geophys. Res., 116: D19118, 2011.

[95] Jöckel, P., Sander, R., Kerkweg, A., Tost, H., and Lelieveld, J.: Technical Note: The Modular Earth Submodel System (MESSy) a new approach towards Earth System Modeling, Atmos. Chem. Phys., 5, 433444, doi:10.5194/acp-5-433-2005, 2005.

[96] Jöckel, P., Kerkweg, A., Buchholz-Dietsch, J., Tost, H., Sander, R., and Pozzer, A.: Technical 5 Note: Coupling of chemical processes with the Modular Earth Submodel System (MESSy) submodel TRACER, Atmos. Chem. Phys., 8, 16771687, doi:10.5194/acp-8-1677-2008, 2008.

[97] Jöckel, P., Kerkweg, A., Pozzer, A., Sander, R., Tost, H., Riede, H., Baumgaertner, A., Gromov, S., and Kern, B.: Development cycle 2 of the Modular Earth Submodel System 10 (MESSy2), Geosci. Model Dev., 3, 717752, doi:10.5194/gmd-3-717-2010, 2010.

[98] Dee, D. P., Uppala, S. M., Simmons, A. J., Berrisford, P., Poli, P., Kobayashi, S., Andrae, U., Balmaseda, M. A., Balsamo, G., Bauer, P., Bechtold, P., Beljaars, A. C. M., van de Berg, L., Bidlot, J., Bormann, N., Delsol, C., Dragani, R., Fuentes, M., Geer, A. J., Haimberger, L., Healy, S. B., Hersbach, H., Hólm, E. V., Isaksen, L., Kállberg, P., Khler, M., Matricardi, M., McNally, A. P., Monge-Sanz, B. M., Morcrette, J.-J., Park, B.-K., Peubey, C., de Rosnay, P., Tavolato, C., Thépaut, J.-N. and Vitart, F.: The ERA-Interim reanalysis: configuration and performance of the data assimilation system. Q. J. Roy. Meteorol. Soc., 137, 553597. doi:10.1002/qj.828, 2011.

[99] Keeling, C. D., Bacastow, R. B., Bainbridge, A. E., Ekdahl, C. A., Guenther, P. R., Waterman, L. S., and Chin, J. F. S.: Atmospheric carbon dioxide variations at Mauna Loa Observatory, Hawaii, Tellus, 28, 538551, doi:10.1111/j.2153-3490.1976.tb00701.x, 1976.

[100] Calvert, J. G.: Glossary of atmospheric chemistry terms (Recommendations 1990), Pure Appl. Chem., 62, 21672219, doi:10.1351/pac199062112167, 1990.

[101] Holton, J. R.: Introduction to dynamic meteorology, forth edition, Department of Atmospheric Science University of Washington, Elsevier Academic Press, 2004.

[102] Jacobson, M. Z.: Fundamentals of Atmospheric Modeling, second edition, Stanford University, Cambridge University press, 2005.

[103] Mengistu Tsidu, G.: High resolution monthly rainfall database for Ethiopia: Homogenization, Reconstruction, and Gridding, Journal of Climate, Vol. 25, No. 24, p. 8422-8443, doi: http://dx.doi.org/10.1175/JCLI-D-12-00027.1, 2012.

[104] Liou, K. N.: An introduction to Atmospheric radiation, Acadamic Press. Inc, 1980.

[105] Chandrasekhar, S.: Radiative Transfer, Dover publications, Inc., New York, 1960.

[106] Mengistu Tsidu, G.: The role of chemistry and transport on NO_y partitioning and budget during Austral Spring 2002 as derived from MIPAS measurement, PhD dissertation, institute für meteorologie and Klimaforschung, Germany, 2005.

[107] Rodgers, C. D.: Retrieval of atmospheric temperature and composition from remote measurements of thermal radiation, Rev. Geophys., 14(4), 609−624, 1976.

[108] Rodgers, C. D. and Connor, B. J.: Intercomparison of remote sounding instruments, J. Geophys. Res., 108(D3), 4116, doi:10.1029/2002JD002299, 2003.

[109] Levenberg, K.: A method for the solution of certain non-linear problems in least squares, Quart. Appl. Math., 2, 164-168, 1944.

[110] Marquardt, D. W.: An algorithm for least squares estimation of non-linear parameters, J. Soc. Indust. Appl. Math., 11(2), 431-441, 1963.

[111] Hase, F., Hannigan, J. W., Coffey, M. T., Goldman, A., Hopfner, M., Jones, N. B., Rinsland, C. P., andWood, S.W.: Intercomparison of retrieval codes used for the analysis of high-resolution, ground-based FTIR measurements, J. Quant. Spectrosc. Radiat. Transfer, 87, 25−52, 2004.

[112] Schneider, M. and Hase, F.: Improving spectroscopic line parameters by means of atmospheric spectra: theory and example for water vapour and solar absorption spectra, J. Quant. Spectrosc. Ra., 110, 18251839, 2009b.

[113] Hase, F. and Höpfner, M.: Atmospheric raypath modelling for radiative transfer algorithms, Appl. Optics, 38, 31293133, 1999a.

[114] Schneider, M. and Hase, F.: Ground-based FTIR water vapour profile analyses, Atmos. Meas. Tech., 2, 609619, doi:10.5194/amt 2-609-2009, 2009a.

[115] Phillips D.: A technique for the numerical solution of certain integral equations of first kind, J. Assoc. Comput. March., 9, 84−97, 1962.

[116] Tikhonov, A.: On the solution of incorrectly stated problems and method of regularization, Dokl. Akad, Nauk. SSSR, 151(3), 501−504, 1963.

[117] Schneider M., Hase, F., and Blumenstock, T.: Water vapour profiles by ground-based FTIR spectroscopy: study for an optimised retrieval and its validation, Atmos. Chem. Phys., 6, 811-830, 2006a.

[118] Notholt, J., Toon, G., Jones N., Griffith D., and Warneke, T.: Spectral line finding program for atmospheric remote sensing using full radiation transfer, Journal of Quantitative Spectroscopy and Radiative Transfer, Volume 97, Issue 1, p. 112-125. doi: 10.1016/j.jqsrt.2004.12.025, 2004.

[119] Schneider, M., Toon, G. C., Blavier, J.-F., Hase, F., and Leblanc T.: H_2O and δD profiles remotely-sensed from ground in different spectral infrared regions, Atmos. Meas. Tech., 3, 15991613, doi:10.5194/amt-3-1599-2010a.

[120] Sussmann, R. and Borsdorff, T.: Technical Note: Interference errors in infrared remote sounding of the atmosphere, Atmos. Chem. Phys., 7, 35373557, doi:10.5194/acp-7-3537-2007, 2007.

[121] Rothman, L. S., et al.: The HITRAN 2008 molecular spectroscopic database, J. Quant. Spectrosc. Ra., 110, 533572, doi:10.1016/j.jqsrt.2009.02.013, 2009.

[122] Rothman, L. S., et al.: The HITRAN 2012 molecular spectroscopic database, J. Quant. Spectrosc. Ra., Elsevier, ISSN 0022-4073, 2013.

[123] Funke, B. and von Clarmann, T.: How to average logarithmic retrievals? Atmos. Meas. Tech., 5, 831-841, 2012.

[124] Araguas-Araguas L, Froehlich K, and Rozanski K.: Stable isotope composition of precipitation over southeast Asia. J Geophys Res, 103: 2872128742, 1998.

[125] Kendall, C. and McDonnell, J. J.: Isotope Tracers in Catchment Hydrology, Netherlands, Elsevier Science B.V., 1998.

[126] Brubaker, K. L.; Entekhabi, D., and Eagleson, P. S.: Estimation of continental precipitation recycling. J. Clim., 6:1077, 1089, 1993.

[127] ZhongFang, L., Yoshimura K., Kennedy, C. D., XinHui, W., and ShuoGuang, P.: Water vapor δD dynamics over China derived from SCIAMACHY satellite measurements, April 2014 Vol.57 No.4: 813823 doi: 10.1007/s11430-013-4687-1, 2014.

[128] Bowen, R.: Groundwater, England, Elsevier Applied Science Publishers, 1986.

[129] Mazor, E.: Chemical and Isotopic Groundwater Hydrology, New York: Marcel Dekker Inc., 2004.

[130] Hoefs, J.: Stable Isotope Geochemistry, Germany, Springer, 2004.

[131] Lee, J. E., Risi, C., Fung, I., et al.: Asian monsoon hydrometeorology from TES and SCIAMACHY water vapor isotope measurements and LMDZ simulations: Implications for speleothem climate record interpretation. J Geophys Res, 117: D15112, 2012.

[132] Gedzelman, S. D., and Arnold. R.: Modeling the isotopic composition of precipitation, J. Geophys. Res.99, 1045510472, 1994.

[133] Gedzelman, S. D., and Lawrence, J. R.: The isotopic composition of cyclonic precipitation, J. Appl. Meteorol.21, 13851404, 1982.

[134] Lawrence, J. R., Gedzelman, S. D., Dexheimer, D., Cho, H. K., Carrie, S. D., Gasparini, R., Anderson, C. R., Bowman, K. P., and Biggerstaff, M. I.: Stable isotopic composition of water vapor in the tropics,J. Geophys. Res., 109, D06115, doi:10.1029/2003JD004046, 2004.

[135] Yapp, C. J.: A model for the relationships between precipitation D/H ratios and precipitation intensity, Journal of Geophysical Research , 87 , 96149620, 1982.

[136] Koster, R. D., de Valpine, D. P., and Jouzel, J.: Continental water recycling and $H_2^{16}O$ concentrations, Geophysical Research Letters , 20 , 22152218, 1993.

[137] Risi, C., Noone, D., Worden, J., Frankenberg, C., Stiller, G., Kiefer, M., Funke, B., Walker, K., Bernath, P., Schneider, M., Bony, S., Lee, J., Brown, D., and Sturm, C.: Process-evaluation of tropospheric humidity simulated by general circulation models using water vapor isotopic observations. Part 2: an isotopic diagnostic to understand the mid and upper tropospheric moist bias in the tropics and subtropics, J. Geophys. Res., 117, D05304, doi:10.1029/2011JD016623, 2012a.

[138] Welp, L. R., Lee, X., Griffis, T. J., Wen, X.-F., Xiao, W., Li, S., Sun, X., Hu, Z., Martin, M. V., and Huang, J.: A meta-analysis of water vapor deuterium-excess in the midlatitude atmospheric surface layer, Global Biogeochem. Cy., 26, GB3021, doi:10.1029/2011GB004246, 2012.

[139] Berkelhammer, M., Hu, J., Bailey, A., Noone, D. C., Still, C. J., Barnard, H., Gochis, D., Hsiao, G. S., Rahn, T., and Turnipseed, A.: The nocturnal water cycle in an open-canopy forest, J. Geophys. Res.-Atmos., 118, 1022510242, doi:10.1002/jgrd.50701, 2013.

[140] Hurley, J. V., Galewsky, J., Worden, J., and Noone, D.: A test of the advection-condensation model for subtropical water vapor using stable isotopologue observations from Mauna Loa Observatory, Hawaii, J. Geophys. Res., 117, D19118, doi:10.1029/2012jd018029, 2012.

[141] Keeling, C. D.: The concentration and isotopic abundances of atmospheric carbon dioxide in rural areas, Geochim. Cosmochim. Ac., 13, 322334, 1958.

[142] Merlivat, L.: The dependence of bulk evaporation coefficients on air-water interfacial conditions as determined by the isotopic method, J. Geophys. Res., 83, 29772980, doi:10.1029/JC083iC06p02977, 1978.

[143] Kimberly, E., Crow, S., Galewsky, J., Hardy, D. R., Sharp, Z. D., Worden, J., and Braun, C.: Upwind convective influences on the isotopic composition of atmospheric water vapor over the tropical Andes, Journal of Geophysical Research: Atmospheres, 10.1002/2014JD021487, 2014.

[144] Lai, C. T., Ehleringer, J. R., Bond, B. J., et al.: Contributions of evaporation, isotopic non-steady state transpiration and atmospheric mixing on the $\delta^{18}O$ of water vapour in Pacific Northwest coniferous forests. Plant Cell and Environment, 29(1): 7794, 2006.

[145] Lee, X., Smith, R., and Williams, J.: Water vapour O^{18}/O^{16} isotope ratio in surface air in New England, USA,Tellus, Ser. B, 58(4), 293304, doi:10.1111/j.1600-0889.2006.00191.x, 2006.

[146] Wen, X.-F., Zhang, S.-C., Sun, X.-M., Yu, G.-R., and Lee, X.: Water vapor and precipitation isotope ratios in Beijing, China,J. Geophys. Res., 115, D01103, doi:10.1029/2009JD012408, 2010.

[147] Clark, I. D., and P. Fritz, P.: Environmental Isotopes in Hydrogeology, CRC Press, Boca Raton, Fla, 1997.

[148] Field, R. D., Jones, D. B. A., and Brown, D. P.: Effects of post-condensation exchange on the isotopic composition of water in the atmosphere, J. Geophys. Res., 115, D24305, doi:10.1029/2010JD014334, 2010.

[149] Datta, P.S., Bhattachatya, S. K., Tyagi, S. K.: Oxygen-18 studies on recharge of phreatic aquifers and groundwater flow-paths of mixing in the Delhi area. Journal of Hydrology , 176, 25-36, 1996.

[150] Lee, J. -E., and Fung, I.: 'Amount effect' of water isotopes and quantitative analysis of post-condensation processes, Hydrol. Processes,22(1), 18, doi:10.1002/hyp.6637, 2007.

[151] Liu, C. and Zipser, E. J.: Implications of the day versus night differences of water vapor, carbon monoxide, and thin cloud observations near the tropical tropopause, J. Geophys. Res., 114, D09303, doi:10.1029/2008JD011524, 2009.

[152] Liu, C. and Zipser, E. J.: Global distribution of convection penetrating the tropical tropopause, J. Geophys. Res., 110, D23104, doi:10.1029/2005JD006063, 2005.

[153] Carminati, F., Ricaud, P., Pommereau, J.-P., Rivire, E., Khaykin, S., Atti, J.-L., and Warner, J.: Impact of tropical land convection on the water vapour budget in the Tropical Tropopause Layer, Atmos. Chem. Phys. Discuss., 13, 3305533087, 2013.

[154] Soden, B. J., and Fu, R.: A satellite analysis of deep convection, upper-tropospheric humidity, and the greenhouse effect,J. Clim., 8, 2333 2351, 1995.

[155] Su, H., William G., Read, Jonathan H., Jiang, Joe W., Waters, Dong L. Wu, and Eric J., Fetzer: Enhanced positive water vapor feedback associated with tropical deep convection: New evidence from Aura MLS, GEOPHYSICAL RESEARCH LETTERS, VOL. 33, L05709, doi:10.1029/2005GL025505, 2006.

[156] Mote, P. W., Rosenlof, K. H., McIntyre, M. E., Carr, E. S., Gille, J. C., Holton, J. R., Kinnersley, J. S., Pumphrey, H. C., Russell, III, J. M., and Waters, J. W.: An atmospheric tape recorder: The imprint of tropical tropopause temperatures on stratospheric water vapor, J. Geophys. Res., 101, 39894006, doi:10.1029/95JD03422, 1996.

[157] Schoeberl, M. R., Douglass, A. R., Stolarski, R. S., Pawson, S., Strahan, S. E., and Read, W. G.: Comparison of lower stratospheric tropical mean vertical velocities, J. Geophys. Res., 113, 24109, doi:10.1029/2008JD010221, 2008.

[158] Schneider, M., Romero, P. M., Hase, F., Blumenstock, T., Cuevas, E., and Ramos, R.: Continuous quality assessment of atmospheric water vapour measurement techniques: FTIR, Cimel, MFRSR, GPS, and Vaisala RS92, Atmos. Meas. Tech., 3, 323338, 2010.

Declaration

I hereby declare that this thesis is my original work and has not been presented for a degree in any other university. All sources of material used for the thesis have been duly acknowledged.

Name: Samuel Takele Kenea

Signature: .....

This thesis has been submitted for the examination with my approval as university advisor.

Name: Dr. Gizaw Mengistu

Signature: .....

Addis Ababa University

Department of Physics

October, 2014